Universität Stuttgart

Institut für Wasser- und Umweltsystemmodellierung

Mitteilungen

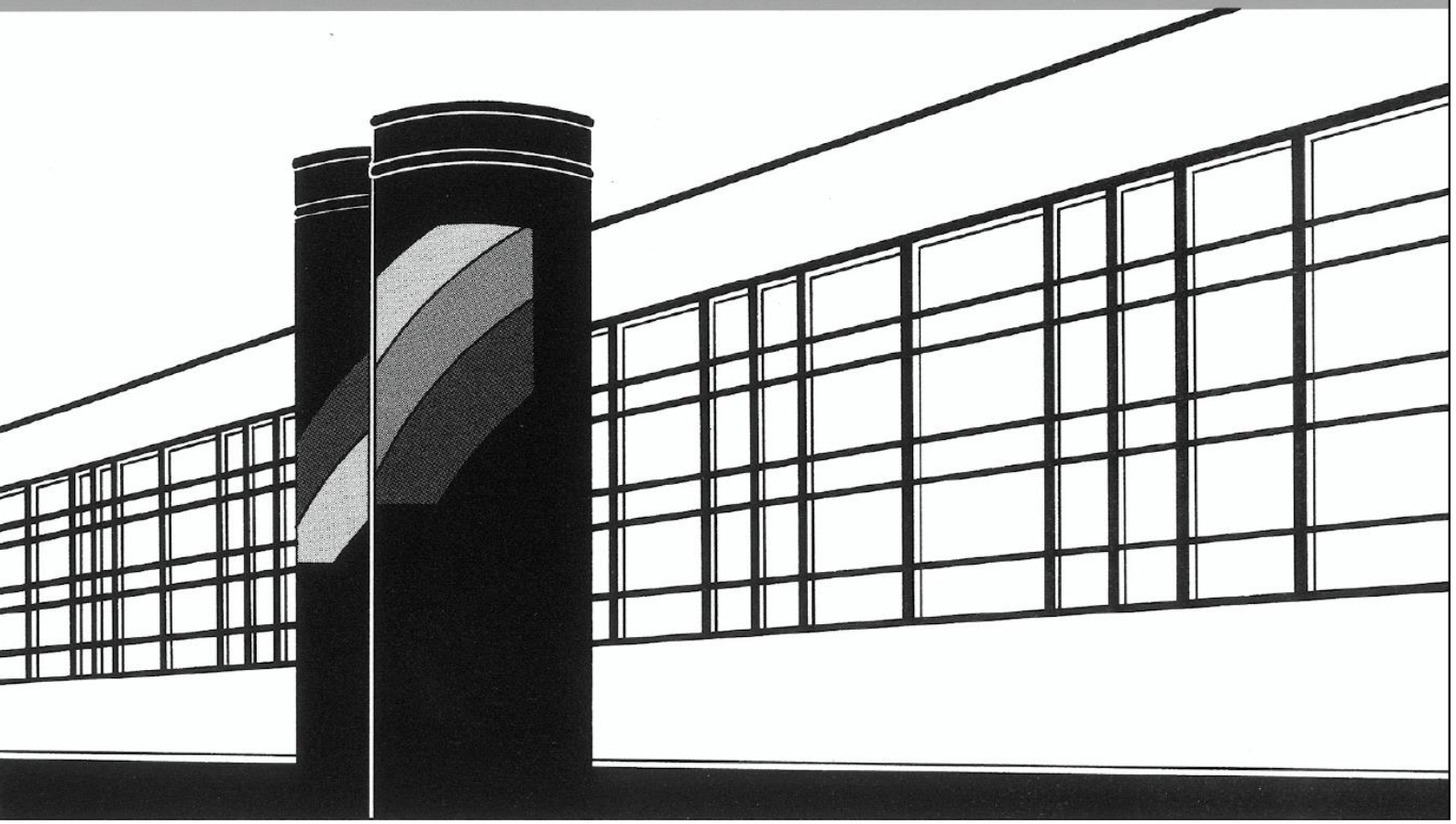

Heft 278 Gabriele Seitz

Modeling Fixed-Bed Reactors for Thermochemical Heat Storage with the Reaction System $CaO/Ca(OH)_2$

Modeling Fixed-Bed Reactors for Thermochemical Heat Storage with the Reaction System $CaO/Ca(OH)_2$

von der Fakultät Bau- und Umweltingenieurwissenschaften
und dem Stuttgart Research Centre for Simulation Technology der
Universität Stuttgart zur Erlangung der Würde eines
Doktor-Ingenieurs (Dr.-Ing.) genehmigte Abhandlung

vorgelegt von

Gabriele Seitz
aus Starnberg, Deutschland

Hauptberichter:	apl. Prof. Dr.-Ing. Holger Class
Mitberichter:	Prof. Dr.-Ing. Rainer Helmig
	Prof. Dr.-Ing. Joachim Groß
	Prof. Dr.-Ing. Gerhard Schäfer

Tag der mündlichen Prüfung: 24.02.2021

Institut für Wasser- und Umweltsystemmodellierung
der Universität Stuttgart
2021

Heft 278

Modeling Fixed-Bed Reactors for Thermochemical Heat Storage with the Reaction System $CaO/Ca(OH)_2$

von
Dr.-Ing.
Gabriele Seitz

Eigenverlag des Instituts für Wasser- und Umweltsystemmodellierung
der Universität Stuttgart

D93 Modeling Fixed-Bed Reactors for Thermochemical Heat Storage with the Reaction System $CaO/Ca(OH)_2$

Bibliografische Information der Deutschen Nationalbibliothek
Die Deutsche Nationalbibliothek verzeichnet diese Publikation in der Deutschen Nationalbibliografie; detaillierte bibliografische Daten sind im Internet über http://www.d-nb.de abrufbar

Seitz, Gabriele:
Modeling Fixed-Bed Reactors for Thermochemical Heat Storage with the Reaction System $CaO/Ca(OH)_2$, Universität Stuttgart. - Stuttgart: Institut für Wasser- und Umweltsystemmodellierung, 2021

(Mitteilungen Institut für Wasser- und Umweltsystemmodellierung, Universität Stuttgart: H. 278)
Zugl.: Stuttgart, Univ., Diss., 2021
ISBN 978-3-942036-82-5

NE: Institut für Wasser- und Umweltsystemmodellierung <Stuttgart>: Mitteilungen

Herausgegeben 2021 vom Eigenverlag des Instituts für Wasser- und Umweltsystem-modellierung

Druck: DCC Kästl e.K., Ostfildern

Danksagung

Diese Arbeit wäre ohne die Unterstützung zahlreicher BegleiterInnen unvollendet geblieben. Bei allen möchte ich mich herzlich bedanken:

Allen voran bei Rainer und Holger, die mir die Möglichkeit zur Promotion gegeben haben. Obwohl es im Projekt mehrere Durststrecken und Sackgassen gab, stand für beide das Zuendeführen meiner Arbeit nie in Frage. So beschafften sie auch eine weiterführende Projektfinanzierung, sodass das Projekt zunächst vom Ministerium für Forschung und Kunst Baden-Württemberg und später von der Friedrich und Elisabeth Boysen-Stiftung gefördert wurde. Vielen Dank für die finanzielle Unterstützung. Rainer und Holger standen mir immer mit fachlichem Rat zur Seite, ob beim Herleiten von Gleichungen, Fehlersuchen, oder Neuorientieren, wenn sich eine Richtung als nicht geeignet erwies. Danke darüber hinaus an Holger, der mich besonders im letzten Jahr darin unterstützt hat, die Arbeit noch zügig fertig zu bekommen und für die Korrektur sogar mindestens ein Wochenende investiert hat.

Großen Anteil am Gelingen dieser Arbeit hatte der Support für die Arbeit mit DuMu^{x}. Vielen Dank hier insbesondere an Bernd für die regelmäßigen Termine und auch an Dennis, Timo und Kilian. Ich konnte nicht nur auf eure bestehenden Implementierungen aufbauen, sondern bekam auch noch Unterstützung bei aktuellen Problemen.

Farid danke ich für die unermüdliche Arbeit an unserem gemeinsamen Paper, von dessen Umfang wir beide überrascht wurden.

Vielen Dank an Prof. Gerhard Schäfer und Prof. Joachim Groß für die Übernahme des Mitberichts. Danke Joachim außerdem für unsere Diskussionen zur Formulierung einer thermodynamisch konsistenten Reaktionskinetik.

Pru und Steffi halfen bei jeglichen Bereichen der Unibürokratie, und David und Michelle unterstützten in allen Technik-Belangen. Danke dafür!

Neben all der fachlichen und organisatorischen Unterstützung, war nicht zuletzt die angenehme Arbeitsatmosphäre am Lehrstuhl ausschlaggebend für das Gelingen der Arbeit. Gemeinsam mit Steffi, Katharina und Beatrix machte das Organisieren der SRP-Nupus-Events Spaß und war auch eine nette Abwechslung zur Forschung. Die wöchentliche Jogging-Runde war zugleich sportlicher Ausgleich zum Schreibtisch und

Gelegenheit zum Austausch. Ebenso das gemeinsame Mittagessen und die zahlreichen Kaffeerunden, in denen die Gespräche nicht selten bei neuen philosophischen Theorien landeten und die Kreativität beflügelten. Dafür bedanke ich mich bei allen Kollegen.

Bei Veronika und Lucia bedanke ich mich für ihre Korrekturen in der englischen Sprache. Danke für all die moralische Unterstützung von meiner Familie und meinen FreundInnen. Besonderer Dank gebührt meinem geliebten Leo. Er hat nicht nur meine Launen insbesondere in den stressigen Phasen er- und mitgetragen, sondern mir auch immer wieder vor Augen geführt, wie viel mehr das Leben zu bieten hat.

Contents

List of Figures

List of Tables

Nomenclature

Greek Letters

α_{HTF}	Heat transfer coefficient	$[\mathrm{W\,m^{-2}\,K^{-1}}]$
γ	Exponent (Power-law parameter)	[-]
λ	Heat conductivity	$[\mathrm{W\,m^{-1}\,K^{-1}}]$
μ	Dynamic viscosity	$[\mathrm{Pa\,s}]$
ν	Stoichiometric constant	[-]
ϕ	Porosity	[-]
ψ	Chemical potential	$[\mathrm{J\,mol^{-1}}]$
ρ, ρ_m	Density, molar density	$[\mathrm{\ kg\,m^{-3}}]$, $[\mathrm{mol\,m^{-3}}]$
τ	Tortuosity	[-]
θ_i	Volume fraction of phase i	[-]

Roman Letters

ΔH_R	Reaction enthalpy	$[\mathrm{J\,mol^{-1}}]$
ΔS_R	Reaction entropy	$[\mathrm{J\,mol^{-1}\,K^{-1}}]$
$\mathbf{j}, \mathbf{j}_e$	Mass flux, energy flux	$[\mathrm{mol\,m^{-2}\,s^{-1}}]$, $[\mathrm{J\,m^{-2}\,s^{-1}}]$
$\mathbf{K}$	Permeability	$[\mathrm{m^2}]$
$\mathbf{v}$	Velocity	$[\mathrm{m\,s^{-1}}]$
A	Pre-exponential factor (Arrhenius constant)	$[\mathrm{s^{-1}}]$

a_f	Fracture aperture	[m]
a_{sg}	Interfacial area between solid and gas phase	[m]
c_p	Heat capacity	$[\mathrm{J\,kg^{-1}\,K^{-1}}]$
D	Diffusion coefficient	$[\mathrm{m^2\,s^{-1}}]$
d_h, d_p	Hydraulic diameter, particle diameter	[m]
E	Activation energy (Arrhenius constant)	[J]
f	Function	[-]
G	Gibbs free energy	[J]
H, h	Enthalpy, specific enthalpy	[J], $[\mathrm{J\,kg^{-1}}]$
k^D, k^H	Reaction constants for dehydration and hydration	$[\ \mathrm{s^{-1}}]$
k_R	Reaction kinetics	$[\ \mathrm{s^{-1}}]$
K_{eq}	Equilibrium constant	[-]
L, l	Length	[m]
m	Mass	[kg]
M_i	Molar mass of i	$[\mathrm{mol\,kg^{-1}}]$
n	Molar amount	[mol]
p	Pressure	[Pa]
p_i	Partial pressure of substance i	[Pa]
Q, q	Heat, specific heat	[J], $[\mathrm{J\,kg^{-1}}]$
q^m_λ, q^e_λ	Molar / energetic source term in phase λ	$[\mathrm{mol\,m^{-3}}]$ / $[\mathrm{J\,m^{-3}}]$
q_R	Reaction rate	$[\mathrm{kg\,m^{-3}\,s^{-1}}]$
R, R_g	Universal gas constant, specific gas constant	$[\mathrm{J\,mol^{-1}\,K^{-1}}]$, $[\mathrm{J\,kg^{-1}\,K^{-1}}]$

S, s	Entropy, specific entropy	$[\mathrm{J\,K^{-1}}]$, $[\mathrm{J\,kg^{-1}\,K^{-1}}]$
T	Temperature	[K]
t	Time	[s]
U, u	Internal energy, specific internal energy	[J], $[\mathrm{J\,kg^{-1}}]$
V	Volume	[m]
W, w	Work, specific work	[J], $[\mathrm{J\,kg^{-1}}]$
X	Conversion	[-]
X_i	Mass fraction of substance i	[-]
x_i	Mole fraction of substance i	[-]
Kn	Knudsen Number	[-]
Nu	Nusselt Number	[-]
Pr	Prantl Number	[-]
Re	Reynolds Number	[-]

Sub-/Superscript

κ	Component
0	Initial quantity/ standard conditions
HTF	Heat transfer
pm	Porous medium

Symbols used only in the proximity to their definition are not listed in this nomenclature.

Abstract

Storage of thermal energy holds a great potential for energy efficiency improvements, as it enables to decouple (waste) heat production and heat demand in space and time. It is thus essential for reaching the goal of the Paris agreement (2015), namely limiting global warming under 2 °C. Of the three types of heat storage - sensible, latent and thermochemical - the latter has the greatest development potential. Thermochemical heat storage offers high storage densities and the possibility to store energy chemically bound without losses. However, more research is needed before this technology is ready to be applied. Different materials are suitable for thermochemical heat storage. Most of them are gas-solid reactions in which the reverse reaction can be prevented by separating the gaseous component.

We limit this work to the reaction of Calcium hydroxide ($Ca(OH)_2$) under supply of heat to water vapor and Calcium oxide (CaO). The reaction stores energy in the form of reaction enthalpy, while the reverse reaction releases heat. Although this reaction system is comparatively well studied, there is no consensus on the reaction mechanism. The water vapor pressure determines the reaction temperature between approx. 400 - 800 °C. At different pressures for storage-loading and -unloading, heat can be released at a higher temperature level than required for loading. During the reaction, different physical and chemical processes depend on each other in a complex way, e.g. gas pressure and temperature change the fluid viscosity and thus the gas flow behavior that controls the reaction. Furthermore, the solid volume changes during the reaction, which also influences the flow field of the gas. After several cycles of charging and discharging, the solid particles agglomerate. As a result, the conversion rate declines.

To bring the technology to market, it is important to understand the different processes and their interactions. Numerical modeling is a suitable method for investigating and understanding the complex interactions of physical and chemical processes involved in

thermochemical heat storage. Individual phenomena and their effects on the reaction process can be tested in numerical experiments. Comparing the model results with suitable experimental data shows whether the model covers all the relevant processes. Model verification by benchmarking is a further method to confirm the model.

This work is limited to the simulation of fixed-bed reactors. The solid material in the form of particles or pellets is filled into a container. Adding or removing heat and steam from the system, controls the reaction. There are two types of fixed-bed reactors: (1) For the directly operated reactor concept, a mixture of steam and an inert gas as heat transfer fluid (usually nitrogen) is passed through the fixed bed. The partial pressure of the steam and the gas temperature control the reaction. Reaction gas supply and heat transfer are coupled together. (2) In the indirectly operated reactor concept, heat exchanger channels run through the fixed bed, which remove/transport the heat generated in the reaction. In the fixed bed itself, pure water vapor surrounds the solid particles. Here, the reaction is controlled by the absolute gas pressure in the fixed bed and the temperature imposed in the heat transfer channel.

In the model, we represent the fixed bed of both reactor types as a porous medium. We formulate balance equations for all chemical components involved as well as the energy, and solve them numerically in the simulator DuMu$^{\text{x}}$. Both reactor types have different requirements for the model setup.

Simulation of the directly operated reactor concept We assume a perfectly isolated reactor and thus reduce the homogeneous reactor filling to a one-dimensional model setup. We verify the model by comparing the simulation results of different models in a benchmark. The benchmark scenario, however, is based on several simplifying assumptions, that we investigate subsequently. The assumption of a local thermal equilibrium is appropriate for small particle sizes. Yet, the effect of the solid volume change on the reaction behavior is significant. The changed volumetric composition of gas and solid influences the heat transport in the porous bulk and thus the reaction process. In addition, a change in the gas flow resistance alters the gas pressure, which also determines the reaction rate. We use a discrete fracture model to drop the assumption of a homogeneous bulk and to represent the agglomerates formed after several cycles of loading and unloading. The fractures between the agglomerates represent the preferential flow paths of the gas flow. We show that these patterns always affect the energy

efficiency of the storage negatively. Although the processes of permeability alteration and fracture formation are covered in literature, there are no quantifying experiments. So, the information given by the simulations based on those experiments has only a qualitative character.

Simulation and model validation of the indirectly operated reactor concept The model for the indirectly operated reactor concept consists of two sub-domains: the fixed-bed reactor and the heat exchanger channel. The heat exchanger channel is simplified to one dimension under simplifying assumptions, while the fixed bed is represented two-dimensionally. We represent the experimental setup of [Schmidt et al., 2017] and aim to validate the model on the basis of their experimental results. However, we found several uncertain parameters, such as undetermined heat losses over the reactor casing. The reaction rate also contains uncertainties. We determine the most uncertain parameters by Bayesian parameter inference and show that the temperature loss significantly influences the course of the reaction. Furthermore, we detect a decrease of the reaction rate with progressing conversion and attribute it to the presence of agglomerates.

Kurzfassung

Um die globale Erwärmung entsprechend dem Pariser Klimaabkommen (2015) auf unter 2 °C zu beschränken, muss der Ausstoß an Treibhausgasen weltweit bis zum Jahr 2050 auf null sinken. Durch räumliche und zeitliche Entkopplung der Erzeugung und Freisetzung thermischer Energie ermöglicht die Wärmespeicherung ein Zusammenführen von Bedarf und Überproduktion. Damit ermöglicht sie Energieeffizienzsteigerungen, die unabdingbar sind, um das Ziel des Klimaabkommens zu erreichen. Unter den drei Arten der Wärmespeicherung - sensibel, latent und thermochemisch - weist Letztere das größte Entwicklungspotenzial auf. Thermochemische Wärmespeicherung bietet die Möglichkeit, chemisch gebundene Energie verlustfrei zu speichern, bei gleichzeitig hohen erreichbaren Speicherdichten. Es besteht allerdings noch Forschungsbedarf, bevor diese Technologie kommerziell eingesetzt werden kann. Verschiedene Materialien eignen sich zu thermochemischer Wärmespeicherung. Meist handelt es sich dabei um Gas-Feststoffreaktionen, bei denen durch das Abtrennen der gasförmigen Komponente die Rückreaktion verhindert wird.

Diese Arbeit beschränkt sich auf die thermochemische Reaktion von Calciumhydroxid ($Ca(OH)_2$) unter Wärmezufuhr zu Wasserdampf und Calciumoxid (CaO). Die genannte Reaktion speichert Wärme in Form von Reaktionsenthalpie, während die Rückreaktion Wärme freisetzt. Der Feststoff wird dabei in Form von Partikeln oder Pellets verwendet. Obwohl dieses Reaktionssystem vergleichsweise gut erforscht ist, besteht dennoch kein Konsens über den Reaktionsmechanismus. Der Wasserdampfdruck bestimmt die Reaktionstemperatur zwischen ca. 400 - 800 °C. Bei unterschiedlichen Drücken für Speicherbe- und -entladung kann die Wärme auf einem höheren Temperaturniveau abgegeben werden als für die Beladung benötigt wird. Verschiedene physikalische und chemische Prozesse, die bei der Reaktion auftreten, bedingen sich in komplexer Weise gegenseitig. Beispielsweise ändern Gasdruck und -temperatur die Fluidviskosität und

damit das Gasfließverhalten, das die Reaktion steuert. Ferner ändert sich das Feststoffvolumen bei der Reaktion, was ebenfalls das Strömungsfeld des Gases beeinflusst. Bei mehrmaligem Be- und Entladen führt dieses Ausdehnen und Zusammenziehen des Feststoffs in einem Festbettreaktor zu Agglomeratbildung und, damit einhergehend, verschlechtertem Reaktionsverhalten.

Um die Technologie zur Marktreife zu bringen gilt es, die einzelnen Prozesse und deren Interaktion zu verstehen. Die numerische Modellierung zeigt sich hierfür als geeignete Methode, um die komplexen Zusammenhänge und Abläufe aus physikalischen und chemischen Prozessen bei der Wärmespeicherung zu untersuchen und zu erfassen. In numerischen Experimenten können einzelne Phänomene und ihre Auswirkung auf das Reaktionsgeschehen getestet werden. Der Vergleich mit geeigneten experimentellen Daten zeigt auf, ob im Modell die relevanten Prozesse korrekt abgebildet sind. Auch eine Modellverifizierung durch einen Benchmark bestätigt das Modell.

Diese Arbeit beschränkt sich auf die Simulation von Festbettreaktoren. Dabei wird der Feststoff in ein Behältnis gefüllt, in dem die Reaktion durch Zu- oder Abfuhr von Wärme und Wasserdampf gesteuert abläuft. Zwei Reaktortypen werden nach ihrer Betriebsweise unterschieden: (1) Beim direkten Reaktorkonzept wird Wasserdampf gemischt mit einem inerten Wärmeträgerfluid (meist Stickstoff) durch das Festbett geleitet. Der Wasserdampfpartialdruck und die Gastemperatur steuern die Reaktion. Reaktionsgasbereitstellung und Wärmeübertragung sind miteinander gekoppelt. (2) Beim indirekten Reaktorkonzept durchziehen Wärmetauscherkanäle das Festbett, die die im Festbett entstehende Wärme ab/antransportieren. Im Festbett selbst umgibt reiner Wasserdampf die Feststoffpartikel. Hier wird die Reaktion durch den Absolutdruck im Festbett und die im Wärmetauscherkanal vorgelegte Temperatur gesteuert.

Im Modell wird das Festbett beider Reaktortypen als poröses Medium abgebildet. Es werden Bilanzgleichungen für alle beteiligten chemischen Komponenten sowie die Energie formuliert und mit der Simulationssoftware DuMu$^{\text{x}}$ numerisch gelöst. Beide Reaktortypen stellen unterschiedliche Anforderungen an den Modellaufbau.

Simulation des direkten Reaktorkonzepts Für eine homogene Schüttung mit idealisierter Wärmedämmung kann der direkte Reaktor eindimensional abgebildet werden. Ein Vergleich mit anderen Modellen aus anderen Softwarepaketen in einem Benchmarkszenario zeigt eine gute Übereinstimmung der Simulationsergebnisse und verifiziert

damit das Modell. Jedoch basiert das Benchmarkszenario auf vereinfachenden Annahmen, die im Anschluss untersucht werden. Die Annahme, Feststoff und Gas haben lokal die selbe Temperatur, kann für kleine Partikelgrößen bestätigt werden. Die Auswirkung der Veränderung des Feststoffvolumens auf das Reaktionsverhalten ist allerdings bedeutend. Die veränderte Volumenzusammensetzung aus Gas und Feststoff beeinflusst den Wärmeabtransport in der porösen Schüttung und damit den Reaktionsverlauf. Außerdem beeinflusst eine Veränderung des Fließwiderstands den Gasdruck, der ebenfalls die Reaktionsrate bedingt. Entscheidend ist ferner die Annahme eines homogenen Festbetts. Nach mehrmaligem Speicherbe- und entladen und Agglomeratbildung fließt das Gas vermehrt in bevorzugten Fließpfaden um diese herum. Im Modell werden diese Strukturen über ein diskretes Rissnetzwerk eingebaut. Es zeigt sich, dass diese Strukturen den energetischen Wirkungsgrad des Speichers reduzieren unabhängig von ihrer räumlichen Anordnung. Über die Prozesse der Permeabilitätsänderung der Rissbildung wird zwar in der Literatur berichtet, allerdings bestehen keine quantifizierenden Experimente, sodass auch die Aussage der darauf beruhenden Simulationen qualitativer Natur ist.

Simulation und Modellvalidierung des indirekten Reaktorkonzepts Das Modell zum indirekten Reaktorkonzept besteht aus zwei Teilgebieten, je für die Festbettschüttung und den Wärmetauscherkanal. Der Wärmetauscherkanal wird unter vereinfachenden Annahmen zu einer Dimension reduziert, während das Festbett zweidimensional repräsentiert wird. Das Modell bildet damit einen Versuchsaufbau aus [Schmidt et al., 2017] nach und wird anhand deren Experimentergebnissen validiert. Dafür werden zunächst Modellparameter ermittelt werden, die einen undetektierten Wärmeverlust über das Reaktorgehäuse abbilden. Ferner beinhaltet die Reaktionsrate Unsicherheiten. Die entscheidenden unsicheren Parameter werden ermittelt und über inverse Modellierung mit Hilfe Bayes'scher Parameterinferenz bestimmt. Es zeigt sich, dass der Temperaturverlust den Reaktionsverlauf maßgeblich beeinflusst. Aus den Daten wird außerdem auf eine Abnahme der Reaktionsgeschwindigkeit bei zunehmendem Reaktionsumsatz geschlossen, was auf das Vorhandensein von Agglomeraten zurückgeführt wird.

1 Introduction

Increasing urgency to mitigate climate change inspires the investigation of innovative means of energy storage. We first give a review on the world's energy consumption and the potential for efficiency increase by the different means of thermal energy storage. Against this background, we outline the objectives of this thesis, namely modeling thermochemical heat storage reactors.

1.1 Energy Conversion and Storage

In 2019, the world population consumed 158.8 $\cdot 10^{12}$ TWh ($\widehat{=}$ 571.8 EJ) of primary energy [BP p.l.c., 2020] with the major share of it falling upon fossil fuels (86.09 %). Therein, coal has a share of 27.6 %, oil of 33.75 %, and natural gas of 24.74 %, see Figure 1.1. The energy sector has a share of 73% to the global CO_2 emissions of in total 34.2 billion tonnes [BP p.l.c., 2020, IEA, 2020]. CO_2 is the most important greenhouse gas. The overall anthropogenic greenhouse gas emissions are estimated to 46.4 billion tonnes CO_2 equivalents [Ritchie, 2020].

Meanwhile, there is a common understanding, that anthropogenic emissions of greenhouse gases cause a climate change. Greenhouse gases absorb and scatter infrared radiation from the earth's surface, which would otherwise be emitted to space. Climate change is responsible for the melting glaciers, sea-level rise, the growing trend to extreme weather events and droughts [IPCC, 2018]. In order to limit the impacts of climate change on the earth, the United Nations in 2015 reached an agreement to limit the increase of global temperature below 2 °C in the Paris Agreement [UNFCCC, 2015]. To reach that goal, the anthropogenic greenhouse gas emissions have to be reduced to zero until the year 2050 [IPCC, 2018].

One aspect of reducing greenhouse gases is based on replacing the conventional energy production with renewable sources of energy, such as solar, wind, hydroelectric, geothermal and biomass. The largest potential is attributed to photovoltaic and wind energy production [Zsiborács et al., 2019]. However, their intermittent nature makes them challenging to integrate into the energy system. One solution to tackle this problem is to store overproduced energy in order to use it in times of increased demand [Delucchi and Jacobson, 2011, Bertsch et al., 2016].

A second aspect is based on energy savings by increasing energy efficiency [Ürge-Vorsatz and Metz, 2009, Metz et al., 2007, Edenhofer et al., 2014], e.g. by optimizing processes. Furthermore, many processes up to now emit waste heat, especially in the industrial sector [Pehnt et al., 2011], the building sector [Reddick et al., 2020] and for the conventional power production with fossil or nuclear fuels [Cot-Gores et al., 2012] at different temperature levels. Exploiting this surplus heat would increase the overall process efficiency. This fact becomes even more important when considering the share of final energy consumption. Figure 1.2 exemplifies the percentage of final energy consumption in Germany. With a share of 56.5 %, heat forms the bigger part of the final energy consumption in Germany. This includes space heating and cooling, warm water, and industrial heating and cooling and cold. For Europe, the share of heat at final energy consumption is 58 % [Köhler et al., 2016]. For developing countries, this percentage is even higher [Stoppok et al., 2018].

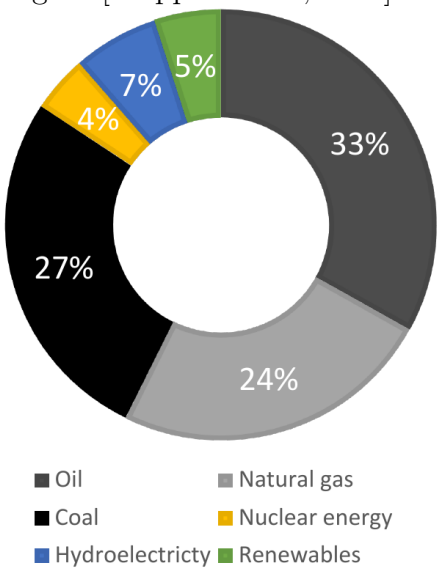

Figure 1.1: Contributions to the world's primary energy consmption in 2019. Data from [BP p.l.c., 2020]

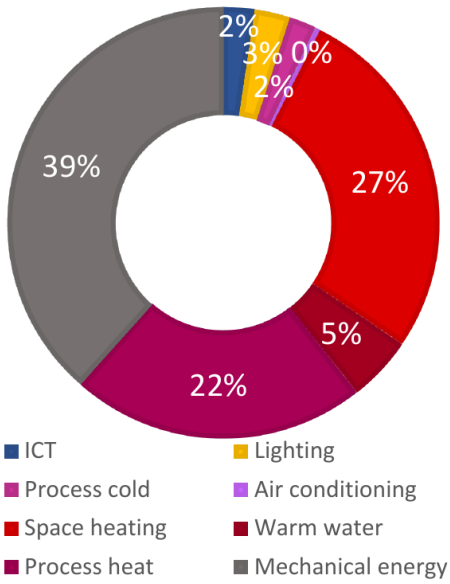

Figure 1.2: Final energy consumption examplarily for Germany in 2017. Data from [BMWi, 2019]

Energy storage is able to decouple the production of energy including sources such as waste heat and its consumption in space and time. It provides thus a possibility to link surplus or waste productions to the needs. Energy can be stored in its various forms, namely potential, chemical and thermal. However, each conversion of one form of energy to another induces a loss of efficiency [Sterner and Stadler, 2014]. In order to keep these losses low, energy is best stored either in the available form or in the form of consumption. Hence, thermal energy storage bears a high potential of increasing energy efficiency and promoting renewable sources of energy and is thus indispensable for coping with the challenge of climate change.

1.2 Thermal Energy Storage

There are three different kinds of thermal energy storage: sensible, latent and thermochemical. Their storage principles, advantages and disadvantages are outlined in the following sections. Table 1.1 provides an overview of typical storage media and the ranges for storage densities and temperature applications.

Table 1.1: Overview of heat storage technologies; data from [Aydin et al., 2015, Bauer et al., 2012, Sterner and Stadler, 2014, Felderhoff et al., 2013]

Storage type	**Material**	**Storage density** [kWh/m^3]	**Temperature range** [°C]
Sensible	Water $[\Delta T = 50$ K]	58	0 - 100
	Concrete $[\Delta T = 50$ K]	25 - 30	0 - 800
Latent	Paraffin	85	-12 - 70
	Molten salt	250	150 - 500
Thermochemical	Zeolite	150	25 - 200
	$CaO/CaCO_3$	1340	750 - 925

Further criteria for installing the heat storage would be the speed of charge and discharge, efficiency and costs. Those properties, however, strongly depend on the respective installation and are therefore not regarded further in this work.

1.2.1 Sensible Heat Storage

Sensible heat is stored as temperature difference of the storage medium. Besides the temperature difference, a high heat capacity is beneficial. Commonly used media are water or concrete. Sensible heat storage is a mature technology used in many applications for heating and cooling [Dincer and Ezan, 2018]. However, the storage densities are rather poor and good insulations are necessary to minimize losses. Additionally, the discharge temperature decreases with decreasing state of charge.

1.2.2 Latent Heat Storage

Latent heat storage exploits the heat of a phase change. Usually, the phase change between solid and gas is used, because the volume difference between solid and liquid is less important than between liquid and gas phase. Different materials are available for different temperature ranges, such as paraffin waxes for low level heat and molten salts for high temperatures. Latent heat storage allows higher storage densities than sensible heat storage. A clear advantage is the limited range of discharge temperatures close to the substances' melting point.

1.2.3 Thermochemical Heat Storage

Thermochemical heat storage can be further classified into heat storage based on sorption processes and on chemical reactions [Kerskes et al., 2011]. The former is based on physical ab- and adsorption of gases to solids under the release of heat, whereas heat storage based on a real chemical reaction involves molecular changes including breaking and restoring molecular bonds. Both means feature a possible high storage density and, due to a variety of possible materials, a large range for temperature applications from low level to high temperature heat [Kerskes et al., 2011]. As the stored heat is chemically bound in the reaction enthalpy (or enthalpy of sorption), heat can, in theory, be stored without losses [Kerskes et al., 2011]. Considerably higher storage densities can be reached, see Table 1.1. Furthermore, heat is released at a constant temperature depending on the equilibrium conditions of the reaction. This fact will be outlined in detail in Section 2.3.2. Thus, thermochemical heat storage has a high potential for

many ways of usage. However, the technology is not yet sufficiently investigated for ready-to-use applications. For systems based on sorption, there are already some applications commercially available, however financially not yet attractive [Kuznik et al., 2018]. For reaction-based thermochemical heat storage, so far only research plants exist [Carrillo et al., 2019].

In this thesis, we focus on thermochemical heat storage based on chemical reactions.

The thermochemical reactions of interest can be described by the following reaction equations:

$$\nu_{AB} \cdot AB_{(s)} \rightleftharpoons \nu_A \cdot A_{(s)} + \nu_B \cdot B_{(g)}, \quad \Delta H_R. \tag{1.1}$$

The solid AB is split by providing reaction enthalpy ΔH_R in the form of heat into another solid A and a gaseous component B. ν_i denotes the stoichiometric constants. The heat is then stored in the chemical potential of the two separated components A and B. Subtracting the gas B from the system prevents the reverse reaction. After complete conversion, the storage system is charged. The storage is discharged or the heat gets released by initiating the reverse reaction. Dosing the reaction fluid enables to control the discharge reaction.

Different reaction systems (comprising the substances AB, A and B) are possible for thermochemical heat storage. N'Tsoukpoe et al. [2014] and Richter et al. [2018] conducted material screenings and identified possible materials, which according to [Wentworth and Chen, 1976, Pardo et al., 2014] best fulfill the following criteria: large reaction enthalpies are favourable to reach high storage densities; the reaction should be fast, without side reactions and aging effects such as sintering; the compounds should be cheap, availabe and environmentally harmless for an easy handling of the storage. For detailed listings of possible materials with their respective temperature ranges, we refer to the mentioned publications.

The materials have in common that they are handled in the form of particles of several μm to mm. The reaction is conducted in reactors, where it can be operated by regulating the pressure of the reactive gas and temperature.

1.2.4 Reactor Concepts for Thermochemical Heat Storage

The reactor forms the environment where the thermochemical reaction takes place in a targeted, controlled way. It consists of a casing that contains the solid reaction material, and heat and reaction fluid are dosed or extracted into that casing. The reactor can therefore be optimized to provide or subtract them both in the best possible way.

Different reactor concepts are presented and summarized e.g. in [Pan and Zhao, 2017]. They range from fluidized bed reactors [Criado et al., 2014, Angerer et al., 2018] over flow reactors [Kerskes et al., 2012] to fixed-bed reactors.

In this work, we restrict ourselves to fixed-bed reactors. This means the solid reactive bulk is rigid. There are two different basic types of bed reactors: the directly operated and the indirectly operated fixed-bed reactor concepts.

Directly Operated Reactor Concept

Figure 1.3 shows the directly operated reactor concept presented by [Schaube et al., 2013a] in the experimental setup and as sketch. The solid reaction material is filled into a tube. A filter at the bottom keeps the solid material at its place. From the bottom, a mixture of heat transfer fluid (HTF) and gaseous reactant is injected and flows through the porous bulk to the top, providing heat and reactant at the same time. The gas flux is small enough so that the solid material does not move. The gas leaves the reactor at the top, reduced or enriched by the gaseous reactant. A pressure gradient between bottom and top induces the gas flux.

This reactor type requires no heat exchanger, as the reaction fluid is the same as the heat transfer fluid. Thereby, it creates a very good heat transfer through the reactor. The partial pressure of the gaseous reactant can be adjusted by the gas composition. The only disadvantages are parasitic losses caused by a pressure drop in the porous bulk.

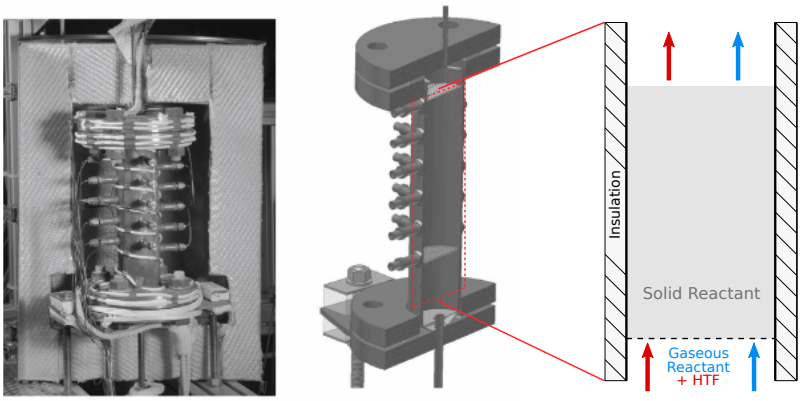

Figure 1.3: Experimental setup[1] and schematic view on the reactor of [Schaube et al., 2013a]

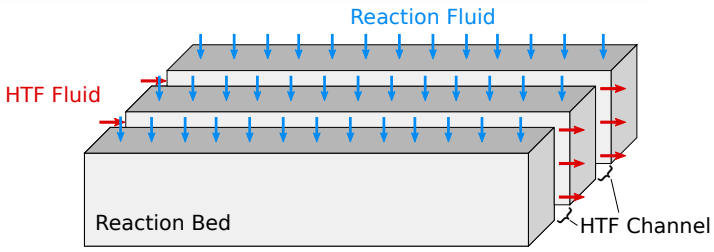

(a) Schematic view of the reactor showing the reactive beds, heat transfer (HTF) channels and fluid, and the reaction fluid flow, adapted from [Schmidt et al., 2014]

(b) Top view of the experimental setup of [Schmidt et al., 2014][2]

Figure 1.4: Indirectly operated reactor concept

Indirectly operated Reactor Concept

In contrast to the previous reactor type, the indirectly operated reactor provides heat and reaction fluid separately from each other. Again, the solid bulk material is packed in beds, see Figure 1.4. Heat transfer channels are integrated into the bed, where a heat transfer flux provides heat. The heat transfer fluid has no direct contact to the reacting substances. Reaction fluid is delivered from the top and/or the bottom to the solid bulk.

[1] Reprinted from "Chemical Engineering Research and Design, 91, F. Schaube et al. De- and rehydration of $Ca(OH)_2$ in a reactor with direct heat transfer for thermo-chemical heat storage. Part A: Experimental results, 856–864, 2013", with permission from Elsevier.

[2] Reprinted from "Applied Thermal Engineering, 62, M. Schmidt et al., Experimental results of a 10 kW high temperature thermochemical storage reactor based on calcium hydroxide, 553-559, 2014", with permission from Elsevier.

1.3 Objectives

This thesis aims at providing a numerical simulator for fixed-bed thermochemical reactors. The processes in the reactors are manifold and depend on each other in a complex manner. Modeling is thereby primarily a tool to proof understanding and to identify all the relevant processes occurring in the thermochemical reactor. Furthermore, it provides a cheap tool to test the influence of different processes. With the modeling, we aim to promote thermochemical heat storage. Afterwards, this simulator should also be able to help designing and optimizing fixed-bed reactors.

We focus on one specific reaction system, namely the reaction of Calcium oxide with water to Calcium hydroxide ($CaO/Ca(OH)_2$). This reaction system has been investigated intensively on different scales and provides a good foundation both on the material parameters [Schaube et al., 2011, 2012], the reaction behaviour [Criado et al., 2014, Schaube et al., 2012, Angerer et al., 2018] and specific processes occuring on the reactor scale [Schaube et al., 2012, Roßkopf et al., 2014, Yan et al., 2019]. Experimental data are available for validating the numerical model on the reactor scale (e.g. Schmidt et al. [2017]).

The simulator needs to depict the relevant processes occuring in the reactor including flow and transport of reaction gas and heat transfer fluid, the chemical conversion of the solid reactive bulk, including the heat development and transport, for both types of fixed-bed reactors. The two reactor concepts display different modeling requirements. For the directly operated reactor concept, the gas mixture and gas flow processes are important. For the indirectly operated concept on the other hand, heat transfer channel and reactor bulk form two domains with very diverse prevailing processes. Both reactor types should be simulated in an accurate and effective manner. Besides, we use the numerical model to investigate the importance of including or neglecting specific processes. Model verification by comparing different numerical models in a benchmark, and model validation by comparing simulation and experimental results, produce proof of our numerical model.

1.4 Outline

In Chapter 2, we investigate the exact physical and chemical processes occurring in the bulk of fixed-bed thermochemical heat storage reactors. We approximate the bulk as a porous medium and present the assumptions related to this concept being incorporated into the conceptual model. The ensemble of processes forms the phyiscal and chemical model for the reactors. Those processes are integrated into balance equations to form a mathematical model in Chapter 3. The balance equations are of the type of partial differential equations, which need to be solved numerically. We present the numerical models including discretization methods and solution strategies. Chapter 4 is dedicated to simulating the directly operated reactor concept. Here we verify the model in a benchmark setup with different software packages. Section 4.1 presents the findings that have been published jointly with T. Nagel in P. Ostermeier in [Nagel et al., 2018]. Subsequently, we test the influence of the simplifying assumptions concerning local thermal equilibrium and morphology changes in solid bulk with numerical experiments. Section 4.3 presents the findings on reversible porosity induced permeability alterations published in [Seitz et al., 2020]. In Chapter 5, we present simulation results for the indirectly operated reactor concept. We aim to validate the model with experimental data of [Schmidt et al., 2017]. In the experimental setup, uncontrolled heat losses occur that influence the reaction behaviour. With the aproach of inverse modeling, we aim to approximate the underlying processes. The results presented here are published in [Seitz et al., 2021]. In Chapter 6, we conclude our findings and give an outlook.

2 Fundamentals

Modeling fixed-bed thermochemical heat storage reactors necessitates understanding the different physical and chemical processes occuring in the porous bulk. The ways to describe and quantify those processes depend on the scale one looks at them. In this chapter, we introduce the different physical and chemical processes necessary to describe the bulk of reactive particles in a fixed-bed reactor. This includes the transport processes as well as the chemical reaction. To do so, we need to introduce the quantities we use for describing the processes. Additionally, we present the specifications of the reaction system $CaO/Ca(OH)_2$.

2.1 Scales, Phases and the Porous Medium

It is necessary to define scales, for each scale has its own properties to describe matter and processes. Chemical reactions like the reaction of Equation 1.1 are the result of interactions between molecules that are so strong, that they lead to a change in their molecular structures. Less intense interactions regulate the arrangement of molecules, e.g. by attraction forces and polarity. These processes are looked at on the *molecular scale*. Every molecule has own properties pertaining to mass, momentum and energy. However, it is computationally unfeasible to model every single molecule within the complete reactor.

Averaging over a sufficient number of molecules leads to the definition of continuous *phases*. A phase occupies a defined space and has, within its domain, continuous properties. A phase is defined by state variables, such as composition, pressure and temperature. Different phases are separated by interfaces. In the present work, we consider a gas phase composed of at least one component (B) and different solid phases (A, and AB). Due to the continuous properties, this scale is termed *continuum scale* [Bear,

2018]. The differentiation between different phases allows to describe the materials visually. The considered solids form particles. Several particles form a solid matrix. The void space (also: the pores) in between the particles is occupied by the gas phase. So, the aggregate of solid matrix and gas-filled pores is termed *porous medium*. Another name for the continuum scale is thus *pore scale*.

The number of particles within a thermochemical reactor is still too large to be resolved in a numerical model. In order to upscale, the quantities within a specific volume are averaged. This volume needs to be chosen in such a way that shifting, in- or decreasing it slightly doesn't cause any change in the describing quantities. It needs to be large enough, so that small characteristics of geometry and composition are represented and considerably smaller than the overall domain. Bear [2018] gives a rough number of 100 times smaller than the simulated domain. This volume is then termed *representative elementary volume* (REV) and the according scale, the *REV scale* [Bear, 2018, Helmig et al., 1997]. Again, due to the upscaling, new parameters arise, such as porosity and permeability. In a REV, all the present phases are continuous, albeit each phase is attributed with a volume fraction. Several continuous phases overlap.

Figure 2.1 illustrates that the same system can be viewed from different scales. Each scale has its own properties to describe matter and processes. Due to upscaling, information of the smaller scale gets lost and new averaged parameters, and also processes, appear. In the system of a complete thermochemical reactor, however, small scale information such as specific pore morphologies at every location are not available anyway. Temperature measurements deliver an average temperature of gas and solid. Modeling on the REV scale requires information on properties of the same scale [Bear, 2018]. Data of smaller scales need to be transferred to the scale of interest by averaging or homogenization techniques [Bear, 2018].

2.2 The Fluid-filled Porous Medium

A porous medium consists of at least one solid and one fluid phase. The phase in turn is composed of one or several chemical species, so-called components. We introduce ways to describe the composition and further properties that describe the phases. Ad-

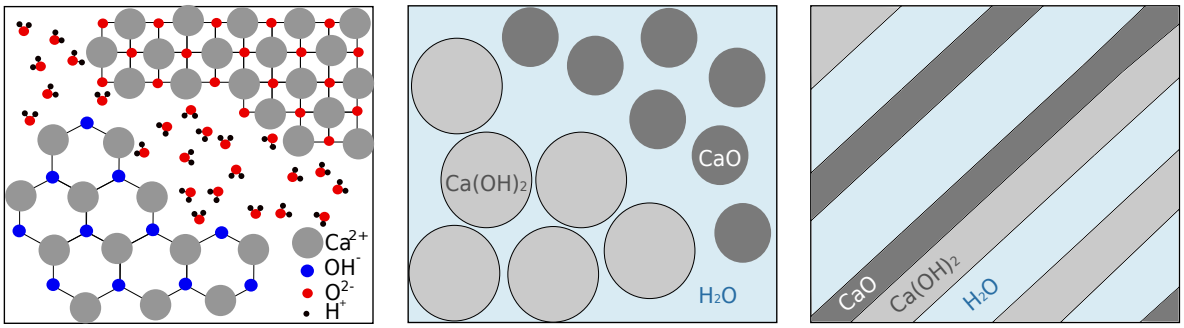

Figure 2.1: Different scales for describing the same systems for the example of the reaction system $CaO/Ca(OH)_2$; **Left:** Molecular scale with CaO and $Ca(OH)_2$ crystals, and water molecules; **Middle**: Micro / pore scale: Continuous phases of solid grains and gas, **Right**: REV scale: The considered volume is filled by volume fractions of the two solids CaO and $Ca(OH)_2$ and the water vapor.

ditionally, we introduce parameters to specify the fluid-filled porous medium on the REV scale.

Mole and Mass Fractions Mole and mass fractions indicate the proportion of one component within the phase. The mole fraction x_κ is thereby the ratio of the number of moles n of a specific component κ within a phase composed of i different chemical species. The mass fraction X_κ relates the mass of the component m_κ to the total mass of the phase m:

$$x_\kappa = \frac{n_\kappa}{\sum_i n_i}, \qquad X_\kappa = \frac{m_\kappa}{m}. \tag{2.1}$$

These definitions generally apply for every phase. In this work we assume though, that the solid phases consist of only one component.

Mass and mole fractions can be converted into each other by the molar mass of a component M_κ.

$$X_\kappa = \frac{x_\kappa M_\kappa}{\sum_i x_i M_i}. \tag{2.2}$$

The sum of mole and mass fractions over all components of a phase is always 100 %.

Partial Pressure According to Dalton's law, the ratio of one component's pressure to the total gas phase pressure is the same as the component's mole fraction in that gas

phase. Thus, it defines the partial pressure as follows:

$$p_\kappa = x_\kappa p. \tag{2.3}$$

The sum of all partial pressures yields the pressure of the gas phase,

$$p = \sum_\kappa p_\kappa. \tag{2.4}$$

Dalton's law assumes thus, that the different components don't interact. It is therefore only valid for ideal gases.

Density The density ρ of a substance is defined as weight of the substance per volume. Similarly, the molar density ρ_m is defined as amount of moles n within a specific volume V:

$$\rho_m = \frac{n}{V}. \tag{2.5}$$

In this work, the density of a solid is assumed to be constant in pressure and temperature. All gases are assumed to behave ideally. The gas density ρ_g (with respect to mass) is determined by the ideal gas law as follows:

$$\rho_g = \frac{p_g M_g}{RT} = \frac{p}{R_g T}, \tag{2.6}$$

with $R = 8.314 \frac{\mathrm{J}}{\mathrm{mol\,K}}$ the univeral gas constant, $R_g = R/M_g$ the specific gas constant, p the pressure and T the absolute temperature.

Viscosity A moving fluid within a rigid porous matrix is faced to shearing at the fluid-solid-interfaces. The resistance of the fluid to shear stress is termed dynamic viscosity μ. For Newtonian fluids, it is determined as constant of proportionality for shear stress τ_s and the velocity gradient:

$$\tau_s = \mu \frac{dv_x}{dy}. \tag{2.7}$$

The viscosity depends on pressure, temperature and composition. For single component gases, viscosity values are tabulated or determined by empirical relations, such as

[IAPWS, 2003] for water and [Reid et al., 1987] for nitrogen. Wilke's law determines the viscosity for gas mixtures [Reid et al., 1987] for a gas composed by two components (i,j) at given temperature, pressure and composition:

$$\mu(i,j) = \frac{x_i \cdot \mu_i}{x_j \cdot \mathbf{p}_{i,j}} + \frac{x_j \cdot \mu_j}{x_i \cdot \mathbf{p}_{j,i}}, \quad \text{with} \quad \mathbf{p}_{i,j} = \frac{(1 + \sqrt{\frac{\mu_i}{\mu_j}}(\frac{M_j}{M_i})^{1/4})^2}{\sqrt{8(1 + \frac{M_i}{M_j})}}. \tag{2.8}$$

Volume Fractions The ratio of the volume V_i that a specific phase i occupies within a considered volume V_{total}, defines the volume fraction θ_i of the phase i,

$$\theta_i = \frac{V_i}{V_{total}} \qquad i \in \{\text{gas}, \text{solid}_1, \text{solid}_2\}. \tag{2.9}$$

The sum of all the phases present in the considered volume fills the total volume, thus all volume fractions θ_i sum up to one. The volume fraction of gas, i.e. the pore volume within the total volume, is also termed *porosity* ϕ. This definition holds for the present case of solid-gas-reactions, if the gas phase is the only fluid phase.

Interfacial Area Different phases meet each other at their interfaces. As pore scale information is not available on the REV scale, Shi and Wang [2011] present an empirical formulation to determine the interfacial area a_{sg} between solid and gas within a REV based on the porosity ϕ and the average grain size diameter d_p:

$$a_{sg} = 6\frac{(1-\phi)}{d_p}. \tag{2.10}$$

This relation considers only one solid phase. For the usage within this work this shall be sufficient.

Tortuosity Following the pores in a porous medium, a longer path is needed to connect two points than with a straight line. This deviation in distance is termed tortuosity [Helmig et al., 1997]. Millington and Quirk [1961] provide the following formula to quantify the tortuosity τ for a porous medium filled with a single fluid based on the porosity ϕ:

$$\tau = \phi^{4/3}. \tag{2.11}$$

Intrinsic permeability The collocation of the solid particles and their surface roughness determine how permeable the porous medium is to fluid flow. This is accounted for by the intrinsic permeability $\mathbf{K}$. If the permeability depends on the flow direction, the intrinsic permeability is a tensorial quantity. For all the materials considered in this work however, we assume isotropic conditions. This assumption reduces the tensor to a scalar quantity.

The intrinsic permeability can be deduced from values of measured hydraulic conductivity with known fluid properties based on Darcy's law (see Equation 2.48). Furthermore, the intrinsic permeability can be estimated with empirical relations based on known porous medium properties. The most well-known of these is the relation of Kozeny and Carman [Carman, 1997].

$$\mathbf{K} = \frac{\zeta^2 d_p^2}{180} \frac{\phi^3}{(1-\phi)^2}, \tag{2.12}$$

with ζ_s the sphericity and d_p the characteristic particle diameter. Le Gallo et al. [1998] state that this equation is not accurate, however according to Nield and Bejan [2013] it is sufficiently accurate for spherical particles with little variation in grain size.

If the porous medium undergoes alterations such as a chemical conversion, its porous medium properties may change. Most materials suitable for thermochemical reaction feature a solid volume change and thereby a change in porosity during the reaction. A change in porosity however, alters the resistance to flow as it affects the void space available for the fluid in a porous medium. A porous medium undergoing such morphological changes can show different alterations of its texture, such as in the size of the pore cavities, pore throats, or the internal roughness. Different approaches exist that relate the change in porosity to a change in permeability [Hommel et al., 2018]. The most well-known among those is also the relation of Kozeny and Carman. In order to track the permeability change due to a change in porosity, Hommel et al. [2018] provide the following modified form of the Kozeny-Carman equation (Eq. 2.12:

$$\frac{\mathbf{K}}{\mathbf{K}_0} = \frac{\phi^3(1-\phi_{0,g}^2)}{\phi_{0,g}^3(1-\phi)^2}, \tag{2.13}$$

with initial porosity $\phi_{0,g}$ and permeability $\mathbf{K}_0$. This relation has the advantage, that it does not require further parameters.

Though the Kozeny-Carman relation is already used in this context, e.g. in [Shao et al.,

2013], there are also other relations that are supposed to reflect the process better. Hommel et al. [2018] and Bernabé et al. [2003] list within those the general power-law relation:

$$\frac{\mathbf{K}}{\mathbf{K}_0} = \left(\frac{\phi}{\phi_0}\right)^{\gamma}, \tag{2.14}$$

with the exponent γ that can be adapted to the process. For chemical alteration, Bernabé et al. [2003] list $\gamma > 10$.

We will address this effect in a numerical experiment in Section 4.3.

2.3 Thermodynamics of Solid-Gas Reactions

The reactive bed of a thermochemical heat storage system forms a thermodynamical system. Thermodynamics is concerned with the transfer and transformation of energy in matter [Atkins and De Paula, 2014]. In this section, we introduce fundamental thermodynamical concepts to describe systems and processes. Based on those, we regard the equilibrium conditions for thermochemical reactions and reaction kinetics.

2.3.1 State Variables, State Functions and Process Variables

Thermodynamical systems are uniquely defined by a set of state variables, namely temperature T, pressure p, volume V, mass/amount of substances m/n and their compositions X_i/x_i. State functions, such as internal energy U or enthalpy H, relate the state variables and describe changes of the system, exemplarily due to a thermochemical reaction.

On the molecular scale, the molecules and their atoms are moving due to Brownian motion. On the continuum scale, this effect is observed as temperature of the phase. The amount of energy due to this phenomenon is described by the state variable internal energy U. According to the first law of thermodynamics, the internal energy is only changed, if heat Q is added to (or respectively removed from) and/or work W is done by or on the system:

$$\Delta U = Q + W. \tag{2.15}$$

The quantity relative to the material's mass is termed specific internal energy $u = U/m$. The definitions of the specific heat and work are accordingly $q = Q/m$ and $w = W/m$. Other than the internal energy, heat and work are process variables. They depend on the path from one state to the other.

Work is defined by a displacement of the system Δx against an opposing force F. Volume expansion is one type of work, that a gas performs, if its volume increases from the volume V_1 to V_2 against the constant pressure p of the surroundings,

$$W = -\int_{V_1}^{V_2} p dV. \tag{2.16}$$

Heat is defined by the energy flux that occurs, if the system's temperature is different to the temperature of the surroundings. It is described below in Equation 2.20. If heat is added to a system, it may partly be converted to perform work. Therefore, the definition of another state variable is advantageous, especially for such systems, that are able to change their volume. The *enthalpy* is defined by internal energy, pressure and volume as follows:

$$H = U + pV. \tag{2.17}$$

At constant pressure, the heat added to the system equals the change in enthalpy.

$$\Delta H = Q. \tag{2.18}$$

If heat is added to a system, its temperature rises, unless a phase change occurs, and its enthalpy increases. The heat capacity gives information on how much heat is stored in a system at a given temperature difference. The isobaric heat capacity is defined by the partial derivative of the enthalpy H with respect to the temperature:

$$C_p = \left.\frac{\partial H}{\partial T}\right|_p. \tag{2.19}$$

In this work, we assume that the solid volume is constant with pressure and temperature. Thus, isobaric and isochoric heat capacities are the same: $C_{p,s} = \left.\frac{\partial H}{\partial T}\right|_p = \left.\frac{\partial U}{\partial T}\right|_V$. We divide C_p by the system's mass to yield the specific heat capacity $c_p = C_p/m$. For a constant heat capacity and no phase change, the heat at

constant pressure is thus determined to

$$Q = C_p \Delta T. \tag{2.20}$$

In this work, we assume the solids to be incompressible and their heat capacity to be constant with temperature. In this way, the heat capacity is considered a property, that can be used to determine the enthalpy change for a solid given a temperature change.

The enthalpy of a system changes not only through added heat or volume expansion, but also through phase changes or chemical reactions. We distinguish *exothermic* processes that add heat to the system, and *endothermic* reactions that absorb heat from the system. Usually, the reaction enthalpy is measured by calorimetric devices, where the pressure is constant [Gedde, 2020] and thus, the enthalpy is determined by the heat provided/produced to perform the reaction. The enthalpy change of a chemical reaction is preferentially given as specific molar enthalpy of reaction Δh_R [$\mathrm{J\,mol^{-1}}$] and is thus independent of the amount of substance. As the enthalpy is a state function, the change in enthalpy does not depend on the reaction pathway. This means, that the enthalpies of intermediate reaction products cancel out, if they are consumed in the course of the reaction. For most substances, the enthalpies of formation at standard conditions are tabularised, see e.g. in [Barin, 1995]. The standard state of the considered substances, ideal gas and pure solid, are defined by the pressure of 1 bar and the temperature of 298.15 K. This state is denoted by the superscript 0. The reaction enthalpy of a chemical reaction at standard conditions can be determined by the sum of the enthalpies of formation according to the stoichiometric coefficients of the reaction equation ν_i:

$$\Delta h_R^0 = \sum_i \nu_i \Delta h_{F,i}^0. \tag{2.21}$$

To yield the reaction enthalpy assuming complete conversion at reaction temperature T_1, the heat due to the temperature difference between standard and reaction temperature needs to be added according to Kirchhoff's law:

$$\Delta h_R = \Delta h_R^0 + \int_{T^0}^{T_1} \sum_i \nu_i c_{pm,i} dT, \tag{2.22}$$

with the molar heat capacities of the pure substances $c_{pm,i}$.

Systems can perform work with their internal energy. To determine the amount of work

a system is able to perform, we introduce the state function entropy S. According to the second law of thermodynamics, the entropy increases if a system undergoes changes but no work is added. The difference in enthalpy of a reversible change from state (1) to state (2) is defined by

$$\Delta S = \int_{(1)}^{(2)} \frac{dQ_{rev}}{T}, \tag{2.23}$$

with Q_{rev} the reversible heat exchange. Similar to the enthalpy of reaction, the entropy change associated to a chemical reaction can also be determined by the individual components at standard conditions

$$\Delta s_R^0 = \sum_i \nu_i \Delta s_{R,i}^0. \tag{2.24}$$

Again, we used here the lower case letter for the specific molar quantity s.

Spontaneous processes increase the entropy of a system. For determining, whether a process, such as a chemical reaction, happens spontaneously, we introduce the Gibbs free energy for systems at constant pressure, G:

$$G = H - TS. \tag{2.25}$$

If ΔG is negative, the process occurs spontaneously, zero for equilibrium, and positive, if energy is needed to run the process.

The partial derivative of the Gibbs free energy with respect to the amount of the component i defines the chemical potential of i:

$$\psi_i = \left.\frac{\partial G}{\partial n_i}\right|_{p,T,n_{j\neq i}}. \tag{2.26}$$

At constant pressure and temperature, ΔG indicates the reversible work other than volume expansion that can be performed by the system and a change in Gibbs free energy is due to a change in composition:

$$\mathrm{d}G = \psi_i \mathrm{d}n_i + \psi_j \mathrm{d}n_j + ... = \sum_\xi \psi_\xi dn_\xi, \tag{2.27}$$

with d the total differential and the components (i, j, ..., ξ).

Combining the definition of the enthalpy (Eq. 2.17) and Gibbs free energy (Eq. 2.25) and reordering them, yields

$$U = -pV + TS + G \tag{2.28}$$

With the help of the chemical potentials ψ_i, we are now able to show, that a change in internal energy also depends on the composition:

$$\begin{aligned} \mathrm{d}U &= -p\mathrm{d}V - V\mathrm{d}p + S\mathrm{d}T + T\mathrm{d}S + \mathrm{d}G \\ &= -p\mathrm{d}V - V\mathrm{d}p + S\mathrm{d}T + T\mathrm{d}S + (V\mathrm{d}p - S\mathrm{d}T + \sum_{\xi} \psi_{\xi}\mathrm{d}n_{\xi}) \\ &= -p\mathrm{d}V + T\mathrm{d}S + \sum_{\xi} \psi_{\xi}\mathrm{d}n_{\xi}. \end{aligned} \tag{2.29}$$

The change in Gibbs free energy ΔG due to a reaction is given by the released reaction enthalpy ΔH_R and the entropy production ΔS_R at constant pressure.

$$\Delta G_R = \Delta H_R - T\Delta S_R. \tag{2.30}$$

If the entropy production is sufficiently high, even endothermic reactions can occur spontaneously.

2.3.2 Solid-Gas Reactions at Equilibrium

For thermochemical heat storage, we consider solid-gas reactions that take place endothermically for the charge and exothermically for the discharge reaction.

High reaction enthalpies are favorable to reach high energy storage densities. According to [Schaube, 2013], furthermore the temperature of the thermochemical reaction is important for the application. Moderate temperatures are beneficial for many applications. According to Equation 2.30, a negative entropy production enables moderate temperatures for the same free energy both for the charge and the discharge reaction. Dissociation reactions, and therein especially solid-gas reaction systems, feature both, high reaction enthalpies and negative entropy productions [Schaube, 2013]. The Gibbs free energy of a reaction at reaction conditions is determined based on the Gibbs free energy at standard conditions (p = 1 bar, T = 298.15 K) and the Gibbs free energy

contained in the difference of pressure and temperature. For ideal gases, this difference is determined as follows in terms of the chemical potential:

$$\psi_i = \psi_i^0 + RT\ln\left(\frac{p_i}{p^0}\right). \tag{2.31}$$

The Gibbs free energy of the reaction results to

$$\begin{aligned}\Delta G_R &= n\sum_i \nu_i\psi_i^0 + nRT\sum_i \nu_i \ln\frac{p_i}{p^0} \\ &= \Delta G_R^0 + nRTln\prod_i\left(\frac{p_i}{p^0}\right)^{\nu_i}.\end{aligned} \tag{2.32}$$

At equilibrium, the amount of forward reaction equals the amount of backward reaction. Equation 2.32 results to

$$0 = \Delta G_R^0 + nRT\ln\prod_i\left(\frac{p_i}{p^0}\right)^{\nu_i}, \tag{2.33}$$

where the product $\prod_i \left(\frac{p_i}{p^0}\right)^{\nu_i}$ is referred to as equilibrium constant K_{eq}:

$$K_{eq} = \prod_i\left(\frac{p_i}{p^0}\right)^{\nu_i}. \tag{2.34}$$

For real gases, K_{eq} is determined by activities instead of the partial pressures. In this work, however, we assume the gases to behave ideally. We rearrange Equation 2.33 and reinsert Equation 2.30 to yield the van't Hoff equation:

$$\ln K_{eq} = -\frac{\Delta h_R^0}{RT} + \frac{\Delta s_R^0}{R}. \tag{2.35}$$

For solid-gas reactions of the type of Equation 1.1 it is generally assumed, that the reaction enthalpy and entropy are independent of the temperature [Atkins and De Paula, 2014]. For only one gaseous component B, Equation 2.35 simplifies to

$$\ln\left(\frac{p_B}{p^0}\right) = -\frac{\Delta h_R^0}{RT} + \frac{\Delta s_R^0}{R}. \tag{2.36}$$

The Van't Hoff equation (Eq. 2.36) describes a linear relation between the logarithm of the gas pressure p_B and the inverse of the temperature at equilibrium. The slope

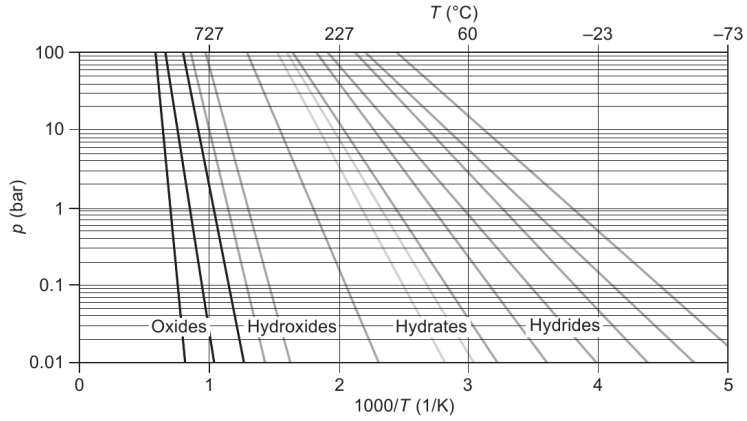

Figure 2.2: The van't Hoff equation for different types of gas solid reaction systems plotted by [Linder, 2015][1]

represents the reaction enthalpy, and the intercept with the pressure axis the reaction entropy. According to [Atkins and De Paula, 2014], the assumption of a constant reaction enthalpy is not accurate. However, this relation is often used, to determine the reaction enthalpy experimentally by determining the equilibrium conditions for pressure and temperature of a reaction [Atkins and De Paula, 2014].

Thus, the plot of the van't Hoff equation visualizes the characteristics of different possible reaction systems for thermochemical heat storage. Linder [2015] plotted the relation of equilibrium pressure and temperature for different reaction systems, as shown in Figure 2.2. For charging, the reaction conditions for pressure and temperature are adjusted to be left of the equilibrium line, i.e. at higher temperatures and/or pressures; for discharging, they are to the right of the equilibrium line. A heat pump effect is exploited, if charging is enforced at lower temperatures than the discharge [Richter et al., 2018]. Thus, in theory, the reaction system can be chosen appropriately according to the envisaged application for temperature and reaction enthalpy.

2.3.3 Fundamentals on Reaction Kinetics for Solid-Gas Reactions

Whereas the equilibrium condition can be derived from thermodynamic relations, the reaction kinetics are usually determined experimentally, see e.g. [Pijolat and Soustelle,

[1]Reprinted from "Advances in Thermal Energy Storage Systems, Woodhead Publishing Series in Energy, M. Linder, Using thermochemical reaction in thermal energy storage systems, 375 - 374, 2015", with permission of Elsevier.

2008], using thermogravimetry (TGA), differential scanning calorimetry (DSG) or differential thermal analysis (DTA). Besides, there are reaction kinetics based on purely theoretical considerations, e.g. by [Schmidt, 2011] for the reaction system $CaO/Ca(OH)_2$. In the experiments, the progress of the reaction is measured gravimetrically exploiting the fact, that the sample mass changes, when the gaseous component leaves or enters the solid phase. Thus, also the conversion X_s is usually expressed in terms of mass fractions (see [Khachani et al., 2014]):

$$X = \frac{m_0 - m_t}{m_0 - m_\infty}, \tag{2.37}$$

with m the mass of the sample at times 0, t and end (∞).

According to Vyazovkin et al. [2011], the general form of reaction kinetics for thermally stimulated processes can be split into three independent terms: a function of the temperature T, the conversion X and the pressure p.

$$k_R = k(T)f(X)f(p). \tag{2.38}$$

Some authors additionally consider the influence of the average particle size d_p. The temperature term is usually described by the Arrhenius equation [Vyazovkin et al., 2011] with a pre-exponential parameter A and the activation energy E:

$$k(T) = A\ exp\left(\frac{-E}{RT}\right). \tag{2.39}$$

For the two other terms $f(X)$ and $f(p)$, different models exist that suggest reaction mechanisms, such as the shrinking core or the nucleation and growth model (see e.g. [Khachani et al., 2014]). They are identified by comparing the experimental data on pressure, temperature and conversion changes to those model concepts and by fitting the individual parameters.

With the change in overall solid density, we formulate the reaction rate q_R based on the reaction kinetics k_R:

$$q_R = \nu_i(1 - \phi)(\rho_{AB} - \rho_A)k_R, \tag{2.40}$$

for the two solids A and AB. ν_i are the stoichiometric coefficients according to the

reaction equation. The term $(1 - \phi)$ accounts for the fact, that the reaction occurs in the solid phase of the reaction bulk.

2.4 Transport Processes in a Porous Medium

Local differences in the state variables (i.e. pressure, temperature and composition) are the driving forces for fluxes. According to the theory of Onsager, fluxes are coupled, i.e. a mass flux induces a heat flux and vice versa [Kjelstrup et al., 2010]. In this work, we apply a phenomenological approach to describe the fluxes as presented in [Bear, 2018].

2.4.1 Diffusion

Transport of a substance due to a concentration gradient is termed diffusion. For binary systems, this is described by Fick's Law. There are different formulations of Fick's law for different reference systems. According to [Taylor and Krishna, 1993], Fick's law in a mass-reference system is given by

$$\mathbf{j}_d^\kappa = -D^\kappa \rho \nabla X^\kappa. \tag{2.41}$$

The law assumes, that the fluxes for each of the components is of the same magnitude but of different sign. The net flux is thus zero. The binary diffusion coefficient D^κ is determined with Fuller's method [Reid et al., 1987], dependent on pressure, temperature and the molecular weights and atomic diffusion volumes of the mixture's substances.

In a porous medium, the gas has to travel a longer distance to overcome the concentration gradient due to tortuosity. Thus, the porous medium diffusion coefficient is the following according to [Helmig et al., 1997]:

$$D_{pm} = D\tau\phi. \tag{2.42}$$

In porous media viewed on the macro scale, a transport effect similar to diffusion is observed: Dispersion smears out concentration gradients due to fluctuations and distortions in the velocity field. Kobus et al. [1992] present methods to quantify dispersion

effects for groundwater applications. In this work however, we don't account for dispersion.

2.4.2 Heat Conduction

Similar to the molecular diffusion due to a concentration gradient, a temperature gradient induces a heat flux. Fourier's law delivers the following relation:

$$\mathbf{j}_{e,d} = -\lambda \nabla T. \tag{2.43}$$

The heat conductivity λ is a material property. For solids, it is constant. For gases, it depends on temperature, pressure and composition. The gas mixture heat conductivity is yield by adding the pure gas property weighted by the mole fractions.

Woodside and Messmer [1961] present different laws to determine the overall porous medium heat conductivity λ_{eff}. We chose the volumetric arithmetic mean of the different phases as follows:

$$\lambda_{\text{eff}} = \sum_i \theta_i \lambda_i. \tag{2.44}$$

According to [Woodside and Messmer, 1961] this is sufficiently accurate for conductivity ratios of fluid to solid in the range of $\lambda_f/\lambda_s = 0.4$ as it is fulfilled for the substances considered in this work.

2.4.3 Heat Transfer

Heat transfer occurs at the surface between a solid and a moving fluid of different temperatures. This occurs either in the porous medium, if the solid grains are of different temperature than the surrounding fluid, or at internal boundaries, such as the heat transfer channel in the setup of the indirectly operated reactor concept. The moving fluid develops a laminar boundary layer that limits the heat flux driven by the different temperatures. The heat transfer flux is determined as follows:

$$\mathbf{j}_{e,\text{HTF}} = \alpha_{\text{HTF}}(T_F - T_S), \tag{2.45}$$

with the convective heat transfer coefficient α_{HTF}, the temperatures of the fluid T_F and the solid T_S. $\mathbf{j}_{e,\mathrm{HTF}}$ delivers a heat flux per area. It is multiplied by the surface area to gain the total heat flux. For heat transfer within the porous medium, the solid surface area corresponds to the interfacial area a_{sg}, that is presented in equation 2.10.

α_{HTF} depends on fluid properties and the flow regime. There are approaches to determine α_{HTF} based on the similarity method with the dimensionless Nusselt number, $Nu = \frac{\alpha_{\mathrm{HTF}} D}{\lambda_g}$, with D, the hydraulic diameter.

In a porous medium, Wakao and Kagei [1982] defined the Nusselt number as follows:

$$\mathrm{Nu} = \frac{\alpha_{\mathrm{HTF}} L}{\lambda} = 2.0 + 1.1\mathrm{Pr}^{1/3}\ \mathrm{Re}^{0.6}, \tag{2.46}$$

with the dimensionless Prantl (Pr) and the Reynolds Number (Re). The dimensionless numbers are defined in Section 2.4.6.

For the case of a rectangular heat transfer channel, such as it occurs in the indirectly operated reactor concept, there are different concepts to determine the Nusselt number: [Incropera, 2013] suggest a fixed Nusselt number depending only on the geometry of the channel. Gnielinski [2010] gives the following equation for a channel with hydrodynamically developed laminar flow:

$$\mathrm{Nu} = (7.541^3 + (\mathrm{Re}\ \mathrm{Pr}\ d_h/L)^3)^{1/3}, \tag{2.47}$$

with L the length of heat transfer. The importance of an accurate description of the heat transfer coefficient will be addressed in Chapter 5.

2.4.4 Advection

A pressure gradient within a fluid phase induces a fluid flux. Based on sand column experiments (in 1856), Henry Darcy developed a law to describe the flux in a porous medium. Later it was validated also for compressible fluid fluxes, see e.g. [Bear, 2018]. It relates the pressure gradient linearly to the fluid flux with the permeability $\mathbf{K}$ as scaling factor:

$$\mathbf{v} = -\frac{\mathbf{K}}{\mu_g}(\mathrm{grad}\, p - \rho \mathbf{g}), \tag{2.48}$$

with $\mathbf{g}$ the gravitational constant. As the reactors, we consider in this work, have small dimensions, we neglect the gravity term ($-\rho\mathbf{g}$). The Darcy-velocity $\mathbf{v}$ describes a flux per intersection. The average fluid velocity is obtained by dividing $\mathbf{v}$ by the porosity. Darcy's law is only valid for creeping flow, i.e. $Re < 1$. Furthermore, it assumes a rigid solid and no-slip at the microscopic fluid-solid interface [Bear, 2018].

The moving fluid transports the containing components and the inherent phase energy along and effects thus advective transport. The advection of the component κ is determined as follows:

$$\mathbf{j}_a^\kappa = \mathbf{v}\rho X^\kappa, \tag{2.49}$$

and the energy advection accordingly as

$$\mathbf{j}_e^a = \mathbf{v}\rho h = \mathbf{v}(\rho u + p). \tag{2.50}$$

$\mathbf{j}_a^e$ contains thus the transport of internal and kinetic energy contributions.

2.4.5 Knudsen Diffusion

For gases, the assumption of no-slip is not always fulfilled. Especially if the pores are small and pressure is low, molecular collisions between the fluid and the solid become more probable and slippage occurs on the solid surface. The Knudsen number,

$$\mathrm{Kn} = \frac{l_{\mathrm{mol}}}{L_{\mathrm{char}}}, \tag{2.51}$$

gives evidence, whether this process is important, with: l_{mol} mean free path of the fluid molecules and L_{char} characteristic length of the porous medium. [Mewes and Mayinger, 2005] present a version of the Knudsen number based on macroscopic quantities:

$$\mathrm{Kn} = \frac{1}{L_{\mathrm{char}}}\sqrt{\frac{\pi}{2}}\frac{\mu}{\rho_g}\frac{1}{\sqrt{R_g T}}. \tag{2.52}$$

If the mean path of the molecule is in the same order of the pore size, the so-called Knudsen diffusion becomes important. [Ziarani and Aguilera, 2012] categorized the following regimes:

- $\mathrm{Kn} \leq 0.01$: no-slip
  Viscous flow dominates and the Knudsen diffusion is negligible
- $0.01 \leq \mathrm{Kn} \leq 0.1$: slip flow
  Gas molecules experience slipping at the solid interface. This is accounted for as a modification to Darcy's law e.g. by the Klinkenberg extension to permeability.
- $0.1 \leq \mathrm{Kn} \leq 10$: transition flow
  Both, slip and regular diffusion flow occur. This regime is best represented with Knudsen's diffusion.
- $10 \leq \mathrm{Kn}$: Equations for continuous flow are not valid anymore.

In the different experimental setups we study in Chapters 4 and 5, conditions are always in the range of "no-slip". For charge reactions in the indirect reactor setup, however, very small pressures are favorable to reach low charging temperatures. This fact is explained by the van't Hoff equation (Eq. 2.36) in Section 2.3.2. For such conditions, the Knudsen number rises up to 0.5, for which cases we present a method calculating the Knudsen diffusion flux in A.1.

2.4.6 Useful Dimensionless Numbers

Table 2.1 summarizes useful dimensionless numbers in the context of thermochemical heat storage and their meaning.

Table 2.1: List of dimensionless numbers

Name	Formula	Meaning
Reynolds number	$\mathrm{Re} = \frac{\mathbf{v} l_{\mathrm{ch}} \mu}{\rho}$	Ratio of inertia and viscous forces
Mach number	$\mathrm{Ma} = \frac{v}{a}$	Ratio between velocity and speed of sound
Prantl number	$\mathrm{Pr} = \frac{c_p \mu}{\lambda}$	Ratio between momentum and thermal diffusivity
Nusselt number	$\mathrm{Nu} = \frac{\alpha_{\mathrm{HTF}} L}{\lambda_g}$	Ratio between convective to conductive heat transfer
Knudsen Number	$\mathrm{Kn} = \frac{l_{\mathrm{mol}}}{L_{\mathrm{char}}}$	Ratio between the free path of a molecule to the pore size

2.5 The Reaction System CaO/Ca(OH)$_2$

The reaction of solid Calcium oxide (CaO) with water vapor to Calcium hydroxide ($Ca(OH)_2$) frames the reaction system CaO/$Ca(OH)_2$ with the following reaction equation.

$$CaO_{(s)} + H_2O_{(g)} \rightleftharpoons Ca(OH)_{2(s)},\ \Delta H_R = 104.4\ \text{kJ mol}^{-1} \tag{2.53}$$

This chemical reaction was investigated by several authors (see Sec. 2.5.2). Schaube et al. [2012] and Schaube [2013] studied additional material properties in detail that are necessary to model the reaction system on the reactor scale, such as heat capacity and conductivity. We will use these properties for modeling in this work if not indicated differently. Constant material properties of the solids are listed in Table 2.2. The properties of water vapor are elaborated in detail by [IAPWS, 1997]. For some reactor setups, an additional inert heat transfer fluid is mixed with the reaction gas. In the setups considered in this work, nitrogen is used as such a heat transfer fluid. The properties of the pure gases water vapor and nitrogen are listed in Table 2.3. Gas mixing laws for the different properties are listed in Table 2.4. In the following section, we give an overview of the specific behavior of the reaction system during reaction. Subsequently, we give a literature review on the formulation of the reaction kinetics.

Table 2.2: Constant properties of the the solid properties, CaO and $Ca(OH)_2$

Property	**Symbol**	**Value**	**Source**
Density $Ca(OH)_2$	$\varrho_{Ca(OH)_2}$	$2200\,\text{kg m}^{-3}$	Schaube et al. [2012]
Tabulated density CaO	ϱ_{CaO}	$3340\,\text{kg m}^{-3}$	Haynes [2010]
Grain size	d_{50}	$5.26\,\mu\text{m}$	Schaube et al. [2012]
Reference permeability	$\mathbf{K}$	$5 - 8.8{\cdot}10^{-12}\,\text{m}^2$	Schaube et al. [2012]
Specific heat capacity $Ca(OH)_2$	$c_{\text{p Ca(OH)}_2}$	$1530\,\text{J kg}^{-1}\,\text{K}^{-1}$	Schaube et al. [2012]
Specific heat capacity CaO	$c_{\text{p CaO}}$	$934\,\text{J kg}^{-1}\,\text{K}^{-1}$	Schaube et al. [2012]
Solid heat conductivity	λ_s	$0.4\,\text{W m}^{-1}\text{K}^{-1}$	Schaube et al. [2012]
Reaction enthalpy	ΔH_R	$104.4\,\text{kJ mol}^{-1}$	Schaube et al. [2012]

2.5.1 Processes Accompanying the Chemical Reaction

The reaction occurs at temperatures between 750 K (at 0.5 bar water vapor pressure) and 815 K (at 2 bar water vapor pressure), see Figure 2.6. During the reaction, the

Table 2.3: Properties of the gaseous components

Property	**H_2O**		**N_2**	
	Law	Source	Law	Source
Density	$\rho_{H_2O}(p,T)$	[IAPWS, 1997]	$\rho_{N_2}(p,T)$	ideal gas
Molar density	$\rho_{m,H_2O}(p,T)$	$= \rho_{H_2O}/M_{H_2O}$	$\rho_{m,N_2}(p,T)$	ideal gas
Viscosity	$\mu_{H_2O}(p,T)$	[Cooper and Dooley, 2008]	$\mu_{N_2}(T)$	[Poling et al., 2001]
Enthalpy	$h_{H_2O}(p,T)$	[IAPWS, 1997]	$h_{N_2}(p,T)$	$c_{p,N_2}(p,T) \cdot T$
Heat capacity	$c_{p,H_2O}(p,T)$	[IAPWS, 1997]	$c_{p,N_2}(p,T)$	method of Joback, [Reid et al., 1987]
Heat conductivity	$\lambda_{H_2O}(p,T)$	[IAPWS, 2011]	$\lambda_{N_2}(p,T)$	[Linstrom and Mallard]

Table 2.4: Properties of the gas phase

Property	**Gas mixture**
Density	$\rho_g = \rho_{H_2O} + \rho_{N_2}$
Molar density	$\rho_{m,g} = \rho_{m,H_2O} + \rho_{m,N_2}$
Viscosity	Wilke's law [Reid et al., 1987]
Enthalpy	$h_g = X_{H_2O} h_{H_2O} + X_{N_2} h_{N_2}$
Heat capacity	$c_{p,g} = X_{H_2O} c_{p,H_2O} + X_{N_2} c_{p,N_2}$
Internal energy	$u_g = h_g - p/\rho$
Heat conductivity	$\lambda_g = x_{H_2O} \lambda_{H_2O} + x_{N_2} \lambda_{g,N_2}$
Diffusivity	$D = f(p,T)$ with Fuller method [Reid et al., 1987]

solid material changes in volume by 50 % [Schaube, 2013]. This is due to the differences in the molecular structure of the two solids. $Ca(OH)_2$ has a molar mass of 74.09 $\frac{g}{mol}$ and a density of 2200 $\frac{g}{m^3}$. Molar mass and density of CaO are 56.08 $\frac{g}{mol}$ and 3340 $\frac{g}{m^3}$, see Table 2.2.

Schaube et al. [2012] proofed cycling stability for 100 cycles of hydration and dehydration for a sample of ca. 30 mg. However, they detected changes in the surface structure of the solid particles. The material before cycling had a fibrous, cotton-like surface structure. After 10 cycles, the surface is reduced and features a granular-like structure. In [Schaube et al., 2013a], they detected, that the surface area decreases from 16 $\frac{m^2}{g}$ to 9.9 $\frac{m^2}{g}$ for $Ca(OH)_2$ after 25 reaction cycles. Whereas Schaube et al. [2012] state, that this change in surface does not affect the reaction because the times until complete conversion didn't differ with the small amount of substance, Schaube et al. [2013a] detect an increased duration for complete conversion. This reduction is associated to

the last 20 % of reaction until complete conversion. Yan et al. [2019] report a structural change of CaO and $Ca(OH)_2$ dependent on the reaction temperatures. Figure 2.3 shows micrographs for the material before reaction and after 10 reaction cycles of dehydration and hydration.

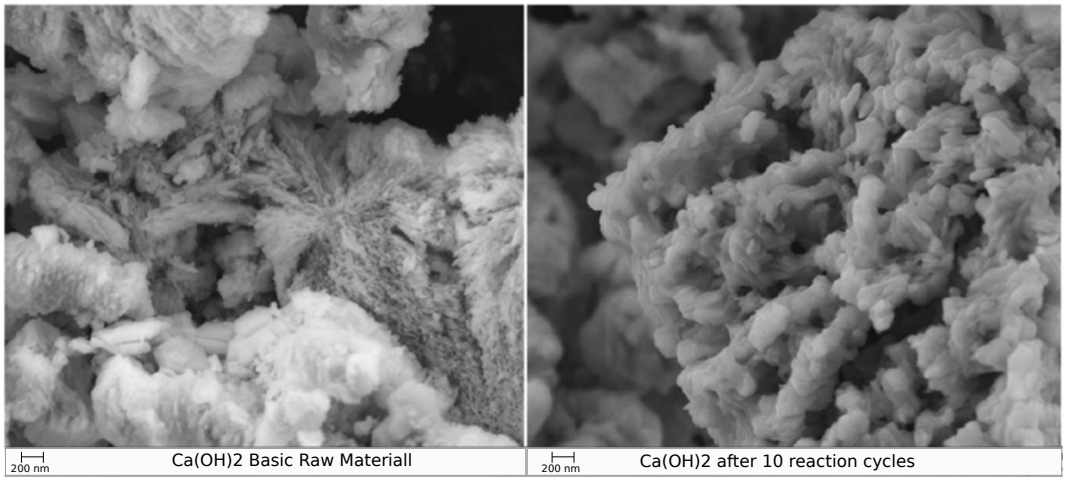

Figure 2.3: SEM micrographs for $Ca(OH)_2$ at initial state and after cycling from [Schaube et al., 2012] [2]

The swelling and shrinking due to the volume change of 50 % during the reaction affects the gas flow behavior in the fixed-bed reactor. Funayama et al. [2019] investigated the use of pellets of around 2mm diameter. They observed, that the pellets crumble to powder due to the stresses while shrinking and swelling. Criado et al. [2014] observed the same for particles of around 1mm size. Kerskes et al. [2011], Schaube et al. [2013a] and Roßkopf et al. [2014] detected agglomerates and preferential flow paths in a powder bulk of a lab scale reactor. Roßkopf et al. [2014] state that after only 4 reaction cycles, the bed properties are not homogeneous anymore. The agglomerates grow and compact with every reaction cycle [Roßkopf et al., 2014]. Figures 2.4 and 2.5 show agglomerates contained in a directly operated fixed-bed reactor and outside the reactor. Roßkopf et al. [2015] report sizes of agglomerates of 2 - 3 cm.

There are strategies to prevent the formation of agglomerates by using additives. Nanoparticles such as "Aerosil" (SiO_2) [Roßkopf et al., 2014] or "Aeroxid" (Al_2O_3) and a combination of both [Gollsch et al., 2020] reduce adhesive forces of the particles

[2] Reprinted from "Thermochimica Acta, 538, F. Schaube et al. A thermodynamic and kinetic study of the de- and rehydration of $Ca(OH)_2$ at high H_2O partial pressures for thermo-chemical heat storage, 9–20, 2012", with permission from Elsevier.

and thus the formation of agglomerates. Another approach is to form stable pellets with composite materials such as $CaCO_3$ with CaO [Alvarez Criado et al., 2015]. In this work however, we aim to model the pure material behavior.

Figure 2.4: View on the reactor for direct charging after 4 reaction cycles shows agglomerates of $Ca(OH)_2$ and preferential flow paths reprinted from [Roßkopf et al., 2014] [3]

Figure 2.5: Single $Ca(OH)_2$ agglomerate from [Roßkopf et al., 2014] [4]

2.5.2 Description of the Chemical Reaction

Different studies investigated the reaction system $CaO/Ca(OH)_2$ with different approaches at different conditions for sample material, pressure and related to this, temperatures. They differ however, in part considerably, in their results.

At first, some authors determined experimentally the van't Hoff relation of equilibrium pressure and temperature given by Equation 2.36 in thermogravimetric measurements. Their results are plotted in Figure 2.6 along with the respective ranges for temperature and pressure. The experimental pressure and temperature ranges are given in Tables 2.6 and 2.5. Each point in Figure 2.6 corresponds to one measurement. Most of the measurement points are close to the mainly used reference of Barin [1995], plotted in black. At low pressures, the speed of reaction is reduced and thus the deviation of

[3] Reprinted from "Energy Conversion Management, 86, C. Roßkopf et al. Improving powder bed properties for thermochemical storage by adding nanoparticles, 93 - 98, 2014", with permission from Elsevier.

[4] See previous footnote.

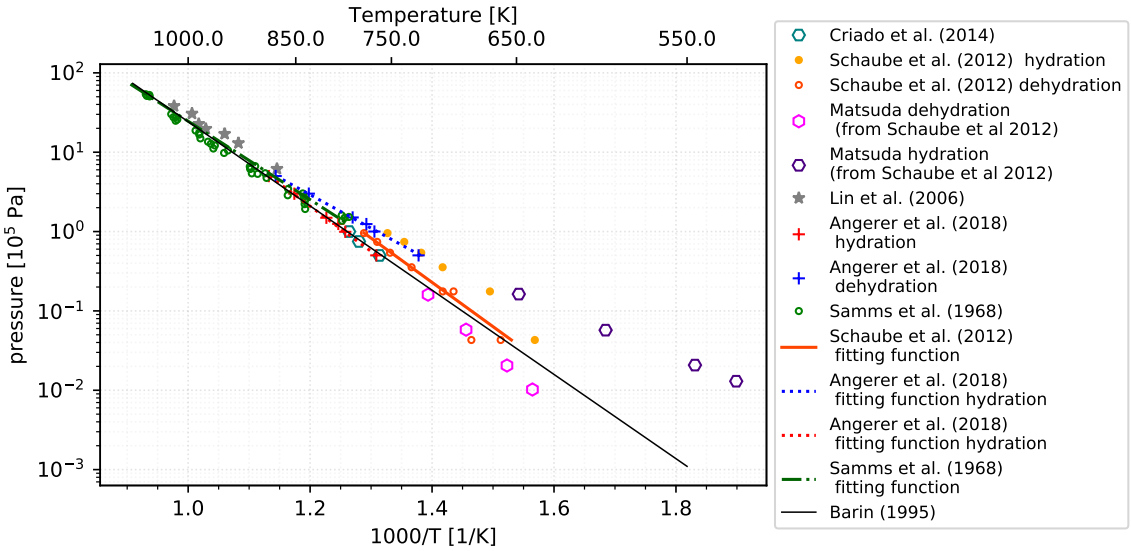

Figure 2.6: Measured values and the fitting functions for the equilibrium pressure and temperature for the reaction system CaO / $Ca(OH)_2$.

the measurement points from the reference increase. The linear fitting functions of the different authors are close to the black line, however only in their respective range of pressure and temperature. Extrapolating those lines would result in larger deviations. The reaction enthalpy ΔH_R is determined by the slopes of the van't Hoff functions. As the different lines in Figure 2.6 vary in slope, the reported reaction enthalpies of the different authors scatter in a range of 94,6 kJ/mol to 124.14 kJ/mol: Schaube et al. [2012] determine a reaction enthalpy of 111.8 kJ/mol by measurement, but use 104.4 kJ/mol as the mean of their own and literature values. Khachani et al. [2014] determine ΔH_R to 124.14 kJ/mol, Samms and Evans [1968] to 94,6 kJ/mol. Lin et al. [2006] use $\Delta H_R = 109$ kJ/mol. Determining the reaction enthalpy from tabulated values of Barin [1995] out of formation enthalpies yields 103.7 kJ/mol at 600 K. The value of reaction enthalpy bears thus uncertainty.

The different studies present furthermore different, even contradicting results concerning the reaction mechanism: [Criado et al., 2014] identified a shrinking core model, "where chemical reaction is the controlling stage" for spherical particles. For [Schaube et al., 2012], a contracting area model for grains of cylindrical shapes fits best to their experimental data. They state however, that they aim at a "mathematical expression rather than a physical interpretation" [Schaube et al., 2012]. [Irabien et al., 1990] applies a pseudo-homogeneous model and [Khachani et al., 2014] the autocatalytic

Sestak-Bergen Model for dehydroxilation. Angerer et al. [2018], Lin et al. [2006] don't name explicitly a known mechanism but fit the data to a mathematical function.

The models and the resulting reaction kinetics are listed in Table 2.5 for hydration and Table 2.6 for dehydration. The different authors consider, despite the different mechanisms, different factors: Only Irabien et al. [1990] does not account for the pressure influence, because all their measurements were done in pure nitrogen atmosphere. Criado et al. [2014], Lin et al. [2006] account for an influence of the particle sizes, a fact, that was addressed by none of the other studies. Angerer et al. [2018] and Schaube et al. [2012] identified hysteresis from the hydration to the dehydration step, but Schaube et al. [2012] attributes this to a measurement error.

None of the reaction kinetics take the particle morphology and its alteration into account. This is however important, as the reaction involves the interaction of different phases (solid and gas) that get in contact at their interfaces. The larger the internal pores of the solid materials, the faster the reaction becomes. Dehydration at high temperatures leads to sintering and the speed of the following hydration is reduced. By subsequent dehydration at reduced temperature, nano-pores get restored [Yan et al., 2019]. The resulting rates are however not quantified in [Yan et al., 2019].

Concerning the various differences in the available studies, Schmidt [2017] assumes, "that the kinetics of the reaction is highly sensitive to the experimental procedure, the pressure and temperature range as well as the nature of the sample material". Thus, no common understanding has been reached yet and the generally applicable reaction mechanism remains unknown in its details.

Therefore, all these factors have to be taken into account carefully when modeling a thermochemical reaction system on the reactor scale. In a modeling study for a directly operated reactor concept, Nagel et al. [2014] compared a simple, theoretical reaction kinetic by [Schmidt, 2011] to the one formulated by [Schaube et al., 2012] and found a reasonable agreement. Risthaus et al. [2020] compares the reaction kinetics of [Schmidt, 2011], [Schaube et al., 2012], [Criado et al., 2014] and [Angerer et al., 2018], and they show different behavior. Thus, for modeling on the reactor scale, the respective reaction kinetics is best chosen according to the pressure and temperature range that was used to determine the respective reaction kinetics.

Applying sophisticated reaction kinetics implies however, that the mechanisms are known. Given the variety of proposed mechanisms, this is however not the case. Therefore, we apply in our modeling the reaction kinetics based on theoretical assumptions of [Schmidt, 2011]. It takes the temperature difference of the actual temperature and equilibrium temperature together with the progression of conversion as driving forces. It reads as follows:

– for hydration (discharge)

$$k_{R,discharge} = k^H \frac{T - T_{eq}}{T_{eq}} x_{\mathrm{H_2O}} (1 - X_H), \tag{2.54}$$

– and dehydration (charge)

$$k_{R,charge} = k^D \frac{T - T_{eq}}{T_{eq}} (1 - X_D), \tag{2.55}$$

with the reaction constants k^D and k^H and the conversion for hydration X_H and dehydration X_D. We use furthermore the simulation cases such, that the water vapor concentration does not limit the reaction rate. For those simulation setups Nagel et al. [2014] state, that these reaction kinetics show good results. Thus, we apply these reaction kinetics, if not indicated differently.

Table 2.5: Summary of reaction kinetics of the reaction system CaO/Ca(OH)$_2$ for hydration. The terms are named according to Equations 2.38 and 2.39.

Author(s)	reaction mechanism	reaction kinetics k_R				experimental conditions for p and/or T)
		A	E	f(x)	f(p,T)	
[Angerer et al., 2018]	-	$390.827e3$	$87.46e3$	$(1-X)$	$\left(max\left\{\frac{^1}{\frac{p_{H_2O}}{p_{eq}}}\right\}-1\right)^{3.43}$	p: 0.5 to 5 bar
[Criado et al., 2014]	shrinking core model	$\frac{2.5e-6}{d_p}$	$59.4e3$	$3(1-X)^{2/3}$	$(\frac{p_{H_2O}-p_{eq}}{p})$	T: 673 and 833 K p: 0 - 100 kPa
[Lin et al., 2006]	excludes gas film diffusion and by-product layer diffusion	$\frac{1}{d_p}\cdot 6.9e-3$	$-8.4e3$	$(1-X)$	$(p_{H_2O}-p_{eq})^2$	p: 0.67 - 2.3 MPa T: 773-983 K
[Schaube et al., 2012] far from equilibrium	-	$1.3945e4$	$8.9486e4$	$3(1-X)$	$\left(\frac{p_{H_2O}}{p_{eq}}\right)^{0.83}$	p: 0 - 96.6 kPa T: 423 - 633 K
[Schaube et al., 2012] close to equilibrium	first order	$1.0004e-34$	$5.3332e4$	$(1-X)$	$\left(\frac{p_{H_2O}}{10^5\text{Pa}}\right)^6$	p: 0 - 96.6 kPa T: 423 - 633 K
[Schmidt, 2011]	-	-0.2	0	$(1-X)$	$\frac{T-T_{eq}}{T_{eq}}X_{H_2O}$	no experiment

Table 2.6: Summary of reaction kinetics of the reaction system $CaO/Ca(OH)_2$ for dehydration. The terms are named according to Equations 2.38 and 2.39. S denotes here the surface are of the solid.

Author(s)	reaction mechanism	reaction kinetics $\frac{\partial X}{\partial t}$				experimental conditions for p and/or T)
		A	E	f(x)	f(p,T)	
[Angerer et al., 2018]	-	$-449.974e3$	91282	X	$\left(min\left\{\frac{1}{\frac{p_{H_2O}}{p_{eq}}}\right\}\right)^{3.43}$	p: 0.5 to 5 bar
[Criado et al., 2014]	First order reaction with respect to the steam volume fraction, shrinking core model	$\frac{5.2 \cdot 10^2}{d_p}$	60.8	$3(1-X)^{2/3}$	$(\frac{p_{H_2O}-p_{eq}}{p})$	T: 673 and 833 K p: 0 - 100 kPa.
[Khachani et al., 2014]	autocatalytic Sestak-Bergen Model for dehydroxilation	$2.07e7$	-132.20	$X^{0.203}(1-X)^{0.380}$		p: 0 Pa
[Irabien et al., 1990]	pseudo-homogeneous model	$1.81e20\left[\frac{cm}{s}\right] \cdot S$	$280.4e3$	$(1-X)$	$1.8583e16\frac{\exp(-\Delta H/RT)}{RT}$	T: 603 - 733.15 K
[Schaube et al., 2012] X $\leq$ 0.2	Contracting area model for grains of cylindrical shapes	$1.9425e12$	$1.8788e5$	$(1-X)$	$\left(1-\frac{p_{H_2O}}{p_{eq}}\right)^3$	p: 0 - 96.6 kPa T: 423 - 633 K
[Schaube et al., 2012] X $>$ 0.2	see above	$8.9588e9$	$1.6262e5$	$2(1-X_D)^{0.5}$	$\left(1-\frac{p_{H_2O}}{p_{eq}}\right)^3$	p: 0 - 96.6 kPa T: 423 - 633 K
[Schmidt, 2011]	-	0.05	-	$(1-X)$	$\frac{T-T_{eq}}{T_{eq}}$	theoretically determined

3 Mathematical Modeling

Numerical modeling often comes along with complex engineered systems, as it is a powerful tool to study complex processes, especially if no simple analytical description is feasible [Nagel et al., 2016].

In this chapter, we present the general mathematical model that is based on the physical and chemical processes introduced in the previous section. We therefore formulate balance equations for mass, momentum and energy in Section 3.1. The combination of all balance equations forms a system of partial differential equations. Due to its complexity, we approximate the solution numerically. We outline the general strategies including discretization in space and time, linearization and solving in Section 3.2. Section 3.3 describes model specializations that involve the coupling of submodels.

3.1 Balance equations

We conserve the quantities mass, momentum and energy within the thermochemical heat storage reactor. A molar formulation of the mass balance equations simplifies the source and sink terms resulting from the chemical reaction due to the stoichiometric coefficients.

3.1.1 Mass Balance Equations of the Gaseous Phase and Components

The gas phase consists of at least one component, the reacting gaseous species. The gas occupies the volume fraction ϕ in the porous bulk of the fixed bed. A change in the gaseous mass of the system arises, if the porosity or the gas density changes, if mass

is added due to a phase flux over the system's boundary or by sources or sinks within the system. Expressed mathematically, this results in the following balance equation:

$$\frac{\partial(\varrho_{m,g}\phi)}{\partial t} - \nabla \cdot (\varrho_{m,g}\mathbf{v}) = q_g^m. \tag{3.1}$$

Here, the first term stands for the phase's storage with the density and porosity, and the second term represents the advection and finally the source and sink term. The advection in a porous medium is determined by Darcy's law for the velocity $\mathbf{v}$ (see Equation 2.48). We use the molar density $\varrho_{m,g}$, to determine the molar flux. Inserting the Darcy velocity results in a combined mass and momentum balance equation:

$$\frac{\partial(\varrho_{m,g}\phi)}{\partial t} - \nabla \cdot \left(\varrho_{m,g}\frac{\mathbf{K}}{\mu_g}(\nabla p)\right) = q_g^m. \tag{3.2}$$

Possibly, an inert component is added to the gas phase depending on the reactor setup. The mass balance equation for each component κ takes additionally a diffusive flux (see Sec. 2.4.1) into account:

$$\frac{\partial(\varrho_{m,g}x^\kappa\phi)}{\partial t} - \nabla \cdot \left[\varrho_{m,g}x^\kappa\frac{\mathbf{K}}{\mu_g}(\nabla p) + \frac{\varrho_g}{M^\kappa}\mathbf{D}_{pm}\nabla X^\kappa\right] = q_g^{m,\kappa}. \tag{3.3}$$

In the above equation (Equation 3.3), we divided the diffusive flux determined by Equation 2.41 with the component's molar mass M^κ for the molar formulation of the mass balance equation. The source term $q_g^{m,\kappa}$ results from the chemical reaction and is quantified in Section 3.1.4. The source/sink term of the inert component is thus always zero.

The permeability $\mathbf{K}$ is potentially a function of the porosity according to Equations 2.13 or 2.14. And, if the Knudsen number is in the respective range, the permeability is adapted as described in Section A.1.

3.1.2 Mass Balance Equations for the Solid Phases

As per the fixed-bed concepts, no solid is transported. Accordingly, only storage and sources of the solid phases are considered. The balance equations of the solid phases

are formulated in terms of their volume fractions θ_λ of the two solid species λ,

$$\frac{\partial(\varrho_{m,\lambda}\theta_\lambda)}{\partial t} = q_\lambda^m. \tag{3.4}$$

Just like in the previous section, the chemical reaction is included via the source terms q_λ, see Section 3.1.4. The solid volume fractions of educt and product θ_{solid1} and θ_{solid2} are possibly different for the same molar amount of the species. Balancing each solid phase separately allows tracking the volume change of the solid matrix (or change in porosity, respectively) during the chemical reaction. Its influence will be discussed in Section 4.3.

3.1.3 Energy Balance Equations

The structure of the energy balance equations is the same as in the mass balance equations: A change in the stored energy occurs due to advective or conductive fluxes or source/sink terms. We balance the energy with contributions of internal, kinetic and potential energy for the gas phase and one averaged solid phase. The contributions of the two solid phases are averaged according to their mass fractions. A detailed derivation including the simplifying assumptions is given in Appendix A.2.

If the gas and the solid phase have different temperatures, we need to balance their energy contents separately. The energy balance of the gas phase results in:

$$\frac{\partial}{\partial t}(\phi\rho_g u_g) + \nabla\cdot[\rho_g \mathbf{v}_g h_g - \phi\lambda_g \nabla T_g] = \underbrace{f(a_{ws}, T_s, T_g, \mathrm{Nu})}_{\dot{e}_{gs}} + q_g^e, \tag{3.5}$$

with the heat exchange between solid and gas phase $\dot{e}_{gs}$. Energy is stored as specific internal energy u_g of the gas phase. The specific enthalpy h_g of the phase is transported and heat is conducted due to a temperature gradient in T_g. Again, the velocity is determined by Darcy's Law 2.48.

The solid is considered incompressible. Thus, the stored energy is expressed with the heat capacity and temperature of the solid. Again, no solid is transported and so the

only energy transport mechanism is heat conduction.

$$\rho_s c_{ps} \frac{\partial (1-\phi) T_s}{\partial t} - \nabla \cdot (1-\phi) \left[\lambda_s \nabla T_s\right] = \underbrace{f(a_{ws}, T_s, T_g, \mathrm{Nu})}_{\dot{e}_{sg}} + q_s^e \tag{3.6}$$

Energy is transferred between the two phases due to a temperature difference, depicted in the terms $\dot{e}_{gs} = \dot{e}_{sg}$. This heat transfer is determined by Equation 2.45. For small particles (as it is the case for the solid material considered in this work) a temperature difference between solid particles and the gas phase evens out rapidly. We therefore assume a local thermal equilibrium. Consequently, one temperature is sufficient for the present phases in the porous medium. This assumption will be verified in Section 4.2. Assuming local thermal equilibrium, the Equations 3.5 and 3.6 are added to the following overall energy balance equation:

$$\frac{\partial}{\partial t} \left(\phi \rho_g u_g\right) + \rho_s c_{ps} \frac{\partial T (1-\phi)}{\partial t} + \nabla \cdot \left[\rho_g \mathbf{v} h_g\right] - \nabla \cdot \left(\lambda_{eff} \nabla T\right) = q^e. \tag{3.7}$$

The storage of each phase is weighted by their volume fractions. For the description of the heat conductivity of the porous medium , see Equation 2.44.

3.1.4 Source Terms

The source terms of the balance equations (q_g^m, $q_g^{m,\kappa}$, $q_{g/s}^e$) depend on the reaction rate q_R. The reaction takes place in the solid phases of the porous medium only. The reaction rate is therefore multiplied by the total solid volume fraction $(1-\phi)$ to yield the mass related source term. For the molar quantity, we divide it by the molar mass of the gaseous reactive component B, see Equation 1.1. This fact is explained as follows: The mass difference of the solid before and after the reaction corresponds to the mass of the reacted gas. The molar source terms result in:

$$q^{m,i} = \frac{\nu_i}{M^B} q_R (1-\phi), \tag{3.8}$$

with the stoichiometric constant ν_i for each reacting species.

The reaction releases or consumes, respectively, reaction enthalpy according to the

reaction rate in the solid phase.

$$q_s^e = \frac{q_R}{M^B}(1-\phi)\Delta H_R. \tag{3.9}$$

However, a gaseous component leaves or enters the solid phase for the reaction. This volume changing work reduces the released heat [Nield and Bejan, 2013]. Therefore, the energy source term of the gas phase is:

$$q_g^e = -\frac{q_R}{M^B}\phi\frac{p}{\rho_{m,g}}. \tag{3.10}$$

The sum of both energetic source terms adds up to the overall energy source term at local thermal equilibrium,

$$q^e = \frac{q_R}{M^B}\left[(1-\phi)\Delta H_R - \phi(\frac{p}{\rho_{m,g}})\right]. \tag{3.11}$$

3.2 Numerical Framework

Our mathematical model for thermochemical heat storage comprises a minimum of four balance equations. The balance equations are coupled strongly and nonlinearly by the chemical reaction. For example, a change in pressure affects the equilibrium temperature of the chemical reaction and thus the reaction rate. This impacts on the water vapor concentration and subsequently the properties of the gas phase with density and viscosity. The gas properties in turn influence the gas flow behavior. There is no analytic solution to this system of equations. Thus, solving this problem requires numerical methods. Carrayrou et al. [2010] compare different solution strategies for reactive transport problems. We choose a monolithic approach. The procedure compromises a discretization in space and time and a subsequent linearization and solving of the problem.

3.2.1 Software

We use the open-source simulator DuMu$^{\text{x}}$ for this undertaking. DuMu$^{\text{x}}$ builds on top of the Distributed and Unified Numerics Environment (DUNE) [Blatt et al., 2016], [Bas-

tian et al., 2008b], [Bastian et al., 2008a], which provides an environment for solving partial differential equations with grid based methods. DuMu^x stands for DUNE for multi-{phase, component, scale, physics, domain, ...} flow and transport in porous media [Koch et al., 2020]. It provides a modular framework for simulating flow and transport of several phases through porous media. The simulations in this work are based on the so called "non-isothermal - one phase - m-component mineralization model": This means that, additionally to the mass balances of the gaseous components, the masses of the solid phases and the energy are balanced. Most simulations were performed with version 3.2 [Coltman et al., 2020]. The software used for each simulation result is listed in Table A.1.

DuMu^x provides the discretization methods for spatial and temporal discretization and the solution methods. For the simulations in this work, we used two different spatial discretization schemes, the cell centered and the vertex centered (BOX) finite volume schemes. They are described in the following section. The discretized set of equations are linearized with the Newton-Raphson method, see e.g. in [Helmig et al., 1997]. The linearized system of equations is then solved either with the UMFPack solver, a part of the SuitSparse Package [Davis, 2019], or with the ILU0BiCGSTAB-solver [Manguoglu and Mehrmann, 2019].

3.2.2 Discretization Schemes

The balance equations presented in the previous section have the following general form: The quantity w is stored, transported due to a spatial gradient and subject to sources or sinks within the simulation domain Ω.

$$\frac{\partial w}{\partial t} + \nabla \cdot \Lambda \nabla w - q_w = 0. \qquad \text{in } \Omega \tag{3.12}$$

Ω is limited by the boundary $\partial\Omega = \Gamma$. At the domain boundary, either Neumann boundary condition (N) for a given flux of the respective quantity (q_N), or a Dirichlet boundary condition (D) with a fixed potential (w_D) is assigned:

$$\begin{aligned} (-\Lambda \nabla w) \cdot \mathbf{n} &= q_N \qquad \text{on } \Gamma_N \\ w &= w_D \qquad \text{on } \Gamma_D \end{aligned} \tag{3.13}$$

We discretize this equation at first in time and subsequently in space.

Temporal Discretization

We approximate the partial temporal derivative of the storage term by the first order difference quotient:

$$\frac{\partial w}{\partial t} \approx \frac{w^k - w^{k-1}}{\Delta t^k}, \tag{3.14}$$

with the discrete time step Δt^k. The time discretized balance equation results to:

$$\frac{w^k - w^{k-1}}{\Delta t^k} + \nabla \cdot \mathbf{j}_w^k - q_w^k = 0. \tag{3.15}$$

This method is called backward Euler method. It is an implicit time discretization, as it depends on all the fluxes of the current time step k and cannot be deduced solely from values of the previous time step. The advantage of this method is its unconditional stability [Helmig et al., 1997].

Spatial Discretization

Equation 3.12 in integral form reads:

$$\int_\Omega \frac{\partial w}{\partial t} d\Omega + \int_\Gamma \Lambda \nabla w \cdot \mathbf{n} d\Gamma - \int_\Omega q_w d\Omega = 0. \tag{3.16}$$

The Green-Gauss Theorem transferred the volume integral of the second term into a surface integral with the normal vector $\mathbf{n}$.

DuMu^x provides different discretization schemes, see Figure 3.1. The cell-centered two point flux approximation (CC-Tpfa) is a classical finite volume method. It is convenient, as it is straight forward and accurate for regular grids. For non-K-orthogonal grids however, it produces an error, that cannot be remedied by grid refinements [Aavatsmark et al., 2008]. Thus, for irregular grids, as they are convenient e.g. for randomly distributed and inclined fractures in the reactor, we apply the BOX method, which delivers more accurate results for such kinds of grids. In the following we briefly present both schemes.

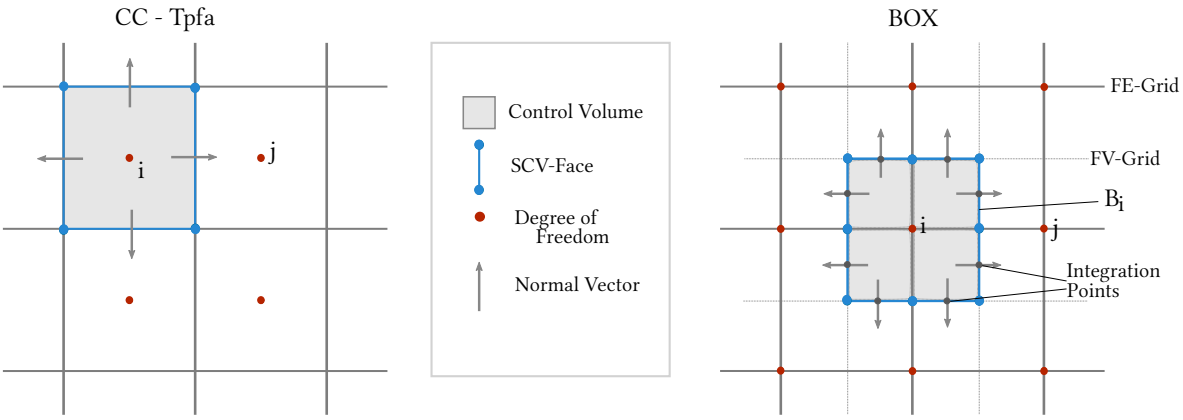

Figure 3.1: Spatial discretization schemes with their Control Volumes and (Sub-) Control Volume Faces (SCV) adapted from [Koch et al., 2020].; **Left** In the Cell-Centered Two point flux approximation (CC-Tpfa) the degree of freedom is in the center of the control volume. **Right** In the BOX method, the degrees of freedom lay on the vertices of the Finite Element (FE) grid. A secondary Finite Volume (FV) grid constructs the box B_i around the node.

Cell-centered Two Point Flux Approximation (CC-Tpfa)

For the CC-Tpfa, we divide the simulation domain Ω into a number ϵ of discrete elements Ω_i. Each element is a control volume. The quantity w is averaged over the control volume and is associated to its center. Neighboring elements share intersections, the control volume faces σ. The control volume is bound by a number n of control volume faces. The conservation of the quantity w holds for every control volume, so that

$$\int_{\Omega_i} \frac{\partial w}{\partial t} d\Omega_i + \int_{\partial\Omega_i} \Lambda \nabla w \cdot \mathbf{n}_{\Omega_i} d\Gamma - \int_{\Omega_i} q_w d\Omega = 0. \tag{3.17}$$

We determine the flux over one face σ of a control volume by the gradient of w of two adjacent elements w_i and w_j and their distance $x_i - x_j$:

$$F_{i,j} = \Lambda |\sigma| \frac{w_i - w_j}{x_i - x_j}. \tag{3.18}$$

We sum up all the fluxes over the n faces of the control volume. Furthermore, we replace the continuous by the integrated storage term $\frac{\partial S_{w,i}}{\partial t} := \int_{\Omega_i} \frac{\partial w}{\partial t} d\Omega_i$ and source/sink term: $Q_{w,i} := \int_{\Omega_i} q_w$. The discretized form of Equation 3.17 in combination with the time

discretization of Equation 3.15 results to:

$$\frac{S_{w,i}^k - S_{w,i}^{k-1}}{\Delta t^k} + \sum_n F_{i,j}^k - Q_{w,i}^k = 0. \tag{3.19}$$

The flux term $F_{i,j}^k$ may have advective and diffusive contributions. For the advective flux contributions, we apply upwinding to avoid oscillations [Helmig et al., 1997].

BOX-Method

We divide the simulation domain at first into a number ϵ of elements to yield the finite element (FE) mesh. We construct a secondary grid, the finite volume (FV) mesh, by connecting the midpoints of the faces and the barycenters of the elements, for the finite volume (FV) mesh, see Figure 3.1 on the right. The secondary mesh divides the elements of the primary grid into subcontrol volumes. The subcontrol volumes surrounding a vertex of the primary grid form a finite volume B_i, the so-called box [Helmig et al., 1997].

We replace the conservation quantiy w by the discrete values $\hat{\mathrm{w}}$ associated to the element vertices and piecewise linear ansatz-functions N_i inbetween to yield the approximate distribution of $\tilde{\mathrm{w}}$:

$$\tilde{\mathrm{w}} = \sum_i^n N_i \hat{\mathrm{w}}_i, \tag{3.20}$$

with m the number of nodes. The gradients of $\tilde{\mathrm{w}}$ are formulated accordingly:

$$\nabla\tilde{\mathrm{w}} = \sum_i^m \nabla N_i \hat{\mathrm{w}}_i. \tag{3.21}$$

The approximate solution produces an error. We introduce weighting functions W_i to get rid of this error. For the BOX-method, the weighting functions are according to [Helmig et al., 1997]:

$$W_i(x) = \begin{cases} 1 & \text{within } B_i, \\ 0 & \text{otherwise,} \end{cases}$$

with x, the location. The approximate solution using the weighting functions results to

$$\int_\Omega W_i \frac{\partial \tilde{\mathrm{w}}}{\partial t} + \int_\Gamma W_i \Lambda \nabla \tilde{\mathrm{w}} \cdot n_\Omega - \int_\Omega W_i \tilde{\mathrm{q}}_w = 0, \tag{3.22}$$

for the overall simulation domain, and for the box B_i to:

$$\int_{B_i} \frac{\partial \tilde{\mathrm{w}}}{\partial t} + \int_{\partial B_i} \Lambda \nabla \tilde{\mathrm{w}} \cdot n_\Omega - \int_{B_i} \tilde{\mathrm{q}}_w = 0. \tag{3.23}$$

We apply mass lumping in order to assure local mass conservation. This means that the quantity $\tilde{\mathrm{w}}$ is located only at the respective node. The amount of $\tilde{\mathrm{w}}$ at the neighboring nodes has no contribution to the amount in box B_i. With this assumption, the first term of Equation 3.23 is replaced by

$$\int_{B_i} \frac{\partial \tilde{\mathrm{w}}}{\partial t} = |B_i| \frac{\partial \tilde{\mathrm{w}}}{\partial t}, \tag{3.24}$$

with the volume of the box $|B_i|$. The third term (source term) is reduced accordingly:

$$\int_{B_i} \tilde{\mathrm{q}}_w = |B_i| \tilde{\mathrm{q}}_w = Q_i. \tag{3.25}$$

The integral in the flux term is replaced by the sum of fluxes over the sub-control-volume faces (SCV-face) evaluated at the integration points of the box with the respective lengths σ and normal vectors $\mathbf{n}_{\sigma,i}$ of the faces. The flux over one SCV-face σ_i of B_i reads:

$$F_i^{\sigma_i} = -\sigma_i \mathbf{n}_{\sigma i}^T \Lambda \nabla N_i \hat{\mathrm{w}}_i \tag{3.26}$$

Thereby, the fully discretized equation yields:

$$|B_i| \frac{\tilde{\mathrm{w}}^k - \tilde{\mathrm{w}}^{k-1}}{\Delta t^k} + \sum_i^{n_\sigma} F_i^{\sigma_i} - Q_i = 0, \tag{3.27}$$

for the box B_i with its number of SCV-faces n_σ. Same as for the CC-Tpfa-method, we apply upwinding for the advective fluxes.

3.3 Model Enhancements by Domain Coupling

For some of the considered simulation cases, different physical processes prevail at different locations. In order to represent them accurately and efficiently in the sense of computational time, we allocate them into separate domains and couple the subdomains with coupling fluxes. DuMu^{x} provides the framework in the module "Multi-Domain" [Koch et al., 2020]. A so-called "coupling-manager" associates the geometrically neighboring grid-cells of two coupled subdomains and evaluates the coupling fluxes between the two domains at the specific location. For the applications we present in this work, the coupling-managers require conforming grids.

We apply the domain coupling in two simulation setups: Firstly, to include a discrete fracture network in the porous bulk of a directly operated reactor and secondly, to couple the heat transfer channel to the porous reaction bed of an indirectly operated reactor. Both setups involve different strategies, which are presented below.

3.3.1 Discrete Fractures in the Porous Bulk

Due to the shrinking and swelling of the $CaO/Ca(OH)_2$ bulk during charge and discharge, preferential flow paths develop in fixed-bed reactors after several cycles of charge and discharge, as described in Section 2.5.1. For simplicity, we term these fracture-like channels "fractures" from now on. Modeling the fracture formation goes beyond our scope. Instead, we model the reaction behavior of a reaction bulk, where fractures have already evolved. Berre et al. [2019] give an overview of possibilities to model fractures in a porous bulk, notably single-continuum models, multi-continuum models and discrete-fracture models. Among those we choose the latter, as it gives the possibility to examine specific fracture patterns.

We treat the fractures as planes with different porous medium properties compared to the rest of the porous bulk. A gas flux with mass, momentum and energy transport is exchanged between fracture and bulk domain. The fractures are randomly distributed and vary in size (including length, width and fracture aperture) and inclination. We represent them by two-dimensional structures within the 3-dimensional bulk domain. Figure 3.2 on the left shows a sketch of a fracture. The two-dimensional fractures split the 3-dimensional bulk domain into discontinuous subdomains, Ω_{b1} and Ω_{b2}, with

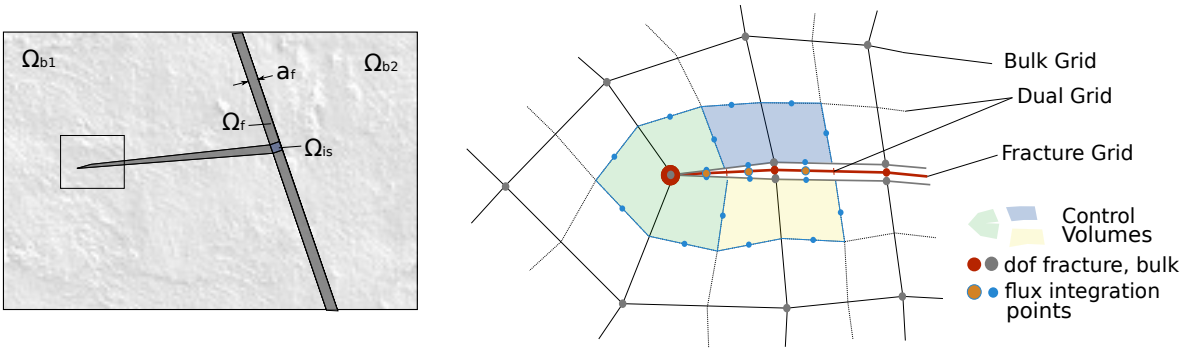

Figure 3.2: **Left**: A fracture separates the bulk into two domains Ω_{b1} and Ω_{b1}. Fractures may intersect and form an additional intersection domain Ω_{is}. The fracture Ω_f is associated with its average fracture aperture a_f. **Right**: The EBOX-DFM discretization scheme is modified after [Gläser et al., 2020b]. It shows the discretized area around the fracture tip. The dofs of fracture and bulk actually coincide, but are stretched here for a better visibility.

internal boundaries. It is furthermore possible that fractures intersect or end within the bulk domain.

From now on, we refer to the bulk as the 3-dimensional (3-D) domain and fractures for the 2-dimensional domain. We assume that the properties of the fractures are constant over their aperture a_f and introduce cross-section averaged quantities, here exemplarily for the pressure:

$$p_f = \frac{1}{a_f} \int_{a_f} p \, da_f. \tag{3.28}$$

In the fracture domain, we balance the same quantities as in the 3-D domain, i.e. momentum and mass for the gaseous components, mass of the solid components and the energy. We assume a small residual content of solid in the fractures and thus, that all fractures feature a higher permeability than the bulk. The cross-section averaged balance equation for gas flux in the fractures reads as follows in a stationary form:

$$\nabla_f \cdot (a_f \rho_{m,g} \mathbf{v}_f) = a_f q_f + |\mathbf{q}_b \cdot \mathbf{n}|_f. \tag{3.29}$$

In that, we consider fluxes between the fracture and the bulk by the exchange term $|\mathbf{q}_b \cdot \mathbf{n}|_f$. Fluxes occur between all the adjacent subdomains. Furthermore, a fracture might end in one bulk subdomain, if it does not strech out over the full length of the bulk subdomain (see Figure 3.2 Left: The domain Ω_{b1} neighbors the horizontal fracture at top and bottom side.). Therefore, we sum over the number of neighboring

bulk subdomains N and the sides connecting bulk and fracture n.

$$|\mathbf{q}_b \cdot \mathbf{n}|_f = \sum_N \sum_n \mathbf{q}_b \cdot \mathbf{n}. \tag{3.30}$$

For the highly conductive fractures, the pressure across the boundary between bulk and fracture is constant:

$$p_b = p_f. \tag{3.31}$$

This corresponds to an internal Dirichlet boundary condition.

We choose the BOX discretization method for the coupled fracture-bulk model. Randomly distributed fracture patterns are disretized more easily with non-regular grids. Due to the flux calculations with the FE-ansatz-functions, the BOX-method performs better with non-regular grids compared to the CC-Tpfa. The enhanced BOX-method for discrete fractures (EBOX-DFM) of [Gläser et al., 2020b] provides the framework for discretizing the fractures and the domain coupling. For each of the coupled submodels, bulk and fracture, linear basis functions N_i according to the respective dimensionality i approximate the real solution within the grid cells. According to [Gläser et al., 2020b], a direct coupling of the two domains with the internal Dirichlet condition of Equation 3.31 does not guarantee mass conservation. Therefore, the condition is included weakly as follows: For calculating the fluxes between bulk and fracture, we substitute the pressure values of the bulk domains located on the same geometric position as the degrees of freedom of the fracture, by the values associated to the fracture degree of freedom:

$$|\mathbf{q}_b \cdot \mathbf{n}|_{b-f} = -\sigma \mathbf{n}_b \mathbf{K}_b \left[\sum_{\substack{n_\sigma \\ x \notin \Omega_f}} p_b \nabla N_b + \sum_{\substack{n_\sigma \\ x \in \Omega_f}} p_f \nabla N_b \right], \tag{3.32}$$

with the face of the subcontrol volume σ and the box number of subcontrolvolume faces n_σ. The fluxes determined by Equation 3.32 are included into the fracture model as additional source terms, and in the bulk domain as internal boundary conditions.

3.3.2 Coupling between Porous Bulk and Heat Transfer Channel

The indirectly operated reactor concept is composed of two functional units, see Figure 3.3: First, the porous reaction bed, where water vapor surrounds the solid particles;

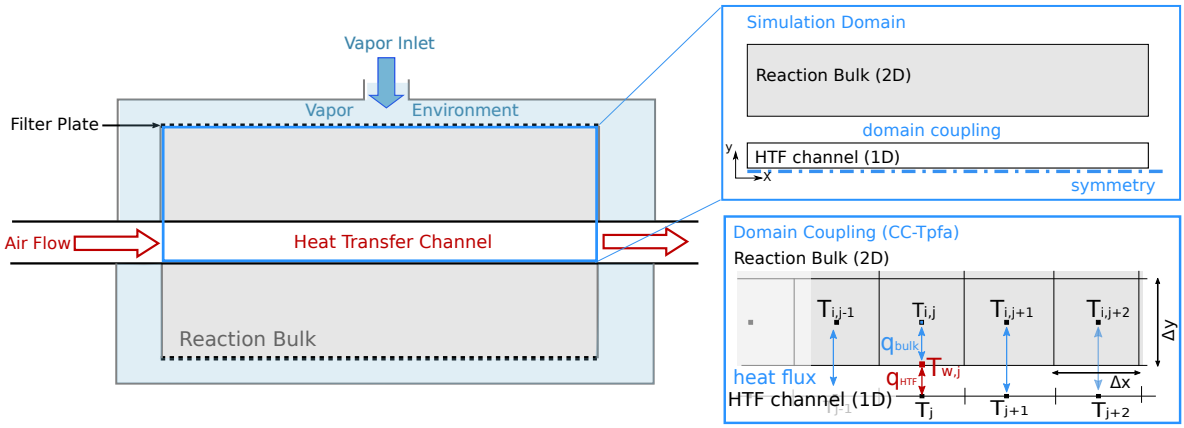

Figure 3.3: Reactor setup; **Left**: Sketch of the experimental setup modified after Schmidt et al. [2017]. The solid bulk is kept between filter plates. Water is provided at constant pressure in the surrounding casing. Air flows through the HTF channel to provide / remove heat. **Top right**: The simulation setup consists of two separate domains: the reactive bulk and the HTF channel. The two domains are coupled by a conductive heat flux. Due to symmetry, the bulk model domain reduces to half of the bulk volume. **Bottom right**: Domain coupling; A heat flux is calculated between the cell centers of the two-dimensional reaction bulk and the 1-dimensional HTF channel.

second, the heat transfer channel (HTF), where a free gas flow transports the heat. Both domains are coupled by a conductive heat flux.

For modeling, we focus on the processes in the porous bulk. Hence, we reduce the dimension of the HTF-domain to $(d-1)$, with d being the dimension of the porous bulk model. This is based on the following simplifying assumptions: The flow profile between the two parallel plates is laminar and compressibility effects are negligible. Those assumptions are justified with the experimental setup in Section 5.1. We apply the Hagen-Poiseuille-law to formulate the fluid velocity between the two plates to

$$\mathbf{v}_{\mathrm{HTF}} = \frac{l^2}{12}\frac{\mu_g}{\varrho_g}\mathrm{grad}\, p, \tag{3.33}$$

with l the channel thickness. The combined mass and momentum balance equation corresponds to Equation 3.2 with 100 % porosity and without sources/sinks. The energy balance equation of the HTF channel-domain corresponds to Equation A.11. The energy source term q^e_{HTF} results from the energy-coupling between the bulk and the HTF domains. The source term is multiplied by 2 in order to incorporate the

symmetry condition.

$$\frac{\partial}{\partial t}\left(\varrho_g u_g\right) + \nabla \cdot \left(\varrho_g \mathbf{v}_{\mathrm{HTF}} h_g\right) - \nabla \cdot \left(\lambda_g \nabla T\right) = 2 \cdot q^e_{\mathrm{HTF}}. \tag{3.34}$$

We discretize the two subdomains with the CC-Tpfa method, see Figure 3.3 on the bottom right. We assume that there is no temperature jump between the two subdomains, i.e. the influence of the metal plate between the bulk domain and the HTF channel is neglected. At the interface between the two domains, the heat fluxes sum up to zero:

$$q^e_{\mathrm{HTF}} = q^e_{bulk} = q^e. \tag{3.35}$$

q^e_{bulk} is thereby the boundary condition of the bulk domain adjacent to the heat transfer channel. q^e_{HTF} is handled as source term in the energy balance equation of the HTF channel-domain.

The heat flux in the porous bulk is purely conductive:

$$q^e_{bulk} = \lambda_{eff} \frac{T_W - T_{bulk,y=\Delta y/2}}{\Delta y/2}, \tag{3.36}$$

with the wall temperature T_W at the interface, the temperature in the bulk grid cell closest to the HTF channel, T_{bulk}, and the size of the bulk grid cell in perpendicular direction (y).

In the free flow, the heat transfer from the bounding wall to the heat transfer flux determines the heat flux:

$$q^e_{\mathrm{HTF}} = \alpha_{\mathrm{HTF}}(T_{\mathrm{HTF}} - T_W), \tag{3.37}$$

with T_{HTF} the temperature in the HTF channel. The heat transfer coefficient α_{HTF} is crucial for determining the heat flux correctly. It will be addressed further in Chapter 5. The two Equations, 3.36 and 3.37, admit of eliminating the unknown wall temperature T_W. The coupling heat flux is then only a function of the temperatures T_{HTF} and T_{bulk}.

4 Simulating the Directly Operated Reactor Containing CaO/Ca(OH)$_2$

The directly operated reactor concept consists of a well insulated reaction chamber, filled with the reactive solid. A mixture of reaction fluid (H_2O) and heat transfer fluid (N_2) is directed through the reactive bulk. We base our numerical simulations on the experimental setup of [Schaube et al., 2013a] (see Figure 1.3). Figure 4.1a shows a sketch of the simulation domain: A cylinder of 5.5 cm diameter and 8 cm length. The cylinder is initially filled with CaO particles for the discharge reaction or with $Ca(OH)_2$ for the charge reaction. The reaction gas is injected from the bottom and leaves the reactor at the top with changed composition and energy content. The gas composition and its temperature drive the chemical reaction.

Several models for fixed-bed thermochemical reactors presented in literature used the same experimental setup for their simulations. Schaube et al. [2013b] present a 2-dimensional model. In order to validate the model with their experimental data, they adapt the previously determined reaction rates of [Schaube et al., 2012]. Nagel et al. [2013] base their model on the same setup but don't validate it against the experimental data. They assume an ideally insulated reactor with no heat losses over the reactor surface. With only gas injection at the top and outflux at the bottom bottom, they reduce the problem to one dimension. Shao et al. [2013] test the influence of different solid particle sizes with the model of [Nagel et al., 2013] and the reaction kinetics of [Schmidt, 2011]. In [Nagel et al., 2014], the authors compare the reaction kinetics of [Schaube et al., 2012] and [Schmidt, 2011] with the same model and simulation setup. All those models assume a constant solid volume. They therefore modify the density of CaO such, that given a constant solid volume, the mass difference between the same amounts of $Ca(OH)_2$ and CaO is equivalent to the mass of water for the same amount. The modified CaO density results to $\rho_{\mathrm{CaO,m}} = 1656\ \mathrm{kg/m^3}$ [Shao et al., 2013]. Based

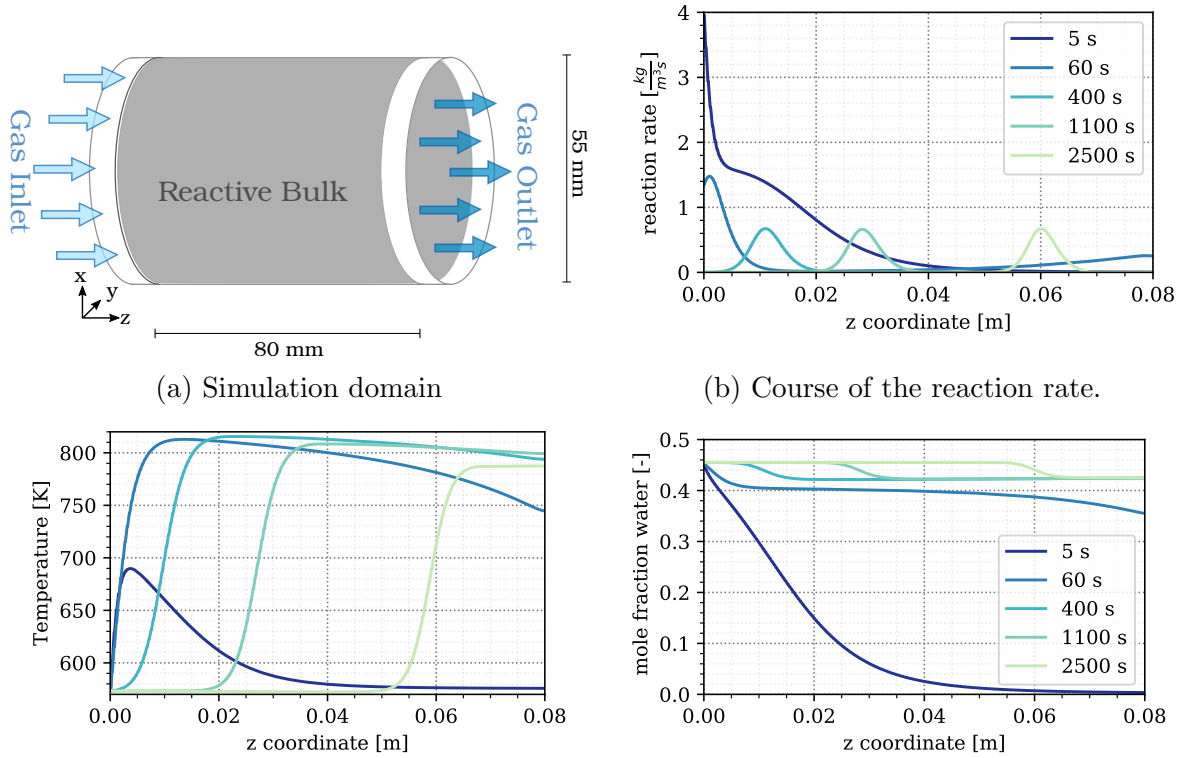

(a) Simulation domain

(b) Course of the reaction rate.

(c) Course of the temperature.

(d) Course of the molar H_2O content.

Figure 4.1: For a homogeneous bulk without heat transfer at the wall, the problem reduces to one dimension. Exemplary simulation results plotted over the reactor length at different times for a discharge reaction with boundary and initial conditions of Case 1 in Section 4.3.

on the assumption of a constant solid volume and porosity, respectively, the model of [Nagel et al., 2013] involves only one balance equation for the solid.

In contrast to the mentioned models, we balance each component separately. Balancing the two solid phases independently allows for representing the volume change of 50 % during the reaction, see Section 2.5.1. With the gaseous components H_2O and N_2, the solid components CaO and $Ca(OH)_2$, and the temperature (assuming local thermal equilibrium), this results in five balance equations, Equations 3.3, 3.4 and 3.7. Same as [Shao et al., 2013], we assume that no heat is lost over the reactor surfaces.

The reaction behavior is complex as the different processes are highly coupled. Figure 4.1b, c and d give an exemplary overview on the interdependence of water vapor pressure, temperature and reaction rate for the discharge reaction. The simulation

setup corresponds to Case 1 in Section 4.3 and is described there in detail. After initiating the reaction, the chemical reaction occurs all over the bulk depending on the availability of water. After 5 seconds, water vapor is depleted in the top region near the outlet. The low water concentration limits the reaction rate. Due to the rate reduction, more water is injected than consumed and the water concentration rises again. After 60 seconds, the gas vapor content is refilled to 0.4 again. Eventually, the temperature approaches the equilibrium temperature at ca. 810 K and limits the reaction rate. Only at the inlet region, where cool gas is injected, the temperature difference induces a considerable reaction rate. CaO is continuously converted to $Ca(OH)_2$ and eventually a reaction front develops and moves from bottom to the top. At the bottom the converted solid accumulates, whereas at the top, the conditions are still at equilibrium. Only at the reaction front, water vapor pressure and temperature allow the reaction to proceed.

For the charge reaction the processes are reciprocal. The injected gas provides the heat necessary for conversion. Water vapor is released in the reaction and increases the vapor pressure and so the equilibrium temperature. At the reaction front the temperature is above the equilibrium temperature and the water vapor concentration is low enough.

The simulations in this chapter address the question, which processes need to be represented in the numerical model to depict the real reactor behavior. We start with a model verification for the homogeneous simulation domain with constant solid volume by comparing different models in a benchmark in Section 4.1. In Section 4.2 we test the assumption of local thermal equilibrium dependent on size of the solid particles. In a next step, we include the solid volume change assuming the process to be reversible and investigate the influence of porosity and induced permeability changes in Section 4.3. Finally, we drop the assumption of a homogeneous bulk and include fracture patterns in the reaction bulk in Section 4.4. Whereas the homogeneous simulation cases are represented in one dimension, the simulations in Section 4.4 will be represented in three dimensions. For the homogeneous setups, we discretize the domain with the CC-Tpfa discretization scheme, but the BOX-scheme for the randomly distributed fractures.

In order to investigate the different processes, we varied the simulation setups including initial and boundary conditions slightly to arrive at realistic and consistent scenarios. For the benchmark scenario in Section 4.1, the porosity is kept constant by a modified CaO density. In the following sections, we applied the tabulated CaO density. For the

same molar amount of CaO, the volume fraction changes with a different density. In all sections we apply the reaction kinetics of [Schmidt, 2011], only for the benchmark scenario, we apply the reaction kinetics of [Schaube et al., 2012]. Therefore, a quantitative comparison between the results of following sections is not possible.

4.1 Model Verification by Benchmarking[1]

The processes in a thermochemical heat storage involving solid and gaseous components are highly coupled and complex. Thus, there is no analytic solution to the mathematical description and due to the lack of appropriate experimental data, it is unclear if all relevant processes are represented. Nagel et al. [2018] conducted a benchmark to gain confidence in the numerical models.

T. Nagel proposed the simulation setup based on the experimental setup of [Schaube et al., 2013a] that we describe in the following section. The benchmark compares the simulation results of three different models: The model results produced in the software OpenGeoSys are provided by T. Nagel. P. Ostermeier generated results with the software ANSYS Fluent and we contributed the results of the presented model in DuMu^x. We give an overview of the different models and their particularities in Section 4.1.2. Subsequently, we present and assess the results. It has to be stated, that the results of DuMu^x differ in this work from those published in [Nagel et al., 2018]. At the time of the publication, the DuMu^x-model excluded the gas volume expansion due to the solid-gas reaction, which led to a considerable error. Including this term yields the results presented in the following.

4.1.1 Setup and Boundary Conditions

The simulation setup for the benchmark corresponds to the setup presented in [Shao et al., 2013]. The ideally insulated cylindrical reactor of 8 cm length and 5.5 cm diameter (Figure 4.1a) is initially filled with a volume fraction of 20 % CaO. A total gas flux of

[1]This section is based on T. Nagel, P. Ostermeier, G. Seitz, H. Class, and R. Helmig. THC-processes. In O. Kolditz, T. Nagel, H. Shao, W. Wang, and S. Bauer, editors, Thermo-Hydro-Mechanical-Chemical Processes in Fractured Porous Media: Modeling and Bench- marking. Springer, 2018

0.5 $\frac{g}{s}$ with a water mass fraction of 0.35 is injected into the reactor at a temperature of 573.15 K to run the discharge reaction. The pressure of 2 bar is kept constant at the reactor outlet, such that gas of different composition and temperature is able to leave the reactor. The constant material properties are summarized in Table 4.1.

Table 4.1: Material properties for the benchmark simulation setup.

Property	Symbol	Value
Porosity	ϕ_{G}	0.8
Density $Ca(OH)_2$	$\varrho_{\mathrm{Ca(OH)_2}}$	$2200\,\mathrm{kg\,m^{-3}}$
Modified density CaO	$\varrho_{\mathrm{CaO,m}}$	$1656\,\mathrm{kg\,m^{-3}}$
Intrinsic permeability	$\mathbf{K}$	$8.53{\cdot}10^{-12}\,\mathrm{m^2}$
Specific heat capacity $Ca(OH)_2$	$c_{\mathrm{p\,Ca(OH)_2}}$	$1530\,\mathrm{J\ kg^{-1}\ K^{-1}}$
Specific heat capacity CaO	$c_{\mathrm{p\,CaO}}$	$934\,\mathrm{J\ kg^{-1}\ K^{-1}}$
Solid heat conductivity	λ_{s}	$0.4\,\mathrm{W\,m^{-1}K^{-1}}$
Diffusion coefficient H_2O/N_2	D_{V}	$9.65{\cdot}10^{-5}\,\mathrm{m^2s^{-1}}$
Reaction enthalpy	ΔH_{R}	$108.3\,\mathrm{kJ\ mol^{-1}}$

The model differs from the model presented in Chapter 3 in the following points: The diffusion coefficient is set to a constant value in this setup. Furthermore, the porosity is set to constant by using the modified CaO density $\rho_{\mathrm{CaO,m}}$ =1656 $\mathrm{kg\,m^{-3}}$, see Table 4.1. Viscosity and heat capacities are calculated by polynomial laws provided in ANSYS Fluent, see in detail in [Nagel et al., 2018]. The reaction kinetics of [Schaube et al., 2012] are used to describe the chemical reaction:

$$k_R = \begin{cases} \text{if } T_{eq} - T \geq 50\mathrm{K}: \\ 1.3945 \cdot 10^4 \cdot \exp(-\frac{8.9486{\cdot}10^4\,\mathrm{J\ mol^{-1}}}{RT}) \cdot (\frac{p_{\mathrm{H_2O}}}{p_{eq}} - 1)^{0.83} \cdot 3(1-X) \cdot (-\ln(1-X))^{0.666}, \\ \text{if } T_{eq} - T < 50\mathrm{K}: \\ 1.0004 \cdot 10^{-34} \exp(-\frac{5.332{\cdot}10^4\mathrm{K}}{T}) \cdot (\frac{p_{\mathrm{H_2O}}}{10^5\mathrm{Pa}})^6 \cdot (1-X), \end{cases} \tag{4.1}$$

with the equilibrium condition

$$T_{eq} = \frac{-12845}{\ln(\frac{p_{eq}}{p_0}) - 16.508}, \tag{4.2}$$

for temperature and pressure.

4.1.2 Specifications of the Software Packages

This section summarizes the specifications of the OpenGeoSys and ANSYS Fluent models. P. Ostermeier provided two different ANSYS Fluent models, the two fluid model (TFM) and the porous zone model (PZM). The DuMu^x model is described in detail in the previous chapters.

- The OpenGeoSys model is based on the theory of porous media [Ehlers, 2002] and is derived in detail in [Nagel et al., 2013]. It uses one mass balance for the overall gas phase and one for the reactive component. Furthermore, it reduces the balance of the solid components to one equation. This is possible due to the assumption of a constant porosity based on the modified CaO density. At constant porosity, the changing overall solid density describes the conversion. Same as the DuMu^x model, OpenGeoSys applies the assumption of local thermal equilibrium. The balance equations are discretized with the finite element method. The system of equations is solved monolithically.

- The ANSYS TFM balances the mass of each involved component, including N_2. A full momentum balance is solved for the gas phase. Friction at the solid gas interface is determined by the Ergun equation [Ergun and Orning, 1949]. Two energy balance equations for solid and gas take temperature differences into account. For the average particle diameter $d_{50} = 8\ \mu$m, only negligible temperature differences were found. The equations are discretized with the finite volume method and solved with the SIMPLE (semi-implicit method for pressure linked equations) algorithm.

- The ANSYS PZM is based on the same equations as the TFM for gas components' mass and momentum balance equations, but only one overall solid mass balance equation. With the assumption of local thermal equilibrium, it furthermore solves only one energy balance equation. Again, the model is discretized with the finite volume method, but solved with the PISO (pressure-implicit with splitting of operators) algorithm.

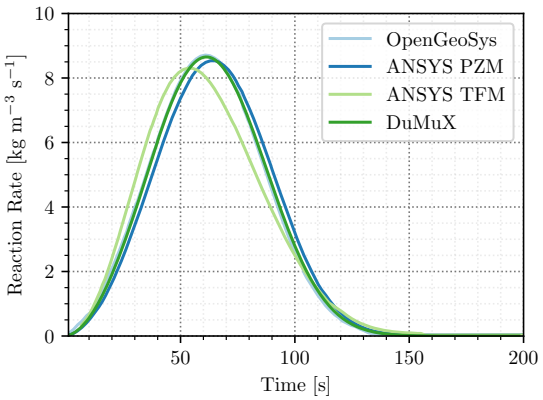

(a) Reaction rate at the reactor inlet over time

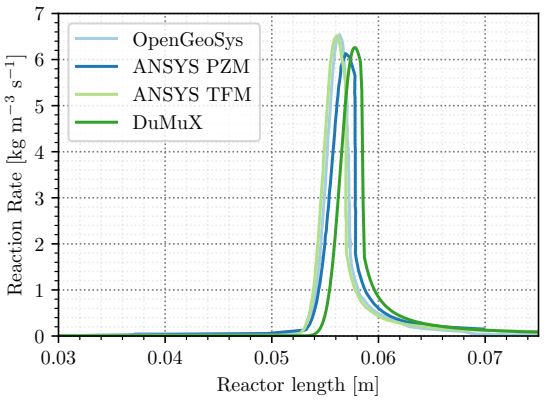

(b) Reaction rate in the reactor at t = 1350 s

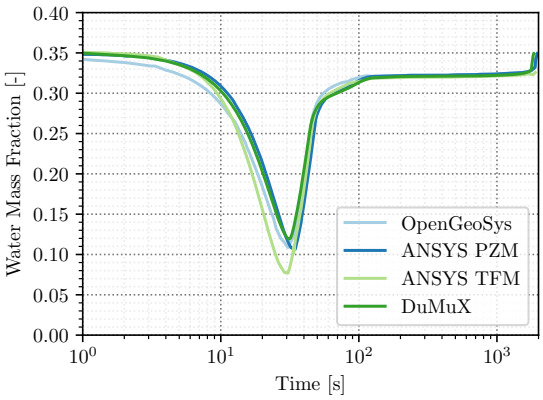

(c) Water concentration at the reactor outlet over time

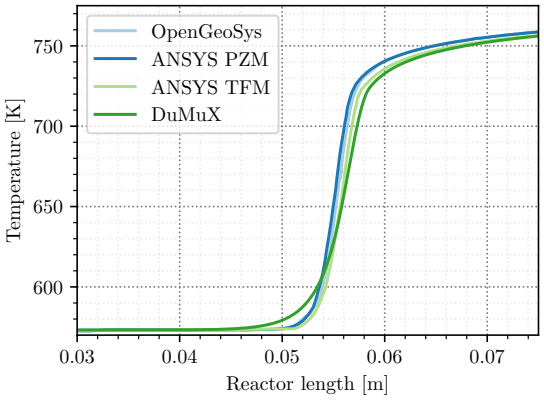

(d) Temperature over reactor lenth at t = 1350 s

Figure 4.2: Benchmark results for water uptake and energy release with the software packages OpenGeoSys, ANSYS Fluent and DuMu^{x}.

4.1.3 Results

We compared different aspects of the simulation results. Internal consistency of each model is shown by comparing the sum of water taken up and the energy released in the reaction for complete conversion to the theoretical values. The results, shown in Table 4.2, show little deviations to the theoretical values.

Furthermore, we compared different aspects of the simulation results. Figure 4.2a shows a plot of the reaction rate at the inlet over time. At the reactor inlet, the reaction rate is not influenced by pressure changes. At a later time (t = 1350 s), the plots over the reactor length give evidence on the reaction front propagation. We compare the shape

Table 4.2: Model comparison regarding total water uptake and energy release.

Model	Water uptake [g]	Energy release [kJ]
Theoretical amount	20.32	122.24
OpenGeoSys	20.30	122.62
ANSYS TFM	20.75	121.72
ANSYS PZM	20.30	124.72
DuMu^x	20.61	123.70

of the reaction rate front (Fig. 4.2b) and the temperature distribution in the reactor (Fig. 4.2d). Other evidence for the correct reaction behavior is gained by looking at the water vapor leaving the reactor at the outlet (Fig. 4.2c). In each plot, all the models show a good agreement. The ANSYS TFM shows the largest deviation from the three other models. It is the only model that considers local thermal non-equilibrium. However, it is unclear, if this is due to the considering of solid-gas temperature difference or due to other differences in the model concept.

4.1.4 Conclusion

The good agreement of the different model results gives confidence in the four different model implementations. This benchmark forms the state-of-the-art of modeling fixed bed thermochemical heat storage.

Some assumptions of the benchmark setups however greatly simplify the real reaction behavior. The difference between the TFM to the others poses the question, whether the heat transfer between solid and gas is limiting the reaction and thus, if it ought to be represented in the model. This question will be answered in the next section. Even more severe is the simplification to neglect the volume change of the solid phase of 50 %. On the one hand, changes in the pore-volumes affect the supply of reactive gas. On the other hand, the solid volume changes are the reason to the formation of agglomerates. Both processes presumably influence the reaction behavior in a directly-operated fixed-bed reactor to a considerable extent. In Sections 4.3 and 4.4, we present approaches to represent them in the numerical model.

4.2 Local Thermal Non-Equilibrium

In a thermochemical reaction of a solid-gas reaction system, the reaction enthalpy is released (hydration) / consumed (dehydration) in form of heat in the solid phase. The gas experiences volume expansion which reduces (hydration)/ increases (dehydration) the heat of the gas phase. Heat is transferred between the phases at the solid gas interface. If the temperature of solid and gas converge fast, the assumption of a local thermal equilibrium is justified. In the previous section however, the one model not assuming local thermal equilibrium showed the largest deviations compared to all other models. We assess in this section, what error is provoked by the simplifying assumption of local thermal equilibrium.

In order to depict the heat flux between solid and gas phase, we need to solve two energy balance equations, Equation 3.5 for the gas phase and Equation 3.6 for the solid phase. The heat transfer between the two phases is determined by the exchange term $f(a_{ws}, T_s, T_f, \mathrm{Nu})$. Therein, the interfacial area a_s is determined according to Equation 2.10, the Nusselt Nu number for the porous medium to Equation 2.46. Thereby, the heat exchange term between solid and gas phase results according to [Nuske et al., 2014] to:

$$f(a_{ws}, T_s, T_f, \mathrm{Nu}) = a_s(T_s - Tg)\frac{\lambda_g \mathrm{Nu}}{L_{ch}} \tag{4.3}$$

The characteristic length is set to the mean grain size, $L_{ch} = d_{50}$.

4.2.1 Simulation Setup

We use the same simulation setup as in the benchmark presented in the previous section. This includes the domain size and resolution, the material properties, initial and boundary conditions. However, we use the reaction kinetics of [Schmidt, 2011] with the reaction constant k_H=0.2. We test 4 different possible grain sizes in the range of typical grain sizes presented in literature: from 5 μm [Schaube et al., 2012] to 1 mm [Criado et al., 2014]. Porosity and permeability are set to the values listed in Table 4.1 regardless of the grain size.

4.2.2 Results and Discussion

Figure 4.3 presents the temperature difference between solid and gas phases ($T_s - T_g$) for the different grain sizes after 1000 seconds of hydration reaction plotted over the reactor length, and Table 4.3 lists the maximum difference at the location z = 0.0425 m. The largest temperature difference occurs at the reaction rate front, where the reaction rate is highest and the most heat is released. The largest grain size displays the largest temperature difference. The larger the grain size, the smaller is the interfacial area between solid and gas, and thus, the smaller is the heat transfer. The temperature difference of 0.03 K for a grain size of 5e-5 m is already below the range of measurement uncertainty of commercial thermocouples (0.4 %T see e.g. [Schmidt et al., 2017]) and thus, negligibly small. For the particle size 5e-6 m, the temperature difference amounts to zero.

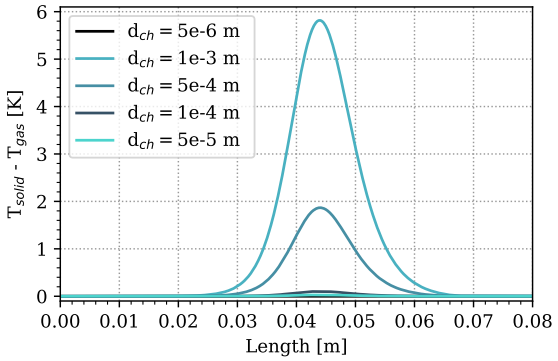

Figure 4.3: Difference between T_{solid} and T_{gas} for different characteristic pore sizes over the reactor length after 1000 seconds hydration.

L_{ch} [m]	max($T_s - T_g$) [K]
1e-3	5.81
5e-4	1.87
1e-4	0.10
5e-5	0.03
5e-6	0.00

Table 4.3: Maximal temperature differences between solid and gas after 1000 seconds hydration at z = 0.0425 m.

4.2.3 Conclusion

The simulation results show, that for small particles ($\leq$ 5e-5 m), the temperature difference between solid and gas is negligible. As there is no time shift in the reaction front, we conclude, that the deviations of the TFM in the benchmark are the result of other differences of the model. Besides the heat transfer coefficient, the interfacial area between gas and solid is determining the heat flux. Shi and Wang [2011] assume spherical particles to determine the surface of the solid. Figure 2.3 shows, that the solid

$Ca(OH)_2$-particles feature an internal porosity, that may contribute further to the solid-gas interface. Thus, assuming spheres is a conservative assumption. Additionally, in our simulation setups in this work we consider even smaller particles of 5e-6 m. This justifies the assumption of local thermal equilibrium. Hence, we reduce the set of primary variables from two temperatures (T_s, T_g) to only one overall temperature (T) for the solid and gas phases. This allows to save computational effort without appreciable loss of accuracy.

The simulation setup in this section is based on theoretical considerations. One would expect the pressure and permeability to depend on the grain sizes, too, but we limited the effect of the particle sizes to the heat transfer. The influence of changing porosity and permeability is addressed in the next section for small grain sizes and thus under the assumption of local thermal equilibrium.

4.3 Influence of Porosity Induced Permeability Alterations [1]

In the previous sections, we neglected the change in solid volume of 50 % during the thermochemical reaction of $CaO/Ca(OH)_2$, as it is presented in Section 2.5.1. Other reaction systems also feature a change in solid volume, such as Strontium bromide and water [Stengler et al., 2017, Michel et al., 2012] or magnesium sulfate and water [Van Essen et al., 2009]. Such a change in morphology potentially alters the texture of the porous medium, the pore sizes and the internal roughness, and consequently the resistance to the gas flow. The chemical reaction in turn depends on the availability of fluid and heat and thus, on the gas flow. In this section, we aim to show the effect of considering changing porosity and permeability on the chemical reaction behavior.

Some numerical models consider the change in solid volume for different reaction systems: Michel et al. [2012], Lu et al. [1996] and Malley-Ernewein and Lorente [2019] interpolate linearly between experimentally determined starting and final permeability based on the conversion.

[1] This section is based on G. Seitz et al.: A numerical modeling study on the influence of porosity changes during thermochemical heat storage. Applied Energy, 2020, 259. Jg., S. 114152.

For the reaction system CaO/Ca(OH)$_2$ however, only the permeability associated to Ca(OH)$_2$ is known. We lack pore-scale information on the morphology alteration of particles and pores, and the permeability associated to the CaO reactor filling. Hence, we assume that the porous bulk alters homogeneously and isotropically. We attribute the solid volume change to a reversible change in porosity such that the overall reactor volume stays constant. Based on the porosity change, we determine alterations in permeability. As the mechanism of the permeability change is unknown for thermochemical heat storage systems, we test two different approaches: The Kozeny-Carman law (Equation 2.13) and the power law (Equation 2.14). The power law allows for choosing the exponent γ to best represent the process. Unpublished experiments[2] show a ratio of initial to converted permeability of 100. With the porosity of 0.8 for Ca(OH)$_2$ and 0.6 for CaO, we choose $\gamma = 16.5$, to map the experimental permeability change.

4.3.1 Simulation Setup

Our model allows for flexibly and independently considering the porosity change and the induced permeability alteration. We simulate and compare four different cases both for charge and discharge reactions:

1. Case of constant porosity and permeability, that reflects the model of Nagel et al. [2013]
2. Case with changing porosity according to the solid contributions of CaO and Ca(OH)$_2$; the permeability is kept constant to show solely the influence of porosity.
3. Case with changing porosity; the permeability changes according to the law of Kozeny-Carman (Equation 2.13).
4. Case with changing porosity and permeability change according to the power law (Equation 2.14).

The ranges for porosity and permeability for each case are listed in Table 4.4. The initial solid volume fractions were adapted compared to Section 4.1 to get realistic reactor conditions. We took the reference porosity of 0.8 for the CaO filling, i.e. a CaO

[2]statement in a personal conversation with Marie Gollsch, scientist at DLR Stuttgart working on reactor setups for the reaction system CaO / Ca(OH)$_2$, on 17 January 2019

volume fraction of 0.2. With the molar masses and mass densities listed in Table 2.2, the same molar amount corresponds to a volume fraction of 0.4 in $Ca(OH)_2$. For the case of constant porosity applying the modified CaO density of Section 4.1, the porosity remains always 0.6. Additional material and reaction properties, that differ from the benchmark simulations in Section 4.1 are listed in Table 4.5.

Table 4.4: Overview of the considered simulation cases.

	Description	Range of ϕ [−]	Range of K [m^{-2}]
Case 1	Modified ρ_{CaO} leads to a constant ϕ and thus K	0.6	5.22e-13
Case 2	Tabulated ρ_{CaO}, changing ϕ but constant K	0.6 - 0.8	5.22e-13
Case 3	Tabulated ρ_{CaO}, changing ϕ and Kozeny-Carman-Law for K change	0.6 - 0.8	5.0e-12 - 5.22e-13
Case 4	Tabulated ρ_{CaO}, changing ϕ and power-law for K change	0.6 - 0.8	5.22e-11 - 5.22e-13

Table 4.5: Material and reaction properties.

Property	Symbol	Value	
Tabulated density CaO	ρ_{CaO}	$3340\,kg\,m^{-3}$	[Haynes, 2010]
Modified density CaO	$\rho_{CaO,m}$	$1656\,kg\,m^{-3}$	[Shao et al., 2013]
Power law exponent	γ	16.5	pers comm. M. Gollsch
Reaction constant hydration	k^H	0.2	[Shao et al., 2013]
Reaction constant dehydration	k^D	0.05	[Shao et al., 2013]

According to the previous section, we apply here the reaction kinetics of [Schmidt, 2011], since our primary focus lies on investigating the influence of changing porosities and related permeability changes. However, we need to enhance the formulation for the reaction rates by the sign factor β, in order to compare the different model concepts of constant and changing porosity. Multiplying the reaction kinetics (k_R) with the density difference between the solids CaO and $Ca(OH)_2$ yields the reaction rate (q_R, see Equation 2.40). The $Ca(OH)_2$ density is the same for both concepts. However, the modified CaO density is smaller and the tabulated CaO density is larger than the $Ca(OH)_2$ density. This results in different signs for determining the reaction rate. The factor β compensates for this. For the case of a constant solid volume fraction (due to the modified CaO density), its value is -1, for the changing solid volume fraction (with the tabulated CaO density), it is set to 1.

– Reaction kinetics of hydration (discharge):

$$k_{R,H} = \beta k^H \frac{T - T_{eq}}{T_{eq}} x_{\mathrm{H_2O}} (1 - X_H) \tag{4.4}$$

– Reaction rate of dehydration (charge):

$$k_{R,D} = \beta k^D \frac{T - T_{eq}}{T_{eq}} (1 - X_D) \tag{4.5}$$

The boundary conditions are listed in Table 4.6. The initial pressure equals the Dirichlet pressure of the outflow boundary, and the initial gas composition in the reactor equals the composition of the injected gas. At the beginning of a simulation, the solid filling consists of one single component, CaO for the discharge run, Ca(OH)$_2$ for the charge run.

Table 4.6: Boundary conditions for the simulations testing the influence of porosity and permeability; the solid components CaO and Ca(OH)$_2$ are not transported and therefore, only initial conditions for their volume fractions are formulated. z = 0 cm is the reactor inlet and z = 8 cm the reactor outlet.

	Location	Primary variable	Value
Discharge	z = 0 cm	p	$q_{N_2} = 2.542$ mol s^{-1}
		$x_{\mathrm{H_2O}}$	$q_{\mathrm{H_2O}} = 2.123$ mol s^{-1}
		T	$T = 573.15$ K
	z = 8 cm	T, $x_{\mathrm{H_2O}}$	Solution-dependent Neumann flux
		p	$p = 2.0$ bar
Charge	z = 0 cm	p	$q_{N_2} = 4.64$ mol s^{-1}
		$x_{\mathrm{H_2O}}$	$x_{\mathrm{H_2O}} = 0.01$ mol s^{-1}
		T	$T = 773.15$ K
	z = 8 cm	T, $x_{\mathrm{H_2O}}$	Solution-dependent Neumann flux
		p	$p = 1.0$ bar

4.3.2 Simulation Results

In order to evaluate the differences of the four simulation cases of Table 4.4, we compare the spatial distribution of different parameters after a certain reaction time: for charge after 4900 s, for discharge after 2600 s. The local conversion (as defined in Equation 2.40) is used as a measure for the reaction progress. Additionally, we plot the water

mole fractions and the temperature at the outlet. A combined parameter is the net power output, that we define by the difference between energy input and output:

$$P_{out} = \dot{m}_{out} h_{out} - \dot{m}_{in} h_{in} \tag{4.6}$$

Figures 4.4o and 4.4p show, that the energy output is negative in the first seconds until the pressure gradient is built up. For the charge reaction, the energy output becomes positive subsequently, because initially hot gas is pushed out of the reactor until the equilibrium temperature is reached. Additionally, the gas outflow already contains a considerable amount of water and thus carries more energy than the injected nitrogen of the same temperature. The initial peak drops as soon as cooler gas leaves the reactor. The heat of the injected gas is consumed in the reaction. Once the reaction is finished and the reactive bulk has a uniform temperature, the net energy output is zero, both for charge and discharge.

Table 4.7: Simulation results for the time and total net energy output for complete conversion for the simulation cases listed in Table 4.4

	Charge		Discharge	
Case	Time [s]	Total energy [kJ]	Time [s]	Total energy [kJ]
Case 1	6937	-118.7	3975	139.7
Case 2	6255	-106.9	3800	127.3
Case 3	5936	-107.0	4060	127.7
Case 4	5903	-107.1	4095	128.6

Figures 4.4a - 4.4t contain the plots of different parameters for all the four cases of the charge reaction (left) and the discharge reaction (right). Table 4.7 provides the reaction times for complete conversion in the different cases as well as the time integral of the power output (defined in Eq. 4.6), expressed in terms of the total energy output for complete charge (negative) and discharge (positive). The total amount of released reaction enthalpy is 245 kJ, which is obtained by multiplying the molar amount of solid reactor fill with the molar reaction enthalpy. It differs considerably from the numbers in Table 4.7. A significant amount of sensible heat is contained in the temperature difference of the reactor before and after conversion. Furthermore, the gaseous component performs volume changing work when entering/leaving the solid phase in the chemical reaction.

At first, we compare the Cases 1 and 2, to examine the influence of the porosity change

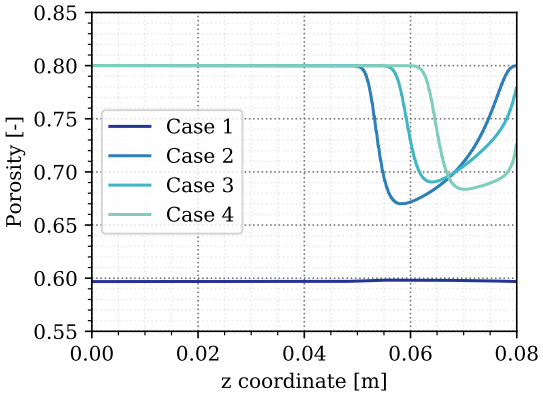

(a) Charge: porosity at 4900 s over the reactor length

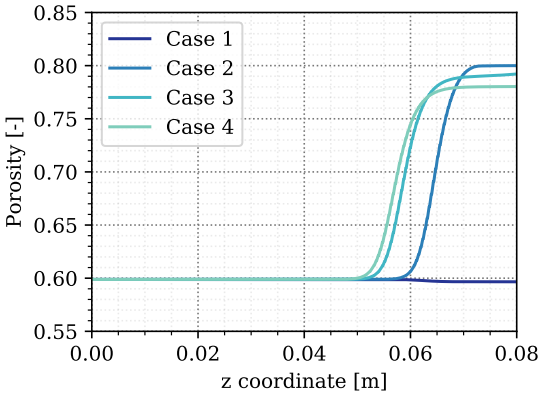

(b) Discharge: porosity at 2600 s over the reactor length

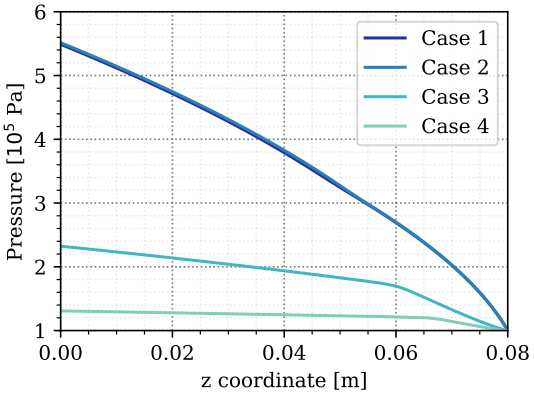

(c) Charge: pressure at 4900 s over the reactor length

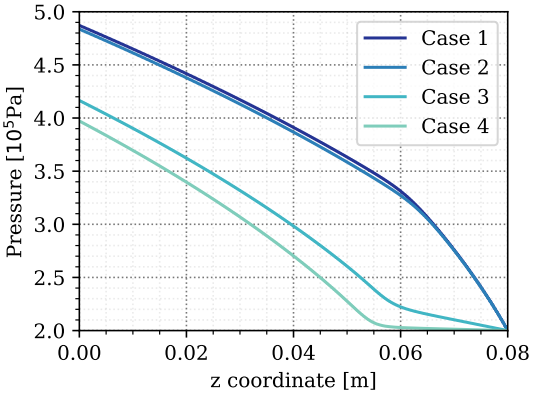

(d) Discharge: pressure at 2600 s over the reactor length

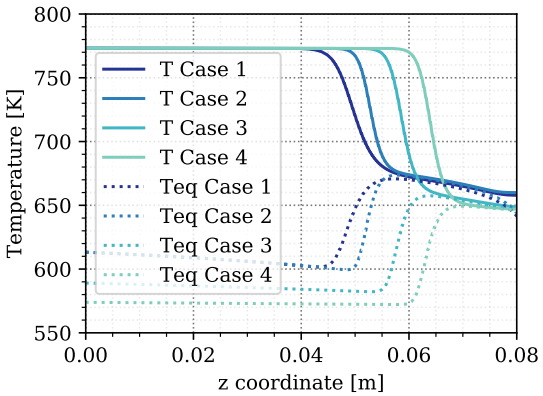

(e) Charge: temperature and equilibrium temperature at 4900 s over the reactor length

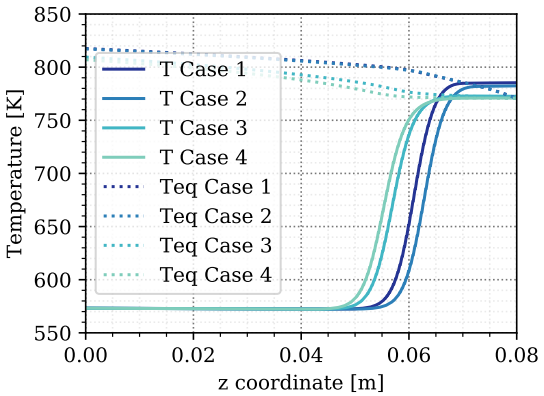

(f) Discharge: temperature and equilibrium temperature at 2600 s over the reactor length

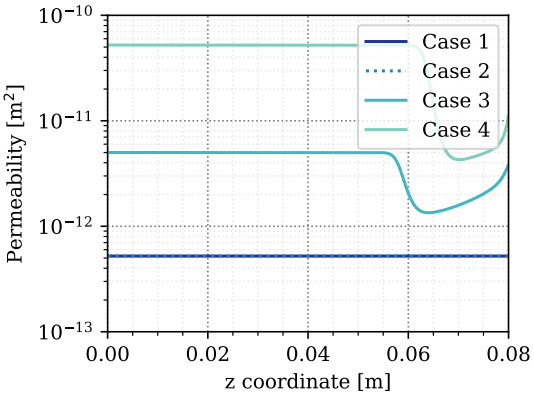

(g) Charge: permeability at 4900 s over the reactor length

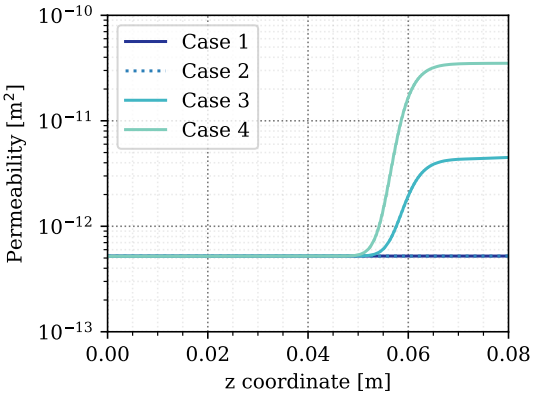

(h) Discharge: permeability at 2600 s over the reactor length

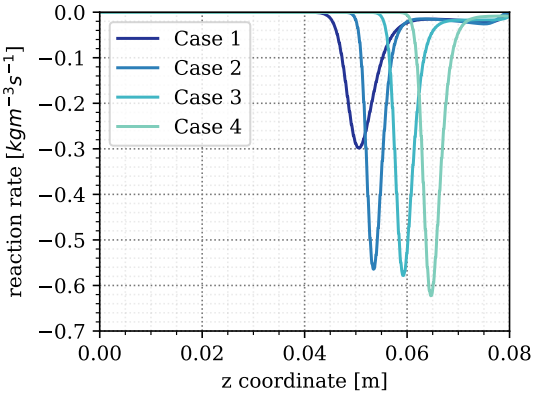

(i) Charge: reaction rate at 4900 s over the reactor length

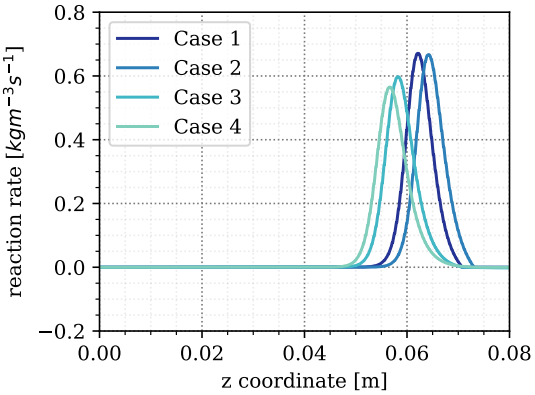

(j) Discharge: reaction rate at 2600 s over the reactor length

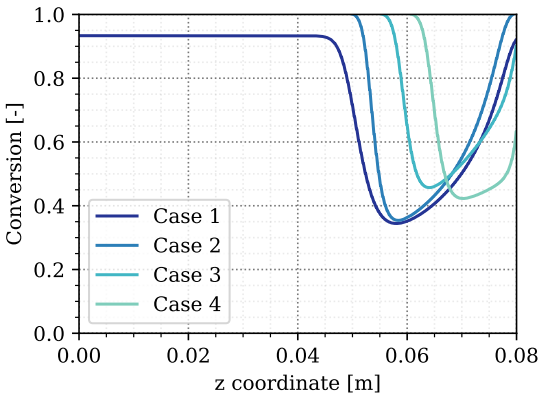

(k) Charge: conversion at 4900 s over the reactor length

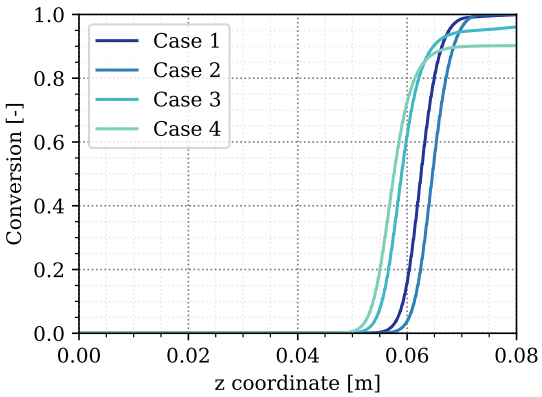

(l) Discharge: conversion at 2600 s over the reactor length

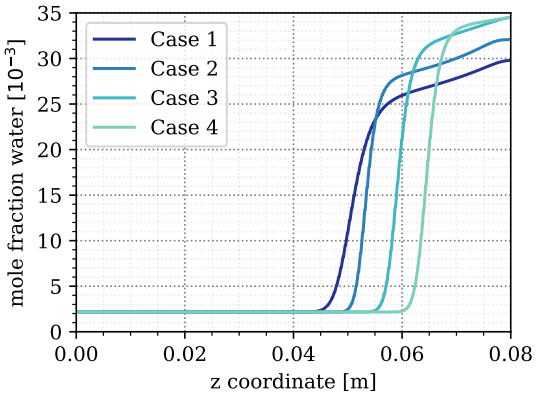

(m) Charge: water mole fraction at 4900 s over the reactor length

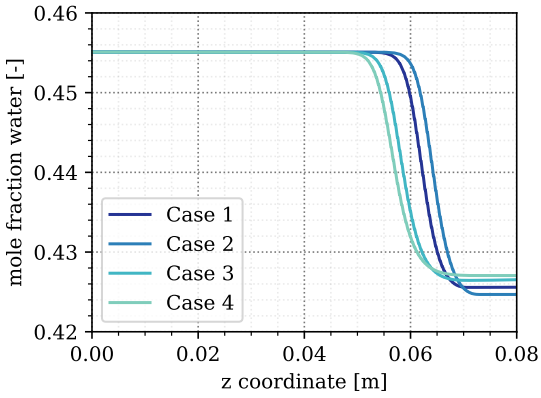

(n) Discharge: water mole fraction at 2600 s over the reactor length

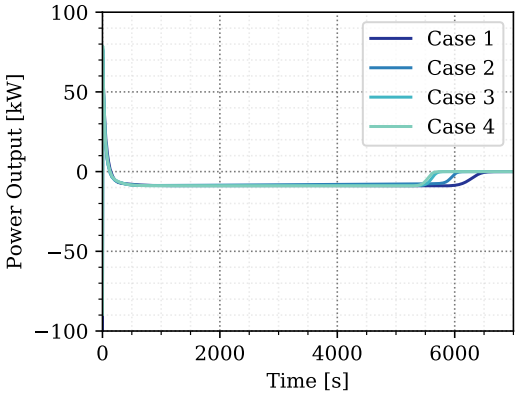

(o) Power output of the charge reaction over time

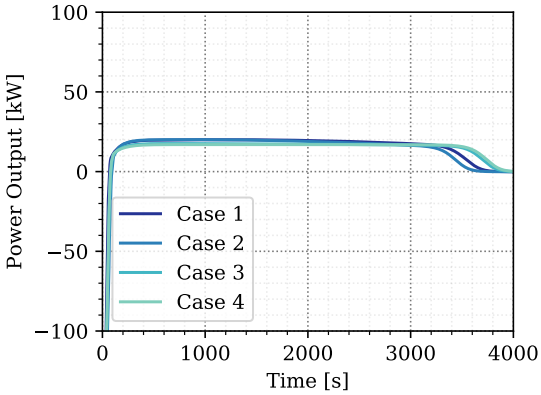

(p) Power output of the discharge reaction over time

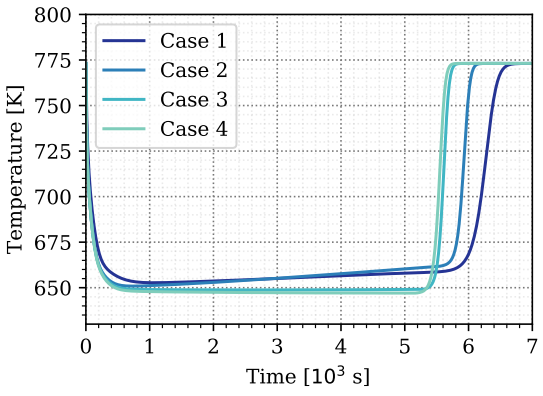

(q) Charge: Temperature at the outlet over time

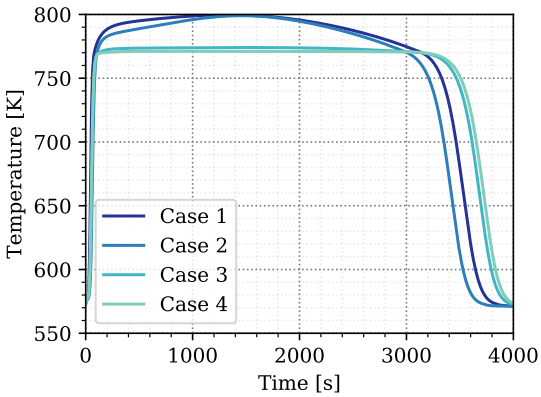

(r) Discharge: Temperature at the outlet over time

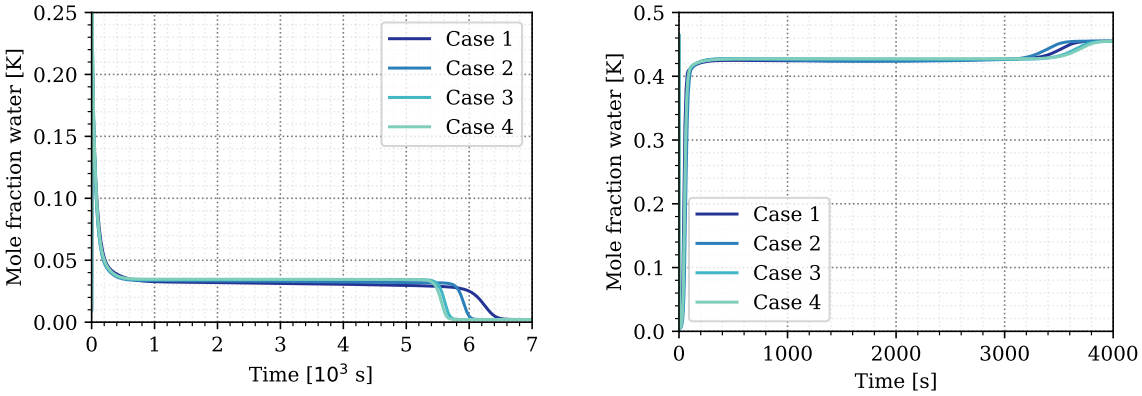

(s) Charge: water vapor content at the outlet over time

(t) Discharge: water vapor content at the outlet over time

Figure 4.4: Comparison of different parameters involved in the chemical conversion process for the four simulation cases each for charge and discharge reactions: Case 1: constant porosity and permeability, Case 2: alternating porosity but constant permeability, Case 3: Kozeny-Carman law for porosity induced permeability changes and Case 4: power law for porosity induced permeability changes.

on the reaction. Subsequently, we analyse the two different porosity-permeability relations.

Influence of the porosity change

With the same permeability, Cases 1 and 2 show roughly the same pressure distributions (Figs. 4.4c, 4.4d) and as a result, same equilibrium temperatures (Figs. 4.4e, 4.4f). Nevertheless, Cases 1 and 2 show different results in charge and discharge. The reaction fronts move faster for Case 2, both for charge and discharge (Figs. 4.4i, 4.4j), which results in a different reaction time. The charge reaction of Case 2 is completed 682 s faster than in Case 1, the discharge reaction 175 s faster (Tab. 4.7). Table 4.7 furthermore shows that the amount of energy for total conversion differs considerably for Case 1 compared to all other cases.

The influence of the porosity change on the reactions is attributed essentially to two overlapping effects:

At first, the different volume fractions affect the heat conduction. The solids have a higher heat conductivity than the gas. Thus, the overall heat conductivity increases for

a decreasing porosity and vice versa. During charge, the porosity increases for Case 2. Thus, in Case 1 more heat is conducted against the direction of the reaction front. A widening of the reaction region of Case 1 during the charge reaction results and thus a smaller peak height, but larger peak width, as shown in Figure 4.4i. Hence, the steepness of the reaction fronts differs. For discharge, the porosity decreases in Case 2. The conductive heat flux against the front's direction is the same for both cases and thus, the effect is less important.

Secondly, a different porosity implies a different storage volume for the gas. The gaseous reactive component performs volume expansion if it enters (charge reaction) or leaves (discharge reaction) the gas phase. For a bigger gas volume as in Case 2, this expansion work is increased. On the molecular scale, the water molecules travel over longer distances. This amount of energy no longer appears in the overall released energy balance in Table 4.7. As less volume-changing work is done in Case 1, more energy is released in form of heat during the discharge reaction. The gas flux however is the same in all simulation cases and thus, the reaction front slows down for Case 1 both for charge and for discharge.

Neglecting the influence of the porosity change overestimates the reaction time for total conversion and the total energy that needs to be provided by or respectively, taken away by the injected gas for the charge and discharge reaction.

Influence of the permeability change

The alternating permeability changes the pressure distribution given the same gas injection in Cases 3 and 4 (Figs. 4.4c, 4.4d). The pressure directly influences the equilibrium temperature. Thus, the reaction front velocity differs for the different cases (Figs. 4.4i, 4.4j).

The increasing porosity during the charge reaction increases the permeability in Cases 3 and 4, and consequently decreases the pressure compared to Cases 1 and 2 (Fig. 4.4c). For discharge, the effect is reversed. However, the differences between the four simulation cases are less prominent, as the final permeability distribution is the same for all cases (Fig. 4.4h). The lower pressures in Cases 3 and 4 lower the equilibrium temperatures (Fig. 4.4e, 4.4f) and consequently the temperatures for conversion. For the charge reaction, a larger difference between temperature and equilibrium temperature

increases the reaction rates for Cases 3 and 4 (Fig. 4.4i) and thus the front velocities and the time until complete conversion, see Table 4.7. For the discharge reaction however, a smaller equilibrium drop reduces the reaction rates for Cases 3 and 4, and retards the reaction. The changed reaction rates furthermore result in increased gas vapor contents for charge (Fig. 4.4m) and lower vapor contents for discharge (Fig. 4.4n).

The permeability difference between the Cases 2 to 4 is roughly one order of magnitude. However, the effect on the reaction behavior is non-linear. The pressure differences between Cases 2 and 3 are larger than between 3 and 4.(Fig. 4.4c, 4.4d). The nonlinear behavior carries on to the reaction front velocities. For charge, the times until full conversion is 319 s (5.1 %) less for Case 3 and 352 s less for Case 4 (5.6 %) compared to Case 2 with constant permeability. For discharge, Case 3 requires 260 s (6.8 %) and Case 4 295 s (7.8 %) more for complete conversion.

4.3.3 Conclusion

Both porosity and permeability alterations have shown a considerable effect on the simulation results for the charge and the discharge reaction. Due to the high dependency of pressure, equilibrium temperature and reaction rate, the results of Cases 1-4 differ strongly in the velocity of the reaction front and thereby in the times until complete conversion. A higher permeability and a corresponding lower pressure reduce the equilibrium temperature. For a constant inlet pressure, the equilibrium drop increases for the charge reaction and hence facilitates it. For the discharge reaction, this effect is reversed: The reduced permeability in the not yet converted region leads to smaller pressures in the reactor, too, and reduces the equilibrium temperatures. This lowers the equilibrium drop and thereby reduces the velocity of the reaction front.

In this section, we assumed that we always have the same total volume consisting of gaseous and solid volume fractions. However, despite the change in permeability, Schaube et al. [2013a] detect a change of around 10% in the volume of reactor filling during their experiments. A reversible change in permeability is a realistic approximation for the first few reaction cycles. After several cycles of charging and discharging however, agglomerates evolve. In between them, fracture-like patterns are observed [Roßkopf et al., 2014]. Those morphological changes potentially affect the flow processes and the reaction behavior even more.

Accounting for such effects requires a considerably more complex model, such as a double-porosity or a discrete fracture model. Those models come along with new processes and parameters, that need to be adapted appropriately to the reaction system $CaO/Ca(OH)_2$. In the following section, we present an approach to include the preferential flow paths as discrete fractures.

4.4 Discrete Fractures in the Reaction Bulk

Due to shrinking and swelling of the solid $CaO/Ca(OH)_2$-particles during repeated charging and discharging in fixed-bed reactors, compacted areas traversed by preferential flow paths develop as described in Section 2.5.1. Figure 2.4 shows this effect with a view into the reactor. Once the agglomerates are formed, the homogeneous gas flow is disturbed and the gas flows through the preferential flow paths for the most part [Roßkopf et al., 2014]. Schaube et al. [2013a] assume that the agglomerates cause diffusional limitations in directly operated reactors. [Roßkopf et al., 2015] state, that heat and mass transfer are affected. To our knowledge, this effect has not been considered in any numerical model of thermochemical fixed-bed reactors yet. Due to the severe impacts on the efficiency of the heat storage reactor, it is important to understand this effect, so that, in a next step, solutions can be found.

The formation of the agglomerates is highly complex and its modeling is beyond our scope. Instead, we aim to capture the reaction behavior once the agglomerates and channels have developed. Therefore, we enhance the model of the previous sections by a discrete fracture network. The discrete fractures represent the channels and the bulk in between them forms the agglomerates. For simplicity, we term the fracture-like channels "fractures" in the following. Starting from Figure 2.4, we conceive different scenarios to capture different fracture traits. The fracture scenarios with the specific simulation setups are presented in the subsequent section, followed by the simulation results and a conclusion.

4.4.1 Fracture Scenarios[4] and Simulation Setup

Figure 2.4 shows multiple fractures of different apertures distributed in the reactive bulk. Some of the fractures are connected. Gollsch et al. [2015] present a view on the inlet region where there is only one fracture visible at the inlet surface. Different fracture patterns possibly have different impact on the gas distribution in the solid bulk. For example, for a flow path from inlet to outlet, we suspect the injected gas to leave the reactor interacting only barely with the solid. To investigate different patterns, we formulated three different Scenarios, as displayed in Figure 4.5: (a) Scenario 1 features one single, straight fracture that connects the in- and outlet; (b) In Scenario 2, ten vertical and horizontal fractures are randomly distributed in the reactive bulk with few connections. In- and outlet are not directly connected by a path through the fractures; (c) Scenario 3 is a combination of the two previous scenarios: ten horizontal and vertical fractures are distributed in the reactor and connected such, that there is a fracture pathway connecting the inlet and the outlet of the reactor.

The fracture geometries are built with the software *FrackIt* [Gläser et al., 2020a] and meshed subsequently with *Gmsh* [Geuzaine and Remacle, 2009].

From Figure 2.4, we estimate the fracture apertures to 0.5 - 1mm. Due to the opening, the fractures are expected to feature a higher conductance than the porous bulk. Lacking further information, we follow the Hagen-Poiseuille law for a flow between two plates to get a first idea of the fracture permeability $\mathbf{K}_{frac} = \frac{h^2}{12}$. However, we account additionally for a residual solid content in the fracture domain and assume a considerable roughness of the fracture planes. We therefore estimate the permeability smaller compared to the values deterimed by the Hagen-Poiseuille equation. For a fracture aperture of 0.5 mm we assign the permeability $\mathbf{K}_{frac}$ = 3.33e-10 m^2, for 1.0 mm a permeability of $\mathbf{K}_{frac}$ = 3.33e-9 m^2. We account for a compaction of the bulk in the permeability of $\mathbf{K}_{bulk}$ = 5.3e-13 m^2. In the previous sections with homogeneous bulk, the permeability was $\mathbf{K}_{bulk}$ = 8.5e-12 m^2. For simplicity, we assume, that the permeabilities of bulk and fracture stay constant during the reaction.

We simulate the discharge reaction with two different simulation setups for the three fracture scenarios and a homogeneous reference case: At first, a setup with fixed pres-

[4]The fracture scenarios were developed in a supervised Bachelor's thesis, J. Schönherr: Untersuchung von Rissstrukturen bei der thermochemischen Wärmespeicherung mit $CaO/Ca(OH)_2$, *Bachelor's Thesis*, Universität Stutgart, 2020.

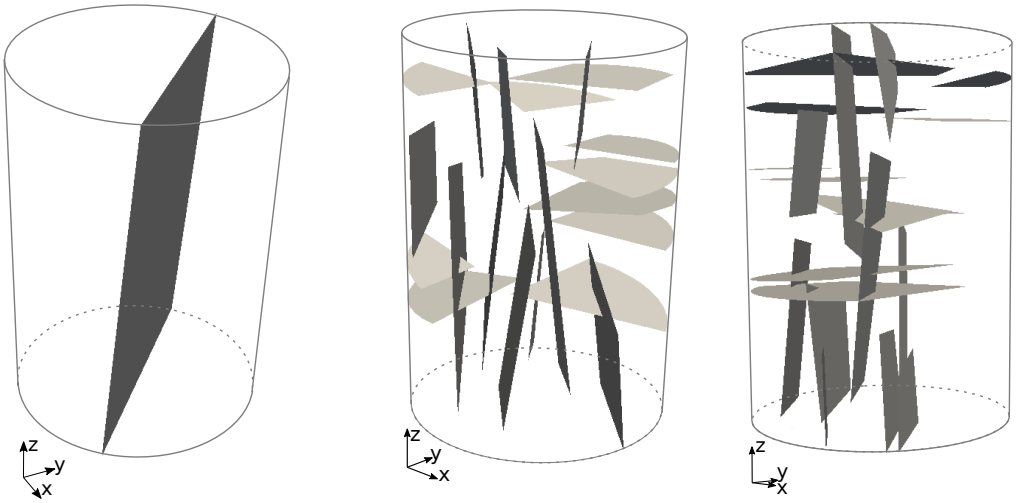

(a) Scenario 1: One continuous fracture connecting in- and outlet.

(b) Scenario 2: Multiple fractures without connection between in- and outlet

(c) Scenario 3: Multiple fractures connecting in- and outlet

Figure 4.5: Different scenarios for fracture distributions in the bulk

sure and concentrations at in- and outlet. This setup builds and continues on the setup presented in the supervised Bachelor's Thesis [Schönherr, 2020]. The outlet region is enhanced by a small additional simulation domain with non-reactive high-permeability material, so that the concentration and temperature of the fluid leaving the actual reactor domain is not affected by the boundary conditions at the outlet of the simulation domain. Because of the the high permeability in the additional domain, the pressure at the outlet of the actual reactor domain is almost the same as at the outlet of the simulation domain. In the additional domain, advective fluxes dominate and thus, the concentrations of the boundary are not transported upstream. A sketch is presented in Figure 4.6a. The pressure and concentrations of H_2O and N_2 are chosen such, that they approximate the boundary conditions presented in the previous sections. However, the constant pressure condition implicates, that as much fluid flows through the reactor domain (including bulk and fractures) as is necessary to keep the pressure gradient constant. This implies, that especially with highly conducting fractures, much more gas flows through the reactor.

In the second setup, we imply a gas flux at the reactor inlet, such as in the previous

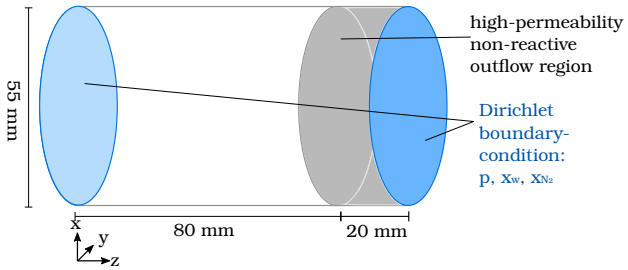

(a) Dirichlet boundary-condtions at reactor in- and outlet. A non-reactive high-permeability region at the outlet assures that the boundary does not affect the fluxes leaving the reactive domain.

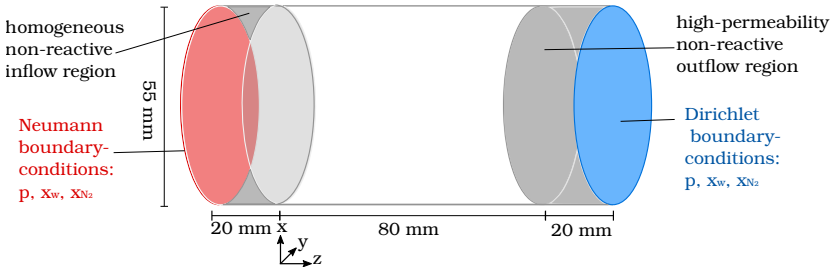

(b) Neumann boundary condition at the inlet; an additional homogeneous non-reactive inflow region distributes the injected gas evenly on the inlet surface.

Figure 4.6: Two sets of boundary conditions for the 3-D fracture setups. For both, the lateral surface of the cylinder is associated with Neumann no-flow boundary conditions;

sections of this chapter. In order to distribute the flux evenly over the surface of the reactor inlet, a homogeneous non-reactive domain is also placed in front of the actual reactor domain. The gas then enters, according to the pressure conditions, either the bulk or the fracture at the actual reactor domain. The amount of injected gas however is constant and thus, the pressure gradient adapts accordingly to the overall reactor permeability. A sketch is presented in Figure 4.6b.

Initial and boundary conditions for the two different simulation setups of boundary conditions are listed in Table 4.8. We used again the general material properties of the reaction system $CaO/Ca(OH)_2$ summarized in Table 2.2.

4.4.2 Results

At first, we present the simulations with fixed pressure boundary conditions and compare the three fracture scenarios each for apertures of 0.5 and 1 mm. Afterwards, we

Table 4.8: Boundary conditions for the simulation setups of the fractured bulk; The solid is immobile and therefore, only initial conditions for their volume fractions are formulated. z = 0 cm is on the bottom, z = 8 cm on the top of the reactor, r = 2.75 cm is at the boundary of the cylinder-shaped reactor casing. Depending on the simulation setup, an additional inflow/outflow region is placed before/after the actual reactor domain, see Figure 4.6.

Case	Condition	Location	Primary variable	Value
Dirichlet for In- and Outlet	Boundary	z = 0 cm	p	p = 4 bar
			x_{H_2O}	$x_{H_2O} = 0.5$
			T	T = 573.15 K
		z = 8 + 2 cm	T	T= 773.15 K
			x_{H_2O}	$x_{H_2O} = 0.3$
			p	$p = 2.0$ bar
		r = 2.75 cm	all	Neumann no-flow
	Initial	z $\leq$ 10 cm	p	$p = 2.0$ bar
		z $\leq$ 10 cm	x_{H_2O}	$x_{H_2O} = 0.5$
		z $\leq$ 10 cm	T	T = 573.15 K
		z $\leq$ 8 cm	θ_{CaO}	$\theta_{CaO} = 0.2$
		z $\leq$ 8 cm	$\theta_{Ca(OH)_2}$	$\theta_{Ca(OH)_2} = 0.0$
Neumann at Inlet Dirichlet at Outlet	Boundary	z = -2 cm	p	$q_{N_2} = 2.33$ mol s^{-1}
			x_{H_2O}	$q_{H_2O} = 2.33$ mol s^{-1}
			T	T = 573.15 K
		z = 8 + 2 cm	T	T= 773.15 K
			x_{H_2O}	$x_{H_2O} = 0.3$
			p	$p = 2.0$ bar
		r = 2.75 cm	all	Neumann no-flow
	Initial	z $\geq$ 0 & $\leq$ 10 cm	p	$p = 2.0$ bar
		z $\geq$ 0 & $\leq$ 10 cm	x_{H_2O}	$x_{H_2O} = 0.5$
		z $\geq$ 0 & $\leq$ 10 cm	T	T = 573.15 K
		z $\geq$ 0 & $\leq$ 8 cm	θ_{CaO}	$\theta_{CaO} = 0.2$
		z $\geq$ 0 & $\leq$ 8 cm	$\theta_{Ca(OH)_2}$	$\theta_{Ca(OH)_2} = 0.0$

highlight the influence of the boundary condition and present simulation results with the Neumann boundary condition for the influx.

Comparing the Three Fracture Scenarios (Dirichlet Boundary Conditions)

Figure 4.7 shows the temperature distribution for the three different fracture scenarios after 400 seconds of hydration and Figure 4.8 after 1000 seconds of hydration. The temperature indicates thereby the progress of conversion. The temperature is high at

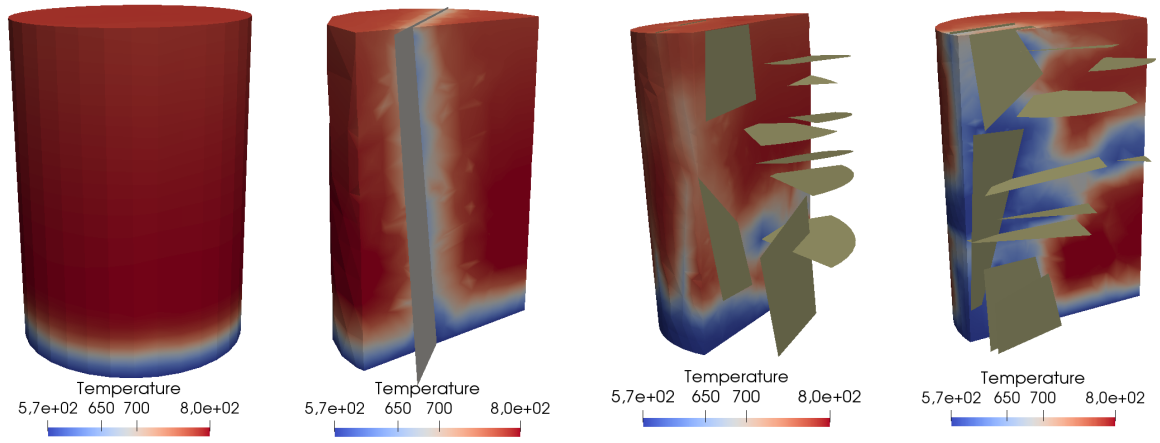

(a) Reference case (b) Scenario 1 (c) Scenario 2 (d) Scenario 3

Figure 4.7: Temperature distribution in the bulk for the different fracture scenarios at 400 s.

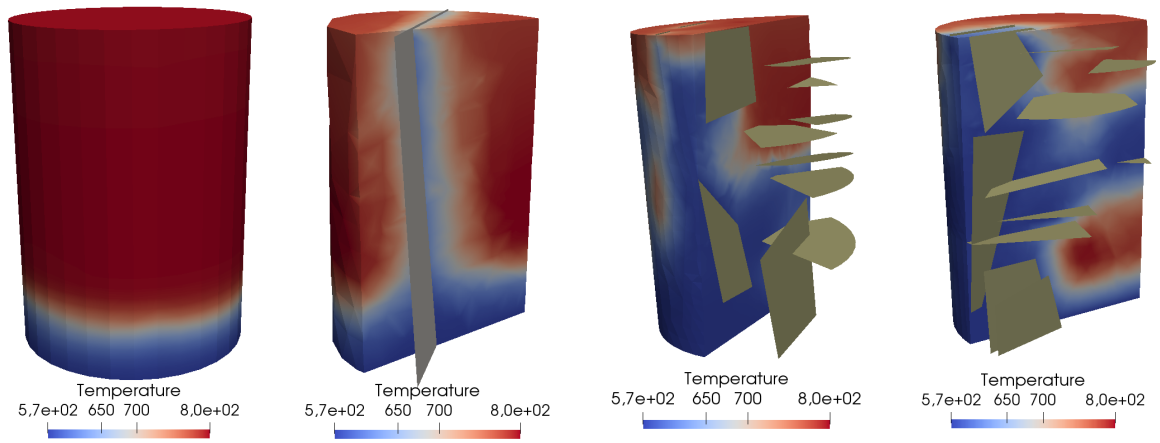

(a) Reference case (b) Scenario 1 (c) Scenario 2 (d) Scenario 3

Figure 4.8: Temperature distribution in the bulk for the different fracture scenarios at 1000 s.

locations, where the reaction is ongoing. If the bulk has cooled down to the initial temperature of 573.15 K, the solid is converted. Figures 4.7 and 4.8 show, that all fracture scenarios increase the area of the reaction front. However, only fractures that are either connected to the inlet, such as in Scenario 1, or fractures, connected to a region where the reaction front has already passed, deliver heat and water vapor for an increased reaction region. In Figure 4.8c on the top right, there are disconnected fractures, where the temperature is still high and thus, no reaction is happening. Comparing Figures 4.7c and 4.8c shows that isolated fractures at an early reaction time don't increase the reaction region.

Table 4.9: Overview of the simulation results with Dirichlet boundary conditions for the different fracture scenarios. Reference: homogeneous case; Scenario 1: 1 continuous fracture; Scenario 2: multiple fractures without connection; Scenario 3: multiple fractures connecting in- and outlet

	Ref.	**Scenario 1**		**Scenario 2**		**Scenario 3**	
Fracture aperture	-	0.5 mm	1 mm	0.5 mm	1 mm	0.5 mm	1 mm
Time for 100 % conversion [s]	7490	5490	5490	4760	4430	5030	4000
Time for 80 % conversion [s]	5000	1840	1720	1590	1272	1700	990
Fracture H_2O injection for 100% conversion [mol]	-	69.3	1414.5	16.5	25.7	47.5	500.7
Overall H_2O injection for 100% conversion [mol]	18.0	85.9	1431.2	41.6	50.9	53.6	504.5
Overall H_2O injection for 80% conversion [mol]	11.1	27.5	447.3	12.0	12.8	16.3	123.0
Fracture E injection for 100% conversion [10^3kJ]	-	5.01	102.19	1.19	1.85	3.44	36.17
Overall E injection for 100% conversion [10^3kJ]	1.29	6.19	103.39	2.30	3.68	3.85	36.43
Overall E injection for 80% conversion [10^3kJ]	0.79	1.97	32.3	0.85	0.91	1.16	8.87
Net E output [kJ]	207.7	207.8	207.8	209.1	209.1	209.1	209.1
η_E 100 % conversion [%]	16.1	3.4	0.2	6.9	5.7	5.4	0.6
η_E 80 % conversion [%]	21.0	8.4	0.5	19.7	18.4	14.4	1.9
Effective overall permeability [m^2]	5.3e-13	2.4e-12	3.9e-11	1.4e-12	1.8e-12	1.7e-12	1.9e-12

With the fixed pressure at in- and outlet of the reactor, significantly more gas flows through the reactor containing fractures than in the homogeneous reference case. Table 4.9 summarizes the amounts of injected mass and energy until complete conversion for the fracture scenarios at the two different apertures and the homogeneous reference. The fractures increase the overall permeability, and thus, the maintained pressure gradient induces a higher gas flux. The overall reactor permeability is determined according to Darcy's law with the pressure difference between in- and outlet, and the overall gas flux once the conversion is finished, see Table 4.9.

The predominant part of the injected gas flows through the highly permeable fractures without interacting with the solid bulk. As the fractures are not connected in Scenario 2,

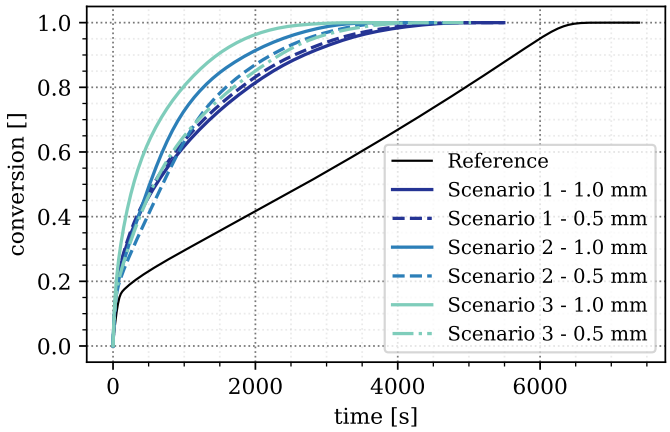

Figure 4.9: Overall conversion for the different fracture Scenarios 1-3 each for two different fracture apertures and the corresponding fracture permeabilities simulated with fixed pressure conditions.

the gas flux is forced to enter the bulk domain, where it is available for use in the reaction. Hence, this scenario requires the minimum of injected amount of gas flow necessary for complete conversion for both fracture apertures of all fracture scenarios.

The gas is injected at 573.15 K and carries the inherent amount of energy. We define the energetic efficiency as the ratio of net energy outcome devided by the injected amount of energy,

$$\eta_E = \frac{E_{net,out}}{E_{injected}}. \tag{4.7}$$

As much more gas is injected for all fracture scenarios, their efficiencies are reduced significantly compared to the homogeneous reference. The maximal efficiency for the given setup amounts to 16.1 % at complete conversion. The net energy output for the different simulation cases varies between 207.7e3 kJ to 209.1e3 kJ due to numerical errors. Table 4.9 lists the resulting efficiencies for complete and 80 % conversion.

Table 4.9 furthermore displays the times for overall and 80 % conversion of the different fracture scenarios with two different fracture apertures. For the fracture scenarios, 80 % solid is converted in roughly one third of the time for total conversion. Seen the other way round, most of the time is spent for the conversion of the last 20 % of solid bulk, if fractures are present. Figure 4.9 shows the global conversion over time for all fracture scenarios with the two different aperture sizes. The conversion of the homogeneous reference scenario increases linearly once the reaction is at equilibrium after

a few seconds in most of the reactor. All the fracture scenarios feature a hyperbolic conversion progress. They are converted at least 2000 seconds faster than the homogeneous reference for the setup with fixed pressure at in- and outlet. At early reaction times, the increased flux in the fractures increases the area where conditions far from equilibrium allow the bulk to react. This is reflected in the energetic efficiency for 80 % conversion, which is significantly higher than the efficiency for complete conversion for all fracture scenarios. The effect of the increased flux decreases until the bulk close to the fracture is converted. Due to changed pressure gradients in the bulk compared to the homogeneous scenario, compartments far from the fractures are less supplied by the gas flux and are thus converted only slowly. This causes the slow conversion progress at the final stages. This is particularly evident in Scenario 1 with 1 mm aperture, where hardly any gas flows from the fracture into the bulk. Consequently, the efficiency drops to 0.2 %. For the fracture aperture of 0.5 mm the difference in permeability between bulk and fracture is smaller, more gas reaches the bulk, resulting in a better efficiency (3.4 %). In Scenario 3, the fractures are distributed over the reactor domain and have a larger interaction area so that more gas is exchanged between fracture and bulk compared to Scenario 1 for both fracture apertures. However, the conductance is highest in the connected fracture pathway and the efficiency for the 1 mm aperture is with 0.6 % poor as well. Scenario 3 with 0.5 mm fracture aperture has a notably higher efficiency compared to the larger aperture. Here, the distribution effect of the fractures is not completely overlaid by the drainage of the conducting fractures. The differences due to the fracture apertures are less dominant in Scenario 2, where the gas is forced to enter the bulk domain, as the fractures are not connected. With 5.7 % (1 mm aperture) and 6.9 % (0.5 mm aperture) the efficiencies of Scenario 2 are the highest within all the fracture scenarios.

Influence of the boundary conditions (Neumann and Dirichlet Boundary Conditions)

The simulation results with the given Neumann boundary for influx differ significantly from the results of the Dirichlet boundary condition. Whereas a certain pressure gradient induces a fluid flux in a porous medium, a given flux rate builds up a pressure gradient according to the sample's permeability. Fractures, especially the connected fractures, enhance the permeability and thus reduce the overall pressure increase for a

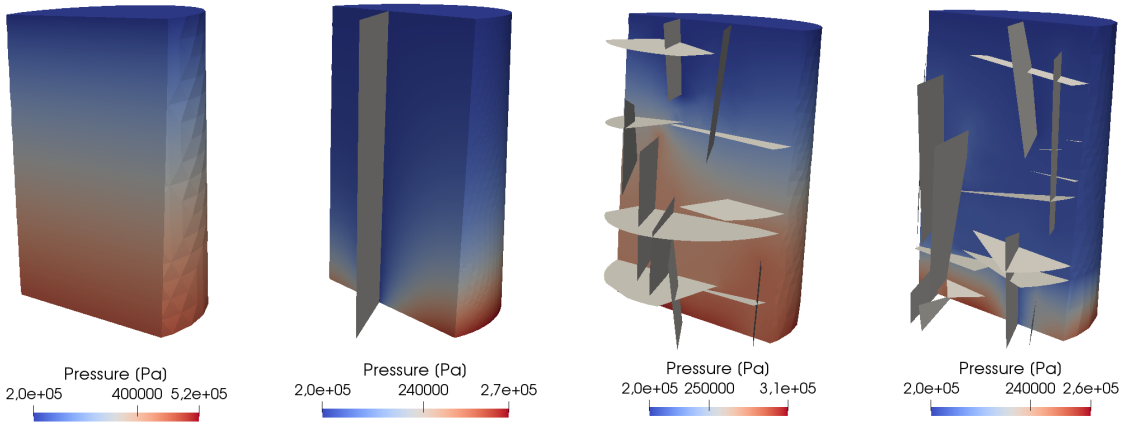

(a) Reference case (b) Scenario 1 (c) Scenario 2 (d) Scenario 3

Figure 4.10: Pressure distribution for the flux boundary condition in the different Scenarios. Each figure is scaled individually.

Table 4.10: Overview of the simulation results for the different fracture scenarios with Neumann boundary conditions. Reference: homogeneous case; Scenario 1: 1 continuous fracture; Scenario 2: multiple fractures without connection; Scenario 3: multiple fractures connecting in- and outlet

	Ref.	**Scenario 1**		**Scenario 2**		**Scenario 3**	
Fracture aperture	-	0.5 mm	1 mm	0.5 mm	1 mm	0.5 mm	1 mm
Time for 100 % conversion [s]	4340	15740	15150	10150	10700	8729	15000
Time for 80 % conversion [s]	2520	5100	5110	3050	3078	3359	4400
Overall H_2O injection for 100% conversion [mol]	23.7	84.9	81.7	52.5	55.4	45.2	77.7
Overall H_2O injection for 80% conversion [mol]	13.8	27.5	27.5	15.7	15.9	17.3	22.8
Overall E injection for 100% conversion[10^3kJ]	1.71	6.13	5.91	3.78	4.00	3.27	5.61
Overall E injection for 80% conversion [10^3kJ]	1.00	1.99	1.99	1.14	1.15	1.26	1.65
net E output [kJ]	210.5	209.9	209.1	209.6	209.3	209.1	209.1
η_E 100 % conversion [%]	12.3	3.4	3.5	5.5	5.2	6.3	3.7
η_E 80 % conversion [%]	16.8	8.4	8.4	14.7	14.5	13.3	10.1
maximum pressure built-up [bar]	2.7	0.9	0.7	1.3	1.1	1.0	0.6

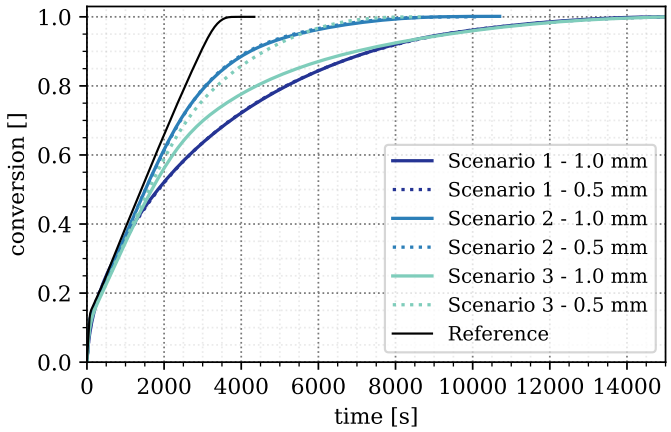

Figure 4.11: Overall conversion for the different fracture Scenarios 1-3 each for two different fracture apertures and the corresponding fracture permeabilities simulated with the flux boundary condition. For Scenarios 1 and 2, the plots for the two apertures almost coincide.

determined fluid flux. The pressure distributions for the different scenarios simulated with inlet flux boundary are shown in Figure 4.10. For the homogeneous reference, the pressure difference between inlet and outlet of 2.7 bar corresponds roughly the Dirichlet boundary conditions of the Dirichlet setup (2 bar). The pressures of the fracture scenarios, however, are reduced dramatically. For Scenario 1, it amounts to 0.9 - 0.7 bar, for Scenario 2 to 1.3 - 1.1 bar, and for Scenario 3 only 1.0-0.6 bar, respectively for the fracture apertures of 0.5 and 1 mm, see Table 4.10.

Similarly to the fixed pressure conditions, the major part of the injected gas flows through the highly permeable fractures. Due to the smaller overall pressure gradient for the flux boundary condition, the pressure gradient between fracture and bulk is also reduced. Less gas exchange occurs between bulk and fracture. The distribution of the reactive gas deteriorates in the bulk. Consequently, the reaction progress is retarded, see Figure 4.11, resulting in notably longer times until complete conversion for all fracture scenarios compared to the homogeneous reference case. The Scenarios 1 and 3 for 1 mm aperture take more than three times as long compared to the homogeneous reference (Tab. 4.10), Scenario 2 and 3 for 0.5 mm aperture take more than twice the time.

The larger fracture surfaces of Scenario 3 with 1 mm fracture aperture enables a larger gas flux between bulk and fracture compared to Scenario 1. However, the results for

simulation time and overall fluxes are similar. Due to the low pressure gradients, the flux in the fracture affects mostly the fracture vicinity and penetrates only very slowly into the reactive bulk.

The conversion regime with its hyperbolic shape corresponds to the fixed pressure boundary setup, see Figure 4.11. Thus, 80 % conversion is reached after roughly three times the time required by the homogeneous reference. As most of the injected gas flows through the highly conductive fractures, for this setup of boundary conditions, a severe reduction of efficiency is observed as well for all fracture scenarios (Tab. 4.10).

The performance difference between the three fractures scenarios is smaller with the Neumann flux boundary condition compared to the Dirichlet pressure boundary condition. Also, the differences due to the different fracture apertures is small for Scenarios 1 and 2 (Fig. 4.11). The small differences in pressure have only little impact in the gas distributions. For Scenario 3, however, the setup with 0.5 mm aperture is converted in half of the time compared to the case with 1 mm fracture aperture. Same as in the setup with Dirichlet conditions, a slight reduction of the drainage effect due to a lower permeability in the fractures, the distribution effect of the fractures shows impact.

4.4.3 Conclusion

Highly conductive fractures enhance the overall permeability of the reactive bulk. If a pressure boundary is imposed, the fractures increase the overall flux through the bulk. If a flux is imposed, the pressure gradient decreases if fractures run through the bulk. The gas flows mainly in the highly conductive fractures. Thus, the efficiency is decreased significantly regardless of the arrangement of the fractures. The arrangement of the agglomerates and the ratio of permeabilities between fracture and bulk determine the extent of the degradation. The effect is more severe, if there is a connection between the fractures such that a pathway connects in- and outlet and less important, if the preferential pathways are widely branched.

In the immediate vicinity of the fractures, the distribution of the reactive gas is enhanced. In compartments far from the fractures however, reduced pressure gradients induce a poor supply with reaction fluid and thus the speed of reaction drops considerably. This results in a changed course of reaction. Whereas the conversion in the

homogeneous reactor bulk progresses linearly, it is fast at the beginning for the fractured bulk and decelerated towards the end. Most of the time for complete conversion is attributed to the last 20 %. This is in accordance with experimental findings: Schaube [2013] describes an increasing reaction time at later reaction cycles. Thereby, the conversion time until 80% is relatively constant in their setting, but the longer reaction time is attributed the last 20 %.

The conceptual description of the agglomerates by a fractured porous medium introduced several new parametrizations, such as the distribution, the aperture and the permeability of the fractures. The presented results show, that effects such as reduction of efficiency and longer times for complete conversion can be reproduced with this approach. It is thus a first step towards understanding the way the agglomerates change the bulk behavior. In order to describe the effects of the agglomerates quantitatively, the numerical model needs to be calibrated with appropriate experimental data.

In this section, we assumed that fracture apertures, porosities, and permeabilities of both bulk and fracture stay constant once the agglomerates are formed. However, it is assumed, that the reactive material still decreases in volume during the charge reaction the charge and increases during discharge reaction, so that fracture aperture and permeabilities change. Depicting such processes requires an even more complex model.

4.5 Summary

We presented a numerical model built in the numeric toolbox $DuMu^x$ to model the processes in a directly operated fixed-bed reactor for storing heat in the reaction of CaO with H_2O to $Ca(OH)_2$. We verified the numerical model in a benchmark together with the software packages OpenGeoSys (T. Nagel) and ANSYS Fluent (P. Ostermeier). The comparison showed matching results. The benchmark forms a state of the art for modeling fixed-bed reactors. The benchmark setup, however, is based on several simplifying assumption, that we tested in numerical experiments subsequently:

– It was shown, that the assumption of local thermal equilibrium is accurate for small particle sizes. Temperature differences between solid and gas for particles smaller than 50 μm, were shown to be negligible.

– The assumption of a constant porosity in the reactor bulk was identified as misleading. The solid bulk increases its volume by 50 % due to the thermochemical reaction from CaO to $Ca(OH)_2$ [Schaube, 2013] and decreases for the reverse reaction. If the bulk volume is constant, the change in solid volume is attributed to a change in porosity. This impacts the gas flow that provides the gaseous reactive component. With the numerical model we tested subsequently the influence of a changing porosity and of a porosity induced permeability change under the assumption of isotropic homogeneous bulk. The simulation results showed, that a changing porosity and permeability both influence the course of reaction as all the different processes are strongly coupled by the reaction rate. A changing porosity impacts the heat distribution that is one driving force of the reaction. A changing permeability changes the pressure if the gas flux is constant. This in turn influences the equilibrium temperature of the reaction, which, in combination with the actual temperature of the medium, again impacts the chemical reaction.

– Due to the shrinking and swelling of the porous bulk, agglomerates are formed, that change the gas distribution in a fixed-bed thermochemical reactor. In order to understand their effects, we dropped the assumption of a homogeneous bulk and included a discrete fracture network. The discrete fractures represent the preferential flow paths in between the agglomerates of solid bulk. We approximated the properties for the preferential flow paths based on pictures of an experimental reactor, where agglomerates had been formed (see [Roßkopf et al., 2014]). We formulated 3 scenarios to represent the spacial distribution of the flow paths. The simulation showed two effects of the preferential flow paths: They distribute the reactive gas in their vicinity, and they conduct the gas quickly out of the reactor. This results in a fast conversion at early reaction times and a considerable deceleration for the last 20 % of conversion. For all scenarios, the presence of preferential flow paths reduced the efficiency of the reactor. If the preferential flow paths are widely distributed, the decrease in efficiency is less severe than if the gas is conducted straightly from in to outlet.

5 Simulating the Indirectly Operated Reactor Type[2]

The indirectly operated reactor concept is composed of two functional units: The reactive bed containing the solid particles of $CaO/Ca(OH)_2$ and the heat transfer channel. The dosage of reaction fluid is decoupled from the heat transfer. Heat transfer channels (HTF) run through the reactor to transport the heat released or consumed by the chemical reaction. Only conductive heat but no mass is exchanged between the two units. The reaction bulk is connected by a filter plate to a water vapor environment with defined pressure. If water is consumed or relased in the reaction, the resulting pressure gradient induces an advective flux. Two different reactor setups are illustrated in the Figures 1.4 and 5.1.

Michel et al. [2014] compare the directly and the indirectly operated reactor concept for the reaction system Strontium bromide/water and state that, for the indirectly operated reactor concept, the heat transfer is the limiting factor to performance. Thus, the reactor geometry is aimed at minimizing the length for the conductive heat flux in the reactive bulk. The reactor geometries of [Michel et al., 2014, Schmidt et al., 2014] and [Schmidt et al., 2017] are designed so that a large, flat reaction bed is located next to a large surface of the HTF channel. The filter plate for providing water vapor and the HTF channel can be arranged perpendicularly to each other (see Figure 1.4 of the reactor setup presented in [Schmidt et al., 2014]), or in parallel (see Figure 5.1 with the experimental setup of [Schmidt et al., 2017]). In the case of a perpendicular arrangement, 3-dimensional effects occur. This needs to be considered when modeling [Ranjha and Oztekin, 2017]. In the parallel arrangement, the processes can be accurately represented in two dimensions.

[2]This section is based on G. Seitz, F. Mohammadi and H. Class: Thermochemical heat storage in a lab-scale indirectly operated $CaO/Ca(OH)_2$ reactor—numerical modeling and model validation through inverse parameter estimation. Applied Sciences, 11(2), 2021.

To begin with, we will enhance our numerical model presented in the previous chapters for representing the indirectly operated reactor concept. Secondly, we will validate the model with experimental data presented in [Schmidt and Linder, 2017] and [Risthaus et al., 2020]. However, the authors of the experiment detected unwanted heat losses across the reactor surface due to a defective insulation. After discharging, the temperature in the reactive bed drops below the temperature imposed in the HTF channel. Therefore, Risthaus et al. [2020] include volumetric heat-loss terms to the reaction bulk, where a temperature difference between ambient (room) temperature outside the reactor's insulation and bed temperature drive the heat losses. Linder et al. [2013] present a similar approach to fit the model results to experimental temperature measurements of an indirectly operated reactor. In our opinion, such a volumetric heat-loss term lacks physical substantiation and is rather a calibration term. Inside the reactive bed itself, heat is transported conductively due to temperature gradients and advectively due pressure gradients of the water vapor. If the insulation is deficient, the vapor vessel cools down. The temperature difference between the reactive bed casing (bed surface) and the vapor vessel induce the heat flux of the heat losses. With the present approach, we seek a match to the experimental data based on a more objective substantiation of the physical background.

In Section 5.1, we first present the experimental setup and based on this, the numerical model enhancement including the reactive bed and the heat-transfer channel with the underlying simplifying assumptions, and possible mechanisms for the heat losses. We present initial simulation results in Section 5.2, where we detect additional uncertain parameters to those describing the mentioned heat losses. Given the experimental data, determining the uncertain parameters poses an inverse problem. To calibrate the numerical model, we apply Bayesian parameter inference. This allows to not only deliver the value of a parameter, but a probability range, which furthermore provides information on the sensitivity of the respective parameter. Section 5.3 gives an overview of the Bayesian model framework and the inference procedure. Finally, in Section 5.4, we present and discuss the results of model calibration and subsequent validation.

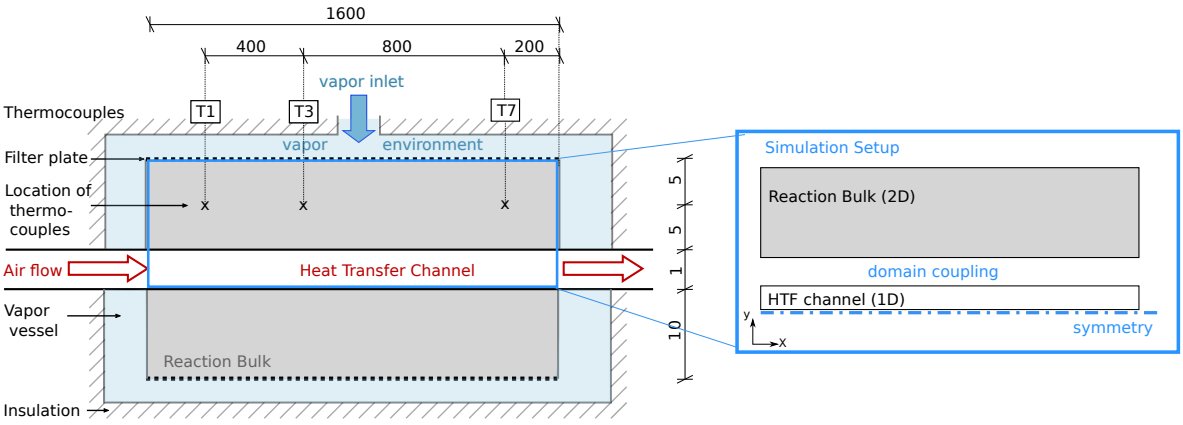

Figure 5.1: Reactor setup; **Left**: Sketch of the experimental setup modified according to [Schmidt et al., 2017]. The solid bulk is placed between filter plates. Water is provided at constant pressure in the surrounding casing. Air flows through the heat-transfer channel to provide / remove heat. Thermocouples are placed at the locations T1, T3 and T7. The lengths are given in mm. For better visibility, the figure is not to scale. The reactive bed streches 0.15 m to the z-direction (third dimension). **Right**: In the model, the setup consists of two separate domains: the reactive bulk and the heat-transfer channel (HTF). The two domains are coupled by a conductive heat flux. Due to symmetry, only half of the bulk is simulated.

5.1 Experimental Setup and Model Specification

Figure 5.1 to the left shows the reactor setup of [Schmidt and Linder, 2017]. The fixed-bed contains 2.4 kg of solid (in the form of $Ca(OH)_2$) in a volume of 4.8 l [Schmidt et al., 2017]. The reactive bulk is placed between filter plates which represent the connection to the surrounding vapor vessel. There, water vapor, the reaction fluid, is provided with a a constant gas pressure. As soon as water is consumed by the discharge reaction, a pressure gradient between reactive bed and vapor vessel develops, inducing an advective flux into the reactive bed. The HTF channel is placed in the middle of the reactive bed and separates it in two parts. Air is used as heat-transfer fluid in the HTF channel to remove/provide heat at a defined temperature.

The reactive bed is initially filled with CaO-powder. The discharge reaction is initiated by increasing the pressure in the vapor vessel above the equilibrium pressure. CaO powder starts to convert to $Ca(OH)_2$ by consuming water vapor. The released heat induces a temperature difference between bulk and HTF channel, so that the heat is conducted towards the channel. Here, a constant volume flux of air removes the heat and keeps the reaction going until complete conversion. A reaction front moves from

left to right according to the direction of flow in the HTF channel. The vapor pressure in the vessel and the volume flux of air in the HTF channel determine the temperature level of the reaction and the speed of the discharge. Several thermocouples in the reactive bed monitor the temperature and by that provide information on the course of reaction. The measurement locations are indicated in Figure 5.1. Besides, the global conversion is measured as a function of the consumed water [Schmidt et al., 2017].

The vessel containing all the reactor units is insulated. It is furthermore heated to the initial temperature of 773.15 K [Schmidt and Linder, 2017], which is the same as imposed in the HTF channel. Nevertheless, temperatures measured by the thermocouples fall below the predefined temperature of the HTF channel after conversion: 764 K at measurement point T1, 763 - 765 K at measurement point T3 and 757 K at measurement point T7 [Schmidt and Linder, 2017]. As the imposed temperature in the HTF channel is constant, the heat must be lost due to a lower temperature in the vapor vessel. Section 5.1.3 contains possible mechanisms for describing the heat losses.

Our focus concentrates on the modeling of the reactive bed. However, the processes in the HTF channel are crucial for the reaction behavior. We therefore represent both domains by two coupled submodels, see Section 3.3.2. The remaining details of the reactor are imposed as boundary conditions to the simulation domain. Just like [Risthaus et al., 2020], we use the symmetry condition to reduce the simulation area to half of the fixed-bed. Figure 5.1 (right) displays the simulation domain. The specifications for the modeling setup of the submodels and the description of the heat loss mechanism are outlined in Sections 5.1.2, 5.1.3 and 5.1.1.

Schmidt et al. [2017], and Schmidt and Linder [2017] performed several experiments with the same experimental setup at different water vapor pressures and air volume fluxes. Risthaus et al. [2020] published additional experimental results to the same setup. For calibrating our model, we use the experimental results of Case A in [Schmidt and Linder, 2017], and for validation, the data of the Reference case in [Risthaus et al., 2020]. The respective vapor pressure and air volume fluxes are listed in Table 5.1. For details concerning the experimental procedure, we refer to [Schmidt et al., 2017] and [Schmidt and Linder, 2017]. The boundary conditions resulting from the operation mode of the reactor are listed in Table 5.2. Table 2.2 contains the necessary material parameters.

Table 5.1: Vapor pressure and air volume fluxes of the experimental setups considered for model calibration and validation.

Case	**Vapor pressure** $p_{bulk,init}$ [kPa]	**Air flux** q_{air} $[\frac{\mathrm{Nm}^3}{\mathrm{h}}]$
Case S17 (Case A in [Schmidt and Linder, 2017])	470	16
Case R20 (Reference Case in [Risthaus et al., 2020])	270	25

Table 5.2: Boundary and initial conditions for the experimental setup of [Schmidt et al., 2017]: q_{air} is the source term for the component air, $q_{\mathrm{H_2O}}$ the water source term, $q_{\mathrm{Ca(OH)_2}}$ the $\mathrm{Ca(OH)_2}$ source term, q_{CaO} the CaO source term and q_e the energy coupling term between bulk and HTF. The initial temperature for all simulation cases is $T_{init} = 773.15$ K

Domain	**Location**	**Primary variable and value**
HTF channel	$t = 0$	$p = p_{HTF,init}$, $T = T_{init}$
	$x = 0$	$q_{air} = q_{air}$; $T = T_{init}$
	$x = x_{max}$	$p = p_{HTF,init}$; $q_{energy} = 2q^e_{\mathrm{HTF}}$
Porous Bulk	$t = 0$	$p_{\mathrm{H_2O}} = p_{bulk,init}$; $T = T_{init}$; $\phi_{\mathrm{CaO}} = 0.1113$ [−], $\phi_{\mathrm{Ca(OH)_2}} = 0.0$ [−]
	$y = 0$	$q_{\mathrm{H_2O}} = 0$; $q_{\mathrm{CaO}} = q_{\mathrm{Ca(OH)_2}} = 0$
		$q_{energy} = q_e$
	$y = y_{max}$	$p_{\mathrm{H_2O}} = p_{bulk,init}$; $q_{\mathrm{CaO}} = q_{\mathrm{Ca(OH)_2}} = 0$; $q_{energy} = \frac{\rho_{\mathrm{H_2O}} K_{bulk}}{\mu_{\mathrm{H_2O}}} \nabla p_{y=y_{max}} \cdot h(\mathrm{H_2O}, T_{y=y_{max}}) + (T(y = y_{max}) - T_{BC})\alpha_{loss}$
	$x = 0$ & $x = z$	$q_{\mathrm{H_2O}} = q_{\mathrm{CaO}} = q_{\mathrm{Ca(OH)_2}} = 0$; $q_{energy} = (T(xy) - T_{BC})\alpha_{loss}$

5.1.1 Submodel for the Heat-Transfer Channel

As outlined in Section 3.3.2, we resolve the flow in the HTF channel in one dimension on the basis of the flow profile of a laminar plate flow. Due to the small width of the HTF channel (1 mm) and a moderate air flux, the corresponding Reynolds-numbers (Re, see Tab. 2.1) in the range between 900-1000 indicate that the flow is laminar and far away from transition to turbulent flow at Re $\approx$ 2200 [Gnielinski, 2010]. According to [White, 2016], compressibility effects are only relevant for large velocities (i.e. for Mach

numbers larger than 0.3) and are thus neglected. The Hagen-Poiseuille law describes the momentum balance of the channel flow with the permeability K for plate flow and the channel thickness l, $K = \frac{1}{12}l^2$. The resulting balance equation for mass and momentum are presented in Section 3.3.2.

The heat transfer between reactive bed and HTF channel is described by Equation 2.45. We assume that the heat conduction in the steel casing is much larger compared to the reactive bed and thus doesn't represent the casing in the model. The heat-transfer coefficient α_{HTF} depends on the fluid properties, which change with the fluid state of pressure and temperature. However, it is common to assume α_{HTF} as constant over the given surface [Mokheimer, 2002] and estimate it based on the Nusselt number Nu. Incropera [2013] lists the value Nu = 8 for a flat-plate cross section with a fully developed boundary layer and laminar flow. With the gas properties of air at 773 K according to [Reid et al., 1987] and the thickness of the HTF channel, the heat-transfer coefficient is in the range of $\alpha_{\mathrm{HTF}} = 440$ W/m^{2}K. Risthaus et al. [2020] follow the instructions of Gnielinski [2010] and yield $\alpha_{\mathrm{HTF}} = 250$ W/m^{2}K for heat transfer between the steel casing to the heat-transfer flux. A correct value of α_{HTF} is crucial to determine the heat flux between bulk and HTF channel. Thus, we calibrate this parameter by inverse modeling in Section 5.3. The heat exchange between reactive bulk and HTF channel is included as source term q^e_{HTF} to the energy balance equation (Eq. 3.34). It is multiplied with 2 since only half the reaction bulk domain but the complete HTF channel are resolved.

5.1.2 Submodel for the Reactive Bed

Other than the directly operated reactor concept, the gas phase in the reactive bed in the present setup contains only water vapor. Equation 3.1 balances the mass for the one component in the gas phase. For the solid phases, the same balance equations apply, namely Equation 3.4. Also, the energy balance equation is the same as in the directly operated reactor concept, Equation 3.7, still assuming local thermal equilibrium. However, the gas properties such as internal energy, density and heat conductivity are the properties of pure water vapor. We again use the reaction kinetics of [Schmidt, 2011] to include the chemical reaction. However, we enhance it by an exponent that reduces the reaction rate for progressed conversion $(1 - X)^{k_{R,2}}$, see Equation 5.1, in

order to fit the simulation results to the experimental data. This term will be subject to optimization and is addressed in more detail in Section 5.2.

$$k_R = k_{R,1}(1-X)^{(1+k_{R,2})}\frac{T-T_{eq}}{T_{eq}}X_{\mathrm{H_2O}}, \tag{5.1}$$

with the constants $k_{R,1}$, and $k_{R,2}$, and the conversion X. We use the formulation of [Samms and Evans, 1968] to determine the equilibrium temperature according to the van't Hoff law, as it suits best for the pressure ranges of the experiments:

$$\ln\left(\frac{p_{H_2O}}{1\ \mathrm{bar}}\right) = \frac{11375\ \mathrm{K}}{T_{eq}} + 14.574. \tag{5.2}$$

The next section adresses the description of the upper temperature boundary condition of the reactive bed to represent the heat losses.

5.1.3 Formulation of the Heat Loss

As outlined earlier, a temperature difference between the outer reactive-bed boundary and the vapor vessel is considered to cause the heat losses in the experiments of [Schmidt et al., 2017]. We assume that the heat is transported between two parallel plates (i.e. the filter plate and the vapor vessel casing, see Figure 5.1 left) with water vapor between them. The height of the reactive bed (2 cm) is much smaller than the length (1.6 m), so that we neglect heat losses on its vertical boundaries. According to [Incropera, 2013], several heat-transport mechanisms overlap and need to be considered:

- *Free convection* occurs, if a hot plate is located below a cooler plate. The gas close to the hot plate warms up and its density decreases. Due to buoyancy, the hot gas ascends and cooler gas descends. Eventually rotating cells of moving gas develop, which transport the heat between the plates. This effect occurs only from bottom to top. It is expressed as:

  $$q^e_{conv} = (T(y = y_{max}) - T_{BC})\alpha_{conv}, \tag{5.3}$$

  with the heat-transfer coefficient α_{conv}, the temperature in the reactive bulk at the top boundary (at location $y = y_{max}$), and the temperature of the pressure

vessel casing T_{BC}.

- *Radiation* between two flat plates of different temperature is determined by:

$$q^e_{rad} = \frac{\sigma(T(y = y_{max})^4 - T^4_{BC})}{\frac{1}{\varepsilon_{FP}} + \frac{1}{\varepsilon_{VV}} - 1}, \tag{5.4}$$

  with the Boltzmann constant $\sigma = 5.67\text{e-}8\ \mathrm{W\,m^{-2}\,K^{-4}}$, and the emissivities of the filter plate ε_{FP} and of the vapor vessel casing ε_{VV}. Radiation is important at high temperature differences and high values of emissivities. According to [Incropera, 2013], typical values for the emissivities of steel are in the range of 0.15 - 0.3.

- *Heat conduction* in the water vapor such as introduced in Equation 2.43.

The different heat-transport mechanisms share the same driving force, namely the difference in the temperature of the bounding walls of the reactive bed and the vapor vessel. For radiation, however, the driving force is proportional to the difference in temperatures raised to the power of four. Representing all mechanisms independently would produce several new parameters, all of which bear uncertainty. Additionally, the dimensions of the vapor vessel are not indicated in [Schmidt et al., 2017]. We aim at determining the overall heat loss in a spatially resolved manner, regardless of which mechanism dominates. Thus, for simplicity, we choose the following form for the overall heat-loss flux:

$$q^e_{loss} = (T(y = y_{max}) - T_{BC})\alpha_{loss}, \tag{5.5}$$

with the heat-loss coefficient α_{loss}, the temperature T in the reactive bulk at the top boundary (at location $y = y_{max}$), and the temperature of the pressure-vessel casing T_{BC}. As the temperatures measured at the locations T1, T3 and T7 all are different, we assign three degrees of freedom to the temperature distribution T_{BC}:

$$T_{BC} = k_1 x^2 + k_2 x + k_3. \tag{5.6}$$

The constants k_1 to k_3 and the heat loss coefficient α_{loss} are calibration parameters in the inverse modeling. Same as in Section 5.1.1, we assume the influence of the reactive bed casing and filter plate to be negligible, so we don't represent them in the numerical model.

5.2 Preliminary Calibration Attempt and Selection of the Optimization Parameters

We run preliminary simulations in order to mark out the ranges of the already identified uncertain parameters representing Case S17, see Table 5.1. We applied a linear T_{BC} distribution (i.e. $k_1 = 0$, $k_2 = -5.567$, and $k_3 = 764.99$) and the heat transfer parameters $\alpha_{\mathrm{HTF}} = 275$ W/m^{2}K and $\alpha_{loss} = 30$ W/m^{2}K. The results are shown in Figure 5.2 in orange. The simulated curves for the three temperatures T1, T3 and T7 roughly match the arrival time of the temperature jump after conversion in the respective region. However, the temporal temperature distribution differs between experiment and simulation. The slope at the temperature jump is much steeper in the simulation than in the experiment. Thus, the chosen parameters for heat transfer and heat loss are not sufficient to reproduce the experimental results, but further processes occur. Based on expert knowledge and trial-and-error, we test further mechanisms related to heat transport and heat release. The changed parameters for each simulation are listed in Table 5.3. Figure 5.2 displays the simulation results.

Porosity induced permeability change During the reaction, the solid volume and, thus, the permeability change. This has a notable effect on directly operated reactors [Seitz et al., 2020], as outlined in Section 4.3. We therefore tested, if this also affects the heat transport in the indirectly operated reactor type. Within the reactive bed of the indirectly operated reactor, most of the heat of reaction is transported due to heat conduction. The pressure gradients in the reactive bed are small and hence the advective heat transport. The gray dashed line in Figure 5.2 shows a simulation with permeability change from 8.8e-11 m^2 to 8.8e-12 m^2 according to the porosity change compared to the simulation in orange without permeability change. No effect on the temperature profile is visible. On account of this, we consider the influence of a permeability change to be negligible for the indirectly operated reactor.

Heat conductivity The temperature profiles of the experiment displayed in Figure 5.2 suggest that, at later times, the heat released by the reaction is affected by a heat transport mechanism. In the solid bulk, most of the heat is conducted in the solid volume fraction. Thus, conduction rises as the solid volume fraction increases during

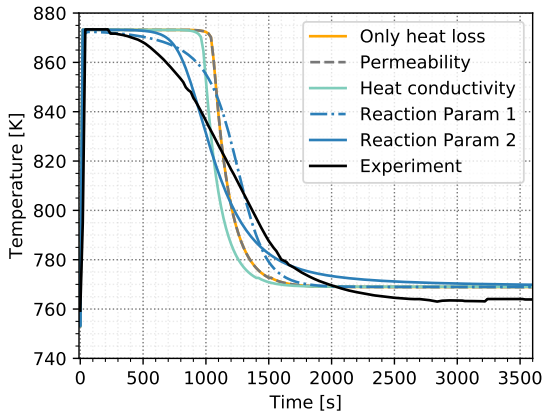

(a) Temperature measurement point T1

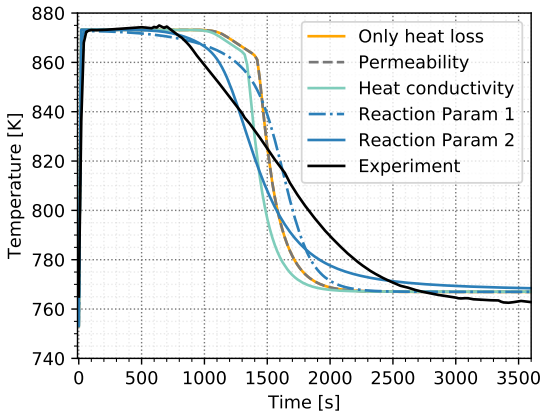

(b) Temperature measurement point T3

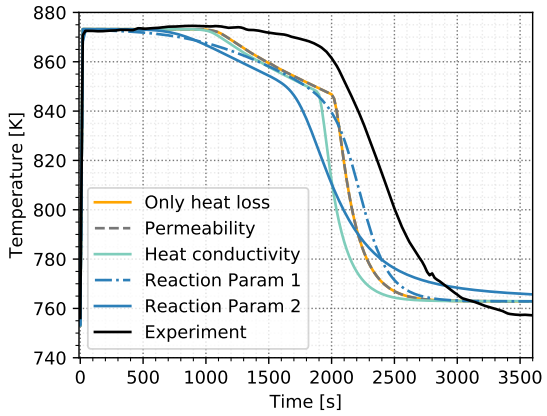

(c) Temperature measurement point T7

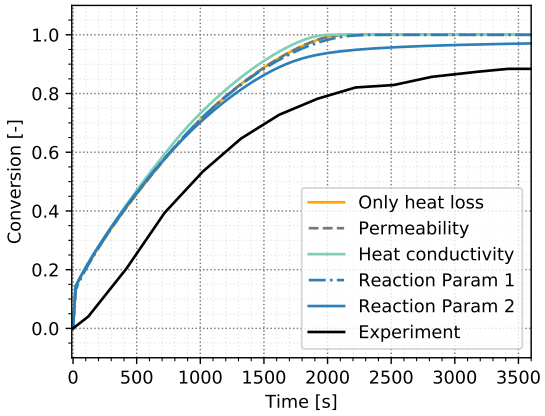

(d) Global conversion

Figure 5.2: Preliminary simulation results to identify the optimization parameters. In black: experimental values from Schmidt and Linder [2017] as reference; Simulation cases: "Only heat loss" is simulated with the standard parameters at constant permeability. "Permeability" applies a permeability change due to porosity alteration, "Heat conductivity" uses different values for solid heat conductivity for CaO and $Ca(OH)_2$, "Reaction Param 1" applies a reduced reaction rate constant $k_{R,1}$ and "Reaction Param 2" introduces the constant term $k_{R,2}$ to the reaction kinetics. The parameters for each simulation case are listed in Table 5.3.

conversion. We tested the effect of an increased heat conductivity of $Ca(OH)_2$ in the simulation results, displayed by the light blue lines in Figure 5.2. The enhanced heat conduction makes the solid react faster, the front is shifted to earlier times. However, the steepness of the temperature jump is not changed. The simulations are hence continued with the literature values for solid conductivity listed in Table 2.2.

Reaction Rate Nagel et al. [2014] and Risthaus et al. [2020] apply the same reaction kinetics but with different rate constants. Nagel et al. [2014] choose $k_{R,1} = 0.2\ s^{-1}$, whereas Risthaus et al. [2020] use $k_{R,1} = 15\ s^{-1}$. The influence of this parameter is shown in the dashed blue line in Figure 5.2. This curve results from a simulation with $k_{R,1} = 0.2\ s^{-1}$, whereas the previously described simulations are performed with $k_{R,1} = 10\ s^{-1}$. Obviously, reducing this parameter renders the temperature curve more smooth and also slightly reduces the slope at the temperature jump. Further reducing the reaction rate constant, however, prevents reaching the equilibrium temperature plateau. Thus, varying the reaction rate constant $k_{R,1}$ is not sufficient to reproduce the shape of the temperature distributions. Therefore, we multiply the reaction rate by an additional term that becomes limitating at progressed conversion: $(1 - X)^{k_{R,2}}$. For $k_{R,2} = 0$, the reaction kinetics correspond to Equation 2.54. Simulation results for $k_{R,2} = 2$ are displayed in the solid blue lines in Figure 5.2. The combination of the two reaction constants, $k_{R,1}$ and $k_{R,2}$, generates both a plateau at equilibrium temperature and a flatter slope at the temperature jump.

Table 5.3: Summary of the simulation cases displayed in Figure 5.2

Case	α_{HTF}	α_{loss}	**K**	λ_{CaO}	$\lambda_{\mathrm{Ca(OH)_2}}$	$k_{R,1}$	$k_{R,2}$
Heat losses	275	30	$8.8e-12$	0.4	0.4	10	0
Permeability	275	30	$8.8 \cdot 10^{-11} - 8.8 \cdot 10^{-12}$	0.4	0.4	10	0
Heat conductivity	275	30	$8.8e-12$	0.3	0.5	10	0
Reaction param 1	275	30	$8.8e-12$	0.4	0.4	0.2	0
Reaction param 2	275	30	$8.8e-12$	0.4	0.4	1	1

With the heat loss and transfer parameters (α_{loss}, α_{HTF}), the constants to represent the temperature distribution of the vapor vessel (k_1 - k_3) and the two reaction rate constants ($k_{R,1}$, $k_{R,2}$), seven parameters in total are selected for optimization by inverse modeling. The parameters and the considered ranges are listed in Table 5.4.

Table 5.4: Parameters selected for optimization and their respective ranges

Parameter	**Symbol**	**Unit**	**Range minimum**	**Range maximum**
Heat-transfer coefficient	α_{HTF}	W/m^2K	150	350
Heat-loss coefficient	α_{loss}	W/m^2K	0	350
Temperature distribution Param1	k_1	K/m^{-2}	-15	15
Temperature distribution Param2	k_2	K/m	-20	20
Temperature distribution Param3	k_3	K	740	780
Reaction coeffiecient	$k_{R,1}$	s^{-1}	0.1	20
Reaction exponent	$k_{R,2}$	-	0	3

5.3 Inverse Modeling [1]

Given the numerical model and experimental results, the determination of unknown model input parameters poses an inverse problem. We use Bayesian inference to deduce the unknown and uncertain parameters. The framework and the procedure is described in the following sections.

5.3.1 Bayesian Model Framework

Bayesian parameter inference is one of the methods of inverse modeling. Based on data from experimental measurements (observations) and some prior knowledge about the parameters to estimate, e.g. a meaningful physical range, Bayesian inference delivers a probability distribution for the unknown parameters. It furthermore takes the uncertainty of measurements and model into account.

We denote the unknown parameters $\boldsymbol{\theta}$, and $\mathcal{Y}$ the observed values. In the present context of parameter inference, the Bayes theorem states the following: the probability distribution of the parameters $\boldsymbol{\theta}$ with given observations $\mathcal{Y}$ can be determined by the probability of the observations $\mathcal{Y}$ at given parameters $\boldsymbol{\theta}$ multiplied by the *prior*

[1] The framework for the inverse modeling is the contribution of F. Mohammadi to [Seitz et al., 2021]. This section summarizes the methods and the algorithm used.

knowledge of the parameters $P(\boldsymbol{\theta})$ before knowing the observations divided by the evidence $P(\mathcal{Y})$:

$$P(\boldsymbol{\theta}|\mathcal{Y}) = \frac{P(\mathcal{Y}|\boldsymbol{\theta})P(\boldsymbol{\theta})}{P(\mathcal{Y})}. \tag{5.7}$$

Therein, $P(\boldsymbol{\theta}|\mathcal{Y})$ is termed *posterior distribution* and $P(\mathcal{Y}|\boldsymbol{\theta})$ the *likelihood function*. $P(\mathcal{Y})$ is the *marginal probability* or probability of the data. We assume that the measured data $\mathcal{Y}$ consist of N independent realizations $\mathcal{Y}_i$ at individual time steps of a time series and/or location. The evidence $P(\mathcal{Y})$ is a normalization constant, which doesn't depend on $\boldsymbol{\theta}$. It makes sure that the posterior distribution integrates to one.

Our model $\mathcal{M}$ represents the considered system based on the parameters $\boldsymbol{\theta}$ of the given input space $\mathcal{D}_{\boldsymbol{\theta}}$:

$$\mathcal{Y} = \mathcal{M}(\boldsymbol{\theta}) + \epsilon. \tag{5.8}$$

In that, ϵ denotes the difference between experimental data $\mathcal{Y}$ and the model output $\mathcal{M}(\boldsymbol{\theta})$. The discrepancy ϵ exists due to measurement errors and model uncertainties, see Section 5.3.2. The likelihood $P(\mathcal{Y}|\boldsymbol{\theta})$ can be expressed based on the independent measurements i for a given distribution of the model output $\mathcal{N}$.

$$\begin{aligned} P(\mathcal{Y}|\boldsymbol{\theta}) &:= \prod_{i=1}^{N} P(\mathcal{Y}_i|\boldsymbol{\theta}) \\ &= \frac{1}{\sqrt{(2\pi)^N \det \Sigma}} \exp\left(-\frac{1}{2}(\mathcal{M}(\boldsymbol{\theta}) - \mathcal{Y})^T \Sigma^{-1} (\mathcal{M}(\boldsymbol{\theta}) - \mathcal{Y})\right), \end{aligned} \tag{5.9}$$

with N, the number of independent measurements within $\mathcal{Y}$. The covariance matrix Σ comprises both measurement and model errors, see Section 5.3.2.

The practical computation of the posterior distribution is usually performed by a Markov chain Monte Carlo Method (McMC) [Wagner et al., 2019]. It directly draws samples from the posterior distribution $P(\boldsymbol{\theta}|\mathcal{Y})$ of the parameter space $\mathcal{D}_\theta$ spanned by the ranges of the input parameters. Therefore, there is no need to compute the normalization factor $P(\mathcal{Y})$. The samples are taken in a random walk procedure and thereby a Markov chain ($\boldsymbol{\theta}_1$, $\boldsymbol{\theta}_2$, ...) is constructed, where the next sampling point $\boldsymbol{\theta}_{t+1}$ only depends on the previous step $\boldsymbol{\theta}_t$. The transition probability $\Gamma(\boldsymbol{\theta}^{(t+1)}|\boldsymbol{\theta}^{(t)})$ determines, whether the next sampling point $\boldsymbol{\theta}_{t+1}$ is accepted or rejected. This results in an invariant distribution of the Markov chain. Once a sufficient number of samples is reached, the invariant distribution of samples is equivalent to the target, the posterior

distribution [Wagner et al., 2019].

There are different methods to construct Markov chains, see e.g. [Wagner et al., 2019]. In our case, several input parameters are correlated. For instance, both a large heat loss coefficient and a big temperature difference between bulk and vessel increase the heat loss. A promising McMC algorithm taking correlations into account is the Affine Invariant Ensemble Sampler (AIES) [Goodman and Weare, 2010]. It is provided in the python module *emcee* by [Foreman-Mackey et al., 2013]. This algorithm runs an ensemble of K Markov chains. Each chain is called a walker. The location $\boldsymbol{\theta}_i$ of the walker is updated for each walker successively. Typical for the AIES method is the so-called strech-move to generate suggestions for next walker candidate location $\boldsymbol{\theta}_i^{(*)}$:

$$\boldsymbol{\theta}_i^{(*)} = \boldsymbol{\theta}_i^{(t)} + Z(\boldsymbol{\theta}_j^{(t)} - \boldsymbol{\theta}_i^{(t)}), \tag{5.10}$$

with Z being distributed as:

$$\mathcal{Z} \sim p(z) = \begin{cases} \frac{1}{\sqrt{2}\left(2\sqrt{a} - \frac{2}{\sqrt{a}}\right)} & \text{if } z \in [1/a, a] \\ 0 & \text{otherwise.} \end{cases} \tag{5.11}$$

We set the parameter $a = 2$ according to e.g. [Foreman-Mackey et al., 2019]. The probability for the candidate $\boldsymbol{\theta}_i^{(*)}$ of the i-th walker in the ensemble to be accepted is the following:

$$p(\boldsymbol{\theta}_i^{(*)}, \boldsymbol{\theta}_i^{(t)}, z) = \min\left\{1,\ z^{N-1}\ \frac{p(\boldsymbol{\theta}_i^{(*)}|\mathcal{Y})}{p(\boldsymbol{\theta}_i^{(t)}|\mathcal{Y})}\right\}. \tag{5.12}$$

The Marcov chain converges if the acceptance rate ranges between 0.23 and 0.5 [Gelman et al., 1996]. A lower value indicates that nearly all steps are rejected and the sampling is not representative for the target density. For a larger value, most steps would be accepted with no regard for the target density.

The integrated autocorrelation time is a second criterion for convergence. It is determined as follows:

$$\tau_{\boldsymbol{\theta}} = \sum_{t=-\infty}^{\infty} \frac{C_{\boldsymbol{\theta}}(t)}{C_{\boldsymbol{\theta}}(0)}, \text{ with } C_{\boldsymbol{\theta}}(t) = \frac{1}{N-t} \sum_{k=1}^{N-t} \left(\boldsymbol{\theta}^{(k)} - \mu_{\boldsymbol{\theta}}\right)\left(\boldsymbol{\theta}^{(k+t)} - \mu_{\boldsymbol{\theta}}\right), \tag{5.13}$$

with $\mu_{\boldsymbol{\theta}}$ the arithmetic mean of the chain. We use an estimate of the integrated

autocorrelation $\tau_{\boldsymbol{\theta},e}$, provided in [Goodman, 2009]. One can compute this measure for the chain of each parameter, $\boldsymbol{\theta}$, and use the maximum and minimum values, $\tau_{\max} = \max_{0 \leq i < N} \tau_{\theta_j e}, \tau_{\min} = \min_{0 \leq i < N} \tau_{\theta_j e}$. The sampler is run until the sample size $j > 100 \cdot \tau_{max}$, and the convergence of the McMC sampler can be achieved, as soon as the difference in $\tau_{\boldsymbol{\theta}}$ from sample $j - \tau_{max}$ to sample j is less than 1%.

Each candidate $\boldsymbol{\theta}_i$ requires a run of the forward model $\mathcal{M}$. This is computationally expensive. To speed up the process, we replace the numerical model by a surrogate model. We apply *polynomial chaos expansion* (PCE) to approximate the model response of the measurement points (T1, T3, T7, and the global conversion), $\mathcal{M}$, by high-dimensional polynomials in the uncertain model parameters:

$$\mathcal{M}(\mathbf{X}) \approx \mathrm{Y} = \sum_{\alpha} c_\alpha \Psi_\alpha(\mathbf{X}), \tag{5.14}$$

with $\mathbf{X} \in \mathbb{R}^M$ a random vector within the space of events M, Ψ_α the multivariate polynomials and c_α the expansion coefficients. We determine c_α with the Bayesian sparse learning approach, see [Tipping et al., 2003]. Furthermore, we apply the *principal component analysis* to reduce the temporal dependency of the model output and obtain linearly uncorrelated parameters. This is achieved by an orthogonal transformation and is outlined in detail in [Higdon et al., 2008].

5.3.2 Errors and Uncertainties

Several steps of the inverse modeling entail uncertainties:

In the first place, the experimental data contain errors from several sources. Schmidt et al. [2017] indicate the accuracies of the applied measurement devices. We account furthermore for the fact that the measurement implementation contains errors. Therein, we consider the error that occurs, if the location of the thermocouples deviates by 0.5 mm from the indicated coordinates and if the measurement is delayed. Due to the large temperature gradients in the reactive bed, the influence of already a small shift of the thermocouple results in a notable difference in temperature. Especially in the first seconds, the temperature rises sharply and thus, a small delay causes large errors. Lastly, we take systematic errors into account. The different experimental runs of [Schmidt and Linder, 2017] don't always show full conversion and the results in

[Risthaus et al., 2020] to the same setup even show conversions larger than 100 %. We assign therefore uncertainties as the full conversion being within the confidence interval. The overall measurement error is displayed as error bars in Figures 5.5 and 5.6 at each time step.

Secondly, the model itself is deficient. We estimate the error of the numerical model due to discretization according to [Oberkampf and Roy, 2010] by comparing the model results of different grid resolutions and extrapolate it with a generalized Richardson extrapolation. We consider for the error, which is evoked by replacing the numerical model with the surrogate model, by the Bayesian Sparse Learning extension to PCE.

We account for the ensemble of all errors in the covariance matrix in Equation 5.9.

5.3.3 Solution Procedure

500 runs of the DuMu^x-model were realized with parameters covering the parameter space listed in Table 5.4. As the parameters are correlated, a uniform distribution of the parameters does not result in an equal distribution of the output space. There are several combinations of parameters that lead to an increased cooling, and thus a faster conversion. We conditioned the input space of the parameters such that it envelops the measurement distributions, i.e. there are simulation results above and below the measured temperature and conversion curves. Therefore, we limited the temperatures resulting from the three parameters k_1 - k_3, if a large heat loss coefficient α_{loss} was chosen. The resulting input space is displayed in the Appendix in Figure A.1. The simulation output of the DuMu^x-model is shown by the gray lines in Figure 5.5.

The surrogate model was trained with the simulation results of 500 runs of the DuMu^x-model. The McMC algorithm was run for an ensemble of 300 Markov chains based on the surrogate model for each sample point, until convergence was reached. We did not restrict the solution of the McMC algorithm to the parameter ranges given in Table 5.4 and thereby admitted extrapolated solutions.

5.4 Results and Discussion[2]

We inferred the optimization parameters listed in Table 5.4 with the algorithm presented in the previous section based on the experimental data of Case S17 (see Table 5.1). This corresponds to the model calibration. The results are presented and interpreted in Section 5.4.1. Subsequently, we simulated the experimental setup of Case R20 (see Table 5.1), in order to validate the surrogate model and, thus, the DuMu^x-model, see Section 5.4.2.

5.4.1 Calibration

Figure 5.4 shows the posterior distribution for the parameters and their dependencies. The optimum values and the 95 % confidence interval of each parameter are as well listed in Table 5.5. All the parameters display a Gaussian posterior distribution, i.e. the model output is sensitive to all the selected parameters. Otherwise, the posterior distribution would resemble the prior distribution displayed in Figure A.1. The narrower the width of the Gaussian distribution, the more sensitive the model output is to the respective parameter.

The heat-transfer coefficient has a narrow distribution and lies with a mean value of $\alpha_{\mathrm{HTF}} = 337$ W/m^{2}K at the upper bond of the selected range. The larger the heat-transfer coefficient, the more heat is transported to the HTF channel given the same temperature conditions. The heat transfer is, however, correlated to the heat loss mechanism, that transports the heat to the top of the reactive bed. It is described by the combination of the parameters α_{HTF}, α_{Loss} and k_1 - k_3. Both mechanisms depend on the temperature at the reactive bed boundary and the outer temperature of both the HTF channel and the vapor vessel. However, the temperature distribution in the HTF channel changes according to the progress of conversion. In early stages, the reaction occurs everywhere in the reactive bed. Cold air removes the heat first at the inlet, where the temperature difference is largest. Eventually, the reactive bed gets converted and the temperature front moves from left to right. The temperature in the outer vessel described by the parameters k_1 - k_3 is constant over time. Via the temperature profiles

[2]The figures in this sections except Figure 5.3 are created by F. Mohammadi.

at the locations T1, T3 and T7, it is thus inferred how much heat is transferred to the HTF channel or lost to the vapor vessel.

The heat loss is determined by the temperature difference between the reactive bed boundary and the vapor vessel, and the heat loss coefficient. The temperature distribution of the outer vessel is plotted in purple in Figure 5.3. It furthermore contains the temperatures at the boundary of the reactive bed, $T(y = y_{max})$, determined by a simulation with the DuMu^{x}-model with the optimized parameters. The temperature differences between bed and vessel amount to more than 100 K at early times of reaction. At the end of the experiment, they still amount to 20 K. Due to the big temperature differences, 1.34e3 kJ of the overall released energy of reaction (2.24e3 kJ) is lost through the reactor surface and only 0.90e3 kJ is transferred to the HTF channel. Temperature measurements in the HTF channel that could verify these results are not available. The heat-transport mechanisms of the heat loss, free convection, conduction and radiation, overlap. Free convection, however, appears only at the upper boundary of the symmetric reactor setup, as outlined in Section 5.1.3. If this mechanism dominates the heat loss, the temperatures in the reactive bed below and above the HTF channel are different and the symmetry condition is not fulfilled. In the experiment, all the thermocouples are installed in the top part of the reactive bed. Thus, the experiment does not provide any information on whether or not the two parts behave symmetrically. The reduced simulation domain provides a considerable simulation speed-up.

The parameters $k_{R,1}$ and $k_{R,2}$ are linked via the reaction rate. Both a small value of $k_{R,1}$ and a large value of $k_{R,2}$ limit the reaction rate and lead to a flat slope in the temperature profiles. The optimal solution is found above the expected ranges for both parameters with $k_{R,1} = 20.9\ s^{-1}$ and $k_{R,2} = 5.58$. Whereas $k_{R,1} = 20.9\ s^{-1}$ is only slightly above the upper value at 20, $k_{R,2} = 5.58$ is clearly above the range. Stricktly speeking, the surrogate is only valid within the bonds of the input parameter space. Extrapolation comes along with increased uncertainty of the surrogate model. We compared the surrogate model and the DuMu^{x}-model and found satisfying agreement. Thus we omitted the precise procedure to build a new surrogate model based on an extended input parameter space.

At initial states of conversion, $k_{R,2} = 5.58$ hardly affects the reaction rate, as the term $(1 - X)^{k_{R,2}}$ is close to one. Its impact increases with increasing conversion. At medium

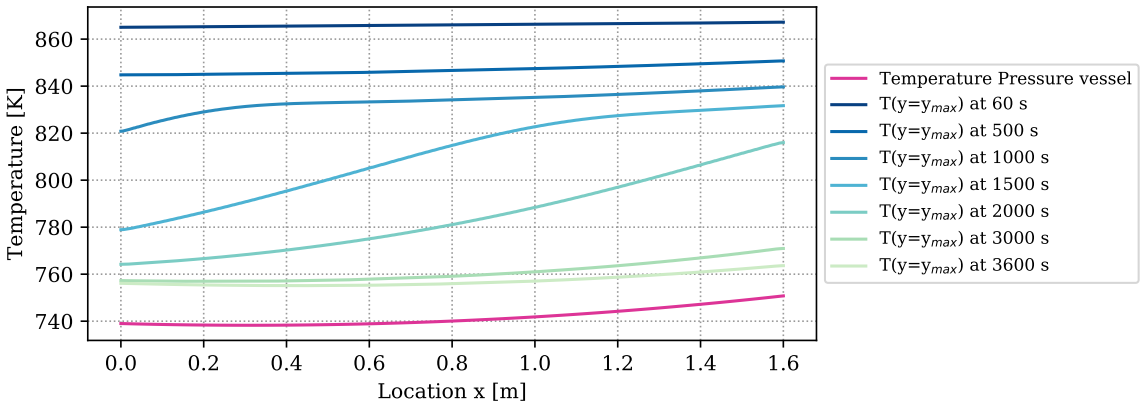

Figure 5.3: Temperature distribution of the outer pressure vessel according to the parameters k_1 - k_3 and at the top boundary of the reactive bed over the reactor length at different times simulated with the DuMu^x-model with the optimized set of parameters of Table 5.5.

conversion, the dampening effect is compensated by the high value of $k_{R,1}$, but at final stages, $k_{R,2}$ dominates the reaction rate. $k_{R,2}$ is responsible for the fact that no complete conversion is achieved within the simulation time.

Experimental results and simulation results agree in this regard as shown in Figure 5.5d. The conversion in the experiment stagnates at 88 % and the maximum conversion of the simulation reaches 95 %. We assigned a large error to the experimental values at final stages in order to not exclude complete conversion. Schmidt et al. [2017] performed 33 cycles of charging and discharging with the same reactor filling. They reach maximal values of conversion between 90 - 95 % for the duration of the experiments and they state that the final 5 - 10 % need significantly more time [Schmidt and Linder, 2017]. Additionally, they detect the formation of agglomerates. In Section 4.4, we showed that the final stages of conversion are retarded, if agglomerates are present in the fixed-bed of a directly operated reactor. The permeability in the surrounding of the agglomerates is larger than in their center. Due to changed pressure gradients, the solid material far from the preferential flow path is less supplied with reaction fluid. In the reactive bed of the indirectly operated reactor concept, pressure gradients are the result of water consumption due to the chemical reaction and thus they are much lesser compared to the directly operated reactor. However, a reduced permeability also deteriorates the fluid flow within the agglomerates in this reactor type. In a self-enhancing mechanism, a smaller pressure gradient deteriorates the supply of water vapor even further and

the reactive solid material in the agglomerates reacts slowly. Same to the directly operated reactor, reactive material with high permeability is converted at first. The retardation effect of the agglomerates becomes noticeable with increasing conversion, when the material close to the preferential flow paths has already reacted. Then, the reduced heat production is overlapped by heat conduction and the slope of the temporal temperature profile is flattened. The term $(1 - X)^{k_{R,2}}$ represents the retardation of the reaction at progressed conversion. This formulation is thus a phenomenological approach to represent the effect of the agglomerates in the model.

The surrogate model represents the conversion profile satisfactorily, see Figure 5.5d. At the beginning, the simulation overestimates the conversion, as the model does not represent the experimental procedure exactly. We used the pressure in the vapor vessel as initial condition in the reactive bed, whereas in the experiment, the reactor had been evacuated beforehand. Thus, an initial water pressure leads to increased conversion at early simulation stages. At later times, experimental and simulation results match well, including the fact that no complete conversion is reached.

Figure 5.5 shows the simulation results of the surrogate model together with the experimental results for the temperature distributions at T1, T3, T7 and the conversion. The results of the calibrated model indicate a good agreement with the experimental data. In particular, the temperature curves T1 and T3 reflect the temperature profile well, including the slope of temperature decrease at final conversion and the final temperature after conversion. The discrepancy in T7 is larger. As the reaction front moves from left to right, this measurement point is less determined by initial and boundary conditions. The surrogate model is built based on the DuMu$^{\text{x}}$-simulations. Thus, the model uncertainties accumulate at this point. This explains furthermore the wavy shape of the surrogate model results for T7. The shape of T1 and T3 is smoother and features a smaller confidence interval especially at later simulation times compared to T7.

Table 5.5: Optimized set of parameters with mean 95 % confidence interval.

Parameter	**Symbol**	**Unit**	**Mean**	**+**	**-**
Heat-transfer coefficient	α_{HTF}	W/m^2K	337	1.30	1.38
Heat-loss coefficient	α_{loss}	W/m^2K	13.2	0.40	0.38
Temperature distribution Param1	k_1	K/m^2	7.54	1.51	1.49
Temperature distribution Param2	k_2	K/m	-4.71	1.34	1.35
Temperature distribution Param3	k_3	K	739	1.39	1.41
Reaction coeffiecient	$k_{R,1}$	s^{-1}	20.9	1.46	1.45
Reaction exponent	$k_{R,2}$	-	5.58	0.26	0.26

5.4.2 Validation

The calibrated surrogate model was used to simulate the experiment Case R20, see Table 5.1, with a similar setup but different water vapor pressure (270e5 Pa) and air volume flux in the HTF channel (47.22 $kg\,m^{-2}\,s^{-1}$). The lower water pressure results in a lower equilibrium temperature and, despite a larger heat-transfer flux, a slower conversion. The experimental data exceed 100 % conversion against the statement of [Schmidt and Linder, 2017], that conversions of maximum 95 % were reached. We attribute this to measurement uncertainty. Figure 5.6 shows the simulation results of the surrogate model.

As outlined in the previous section, the simulation does not reach complete conversion due to the high value of the parameter $k_{R,2}$ that phenomenologically represents the reaction behavior once agglomerates have formed. As the experiment reaches 100 % conversion in 6000 seconds, possibly no agglomerates are present yet. This would be the case, if this experimental run was one of the first in row of the altogether 33 experiments [Schmidt et al., 2017]. The chronological order of the experiments is not mentioned in [Schmidt et al., 2017, Schmidt and Linder, 2017] or [Risthaus et al., 2020]. The parameter $k_{R,2}$ determines the rate of conversion and the temperature profiles unfold accordingly. Experimental data and simulation results of the temperatures T1, T3, and T7 are shown in Figures 5.6a, 5.6b and 5.6c. The profiles show a good agreement with the experimental temperature curves. It is thus conceivable that the experimental data of conversion contain a measurement bias and agglomerates are present.

The model results overestimate the equilibrium temperature of the experiment. The equilibrium condition for pressure and temperature of [Samms and Evans, 1968], which was used for the calibration case, is not adapted to the pressure conditions of the reaction conditions. The simulated temperatures however, are still in the range of measurement uncertainty. Despite that, the temperature profiles of this experimental setup are reproduced with an accuracy comparable to the calibration case. The decrease in temperature is slightly steeper in the model results, but the velocity of the reaction front matches the model results. The final temperatures for each measurement lay within the range of measurement uncertainty.

5.5 Summary and Conclusion

In this chapter, we presented the model concept for simulating the indirectly operated reactor concept. It is composed of two subdomains, one for the reactive bed and one for the HTF channel. Both submodels are coupled by a conductive heat flux. With the aim of calibrating and validating the numerical model, we compared the simulation results to experimental data for the course of temperature at distinct measurement points and the overall conversion for a discharge reaction presented in [Schmidt and Linder, 2017]. In the experiment, the temperature of the reactive bed falls below the temperature imposed in the HTF channel. This is explained by heat losses over the reactor casing to the ambient [Risthaus et al., 2020]. It furthermore turned out that introducing the heat loss is not sufficient to reproduce the experimental temperature profiles with the numerical model. We identified that the reaction rate decreases with increasing conversion. To represent this effect, we enhanced the reaction kinetics by the factor $(1 - X)^{k_{R,2}}$. With the heat-transfer coefficient in the HTF channel, the temperature distribution outside the reactive bed, the heat loss coefficient and two reaction rate constants, we identified altogether seven model parameters that needed to be calibrated for the envisaged simulation setup. We inferred them with the help of Bayesian inversion based on a McMC algorithm. To accelerate the process, we replaced the numerical model by a PCE (polynomial chaos expansion) surrogate model that we trained with 500 simulation runs at varying parameters covering the parameter space. The Bayesian inference delivers a posterior parameter distribution with the mean being the most probable value. All the inferred parameters were Gaussian distributed

in the posterior distribution. Our numerical model is thus sensitive to all of them. The simulation results of the calibrated surrogate model showed a good match with the measurements. A subsequent validation with a similar experiment at different boundary conditions confirms the model for the experimental setup.

From the experimental data on the course of temperature and conversion over the duration of the chemical reaction, we draw the following conclusions:

Additionally to the heat transported in the HTF channel, heat is lost over the reactor surface. As temperatures close to the equilibrium temperature limit the reaction, the heat losses lead to an increased speed of reaction. A temperature difference between the surface of the reactive bed and the casing of the vapor vessel induces a heat transport by a combination of different heat transport processes, notably heat conduction, free convection and radiation. It is beyond our scope to identify the amount of heat loss associated to each mechanism separately. We inferred that with 1.34e3 kJ in total more heat is lost over the reactor surface than transported to the HTF channel (0.90e3 kJ).

Contrary to the statement of Risthaus et al. [2020] that the experimental results can be reproduced by only considering the heat losses happening in the homogeneous reactive bed, we identified that an additional process influences the reaction at progressed conversion. [Schmidt and Linder, 2017] confirm the presence of agglomerates in the experiment. We showed that the agglomerates decelerate the reaction not only in the directly operated reactor setup, but also in the reactive bed of the indirectly operated reactor, as they limit the distribution of the reaction fluid. We represented this effect phenomenologically by enhancing the reaction kinetics by the constant $k_{R,2}$ in the factor $(1 - X)^{k_{R,2}}$. The reduced reaction at progressed conversion permits to reach the equilibrium temperature at the beginning of the reaction and causes a flatter slope of the temperature jump at the end of conversion. Due to the retardation, no complete conversion is reached within the given duration of the experiment. This is confirmed by the experimental data on the course of conversion.

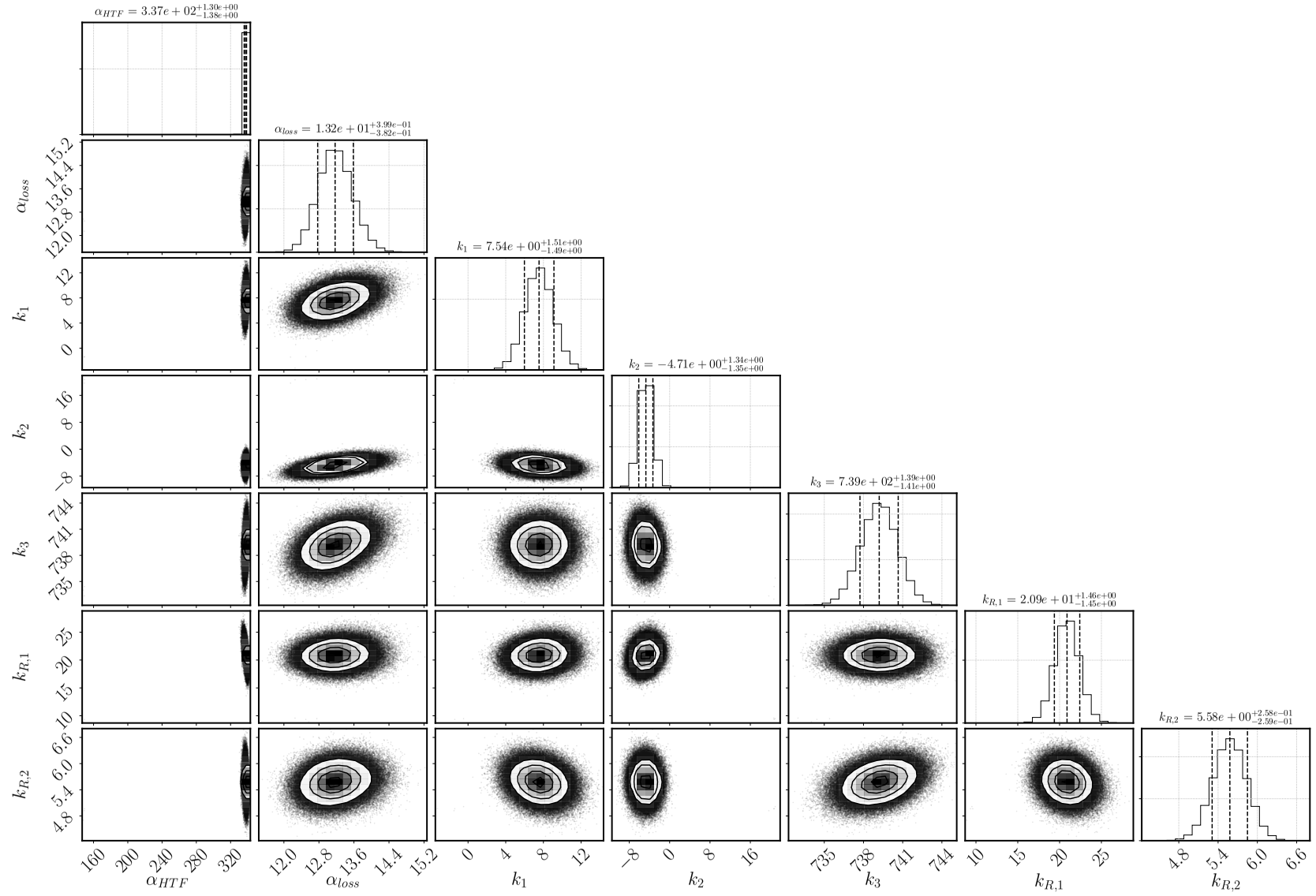

Figure 5.4: Histograms for the parameter distribution after inverse modeling based on experimental data of [Schmidt and Linder, 2017]. On the diagonal are the histograms for the single parameters including mean and 95 % confidence interval (indicated by the dashed lines). The scatter plots show the covariance between the parameters of the respective row and column.

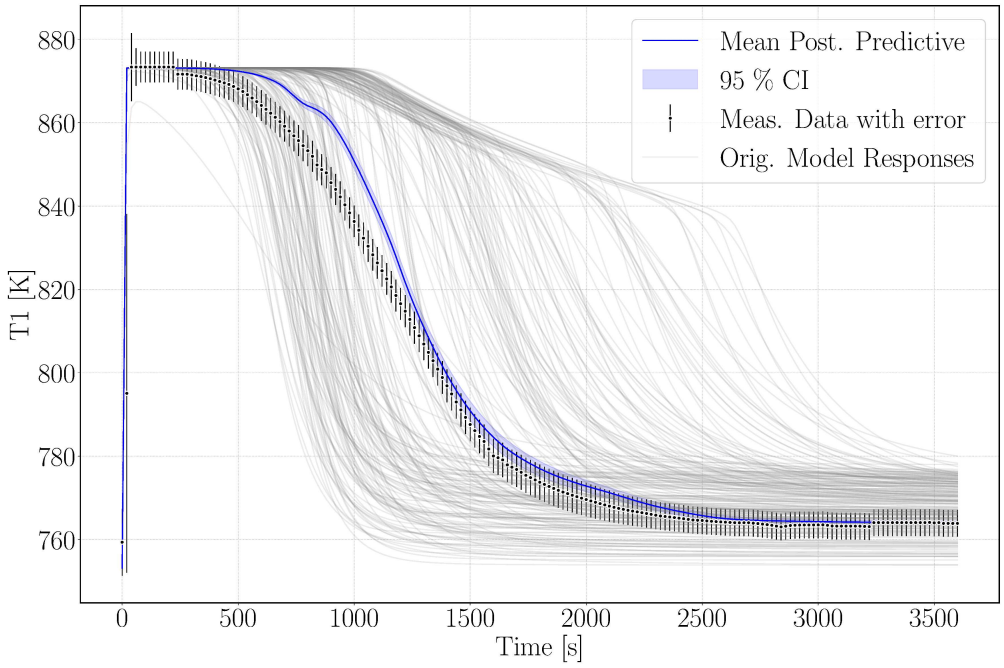

(a) Temperature measurement point T1.

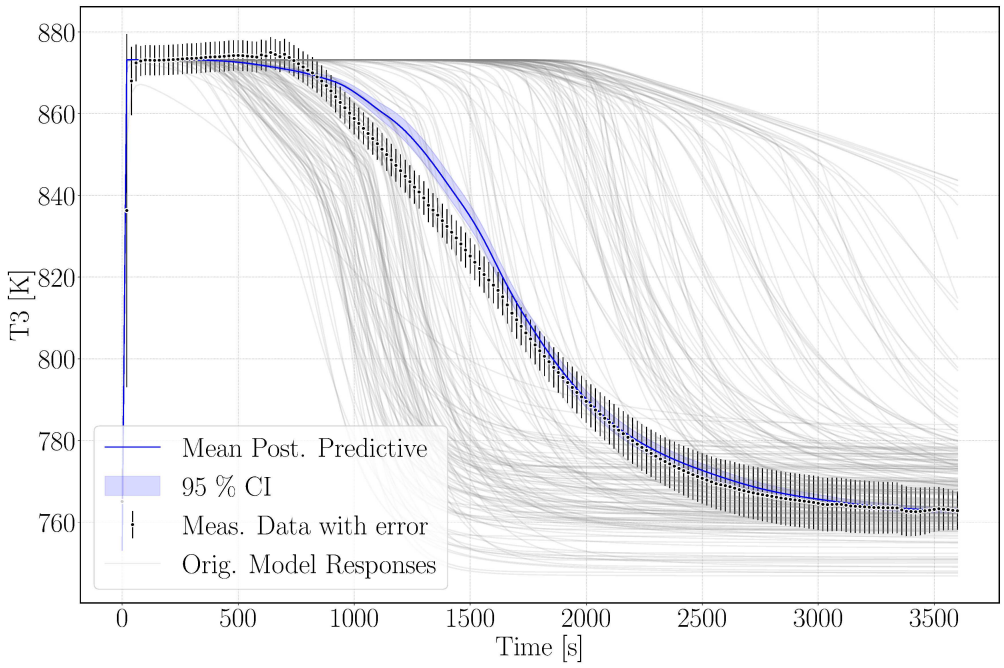

(b) Temperature measurement point T3.

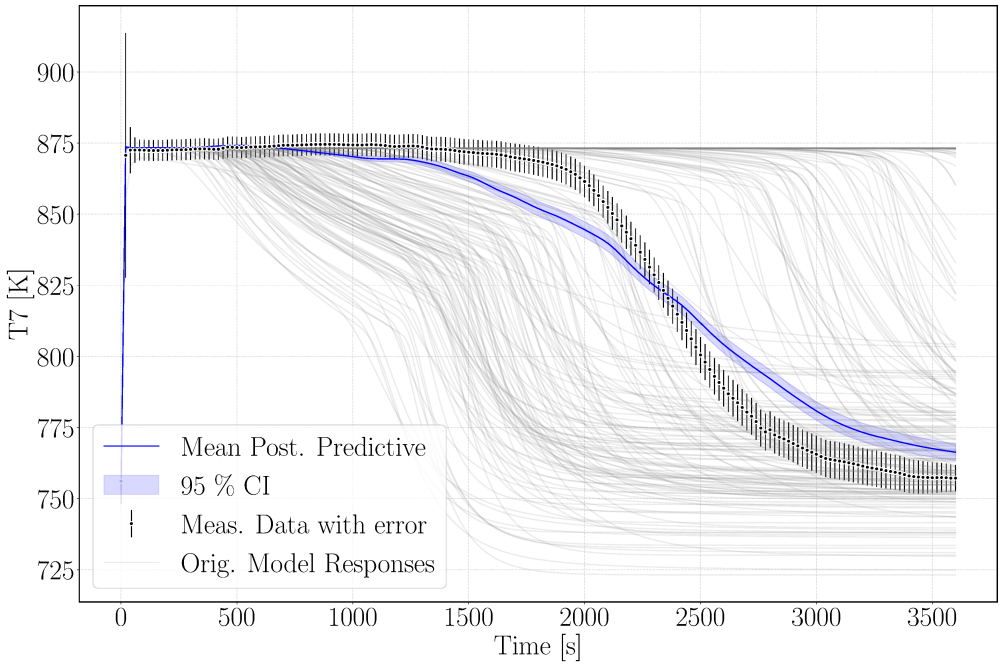

(c) Temperature measurement point T7.

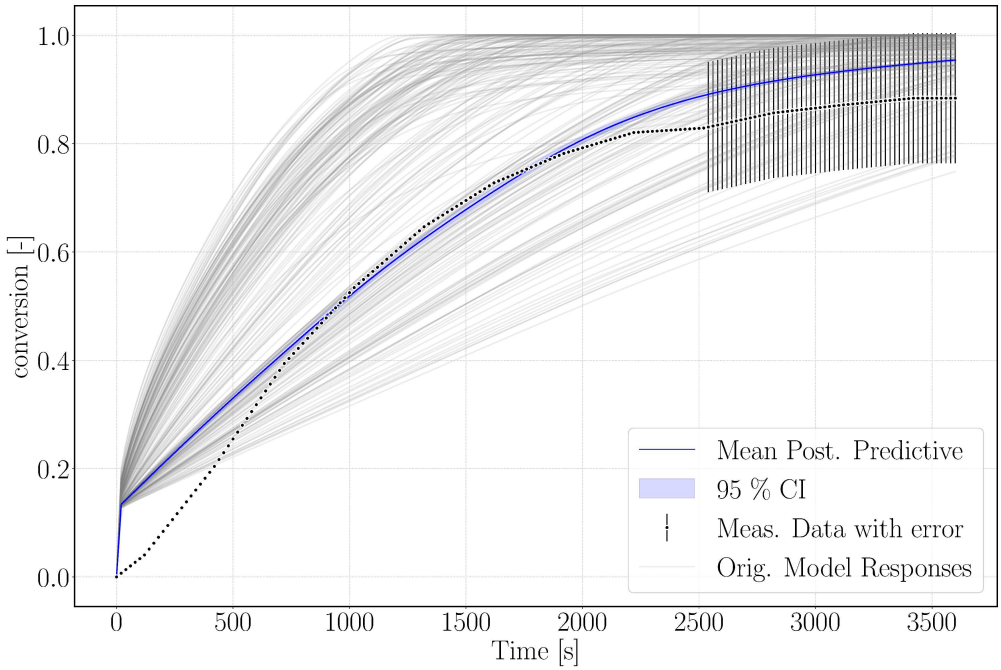

(d) Global conversion

Figure 5.5: Simulation results of the calibrated surrogate model with its 95% confidence interval (CI) for Case S17; the surrogate model is based on 500 simulation runs of the DuMu^x-model plotted in gray. The experimental reference data are plotted in black including error-bars representing the uncertainties.

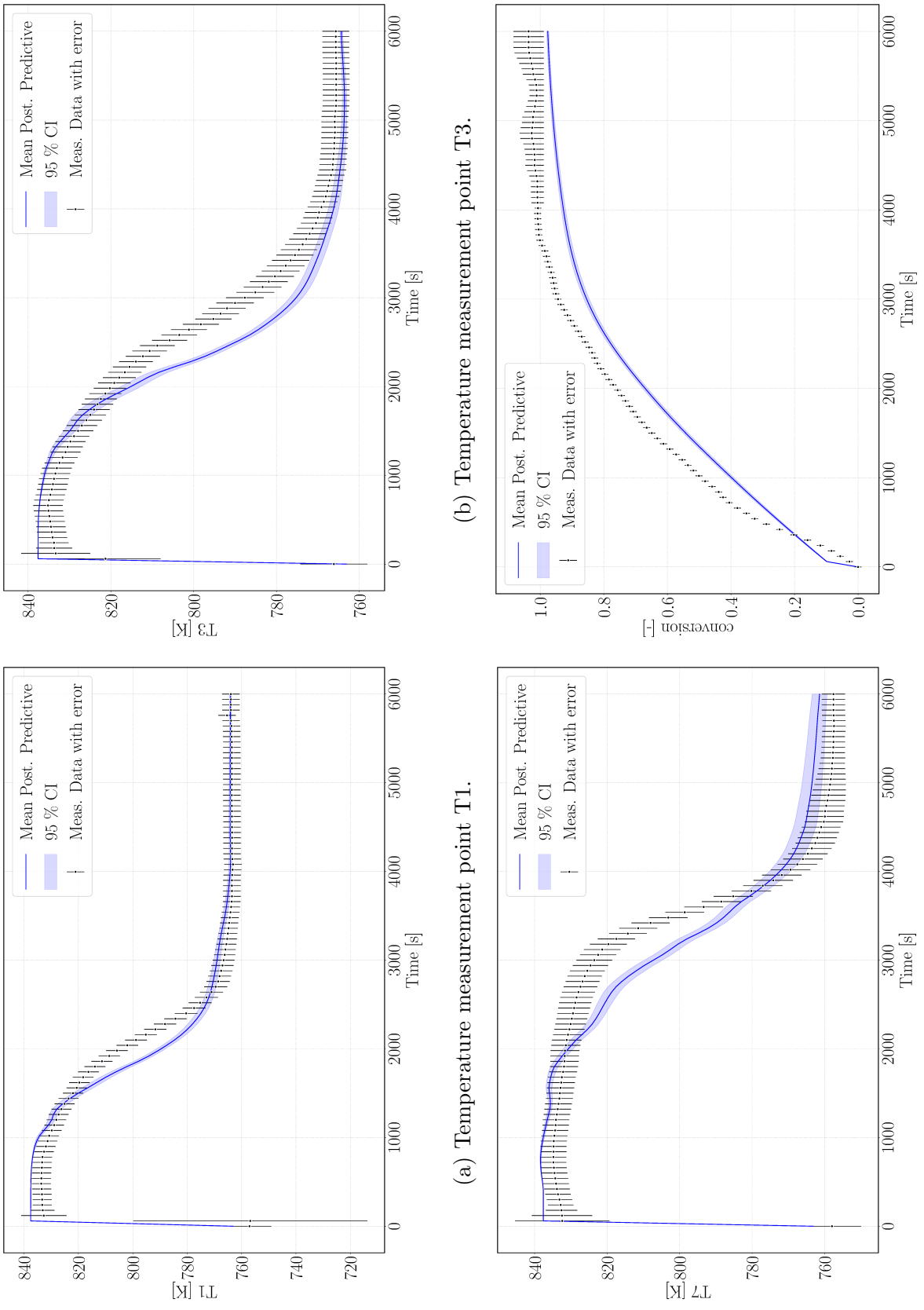

(a) Temperature measurement point T1.

(b) Temperature measurement point T3.

(c) Temperature measurement point T7.

(d) Conversion

Figure 5.6: Simulation results of the calibrated surrogate model with its 95% confidence interval (CI) for Case R20; the experimental reference data are plotted in black including error-bars representing the uncertainties.

6 Finale

This chapter summarizes our key findings in Section 6.1 and outlines on how to continue this work in Section 6.2.

6.1 Summary

To tackle the challenge of climate change, a variety of solutions is necessary to decarbonise the energy production and increase energy efficiencies. Against this background, thermochemical heat storage is a promising technology, as it features high storage densities and the possibility of a loss-free long-term storage. Different reaction systems span a large range of temperature applications. Solid-gas reactions are the most favorable, as the reactive gas can easily be removed from the system to prevent the reverse reaction. However, there is no ready-to-use application of thermochemical heat storage available. Thus, further research is necessary to better understand the relevant processes. We addressed this topic in the present work by numerical modeling of fixed-bed reactors. The reactor forms the environment, where the reaction is controlled by adjusting the conditions of gas pressure and temperature accordingly. In fixed-bed reactors, the solid material usually comes in the form of particles or powders, that are filled in a container. Two different types of fixed-bed reactors are distinguished: (1) In directly operated reactors, a mixture of reactive gas and inert heat-transfer fluid is conducted directly through the fixed bed to provide both heat and reaction fluid. (2) In the indirectly operated reactor, heat and reaction fluid are provided independently. The reactive gas is dosed directly into the reactive bed, whereas the heat is transferred in spatially enclosed heat-transfer channels. Both reactor types have different modeling requirements, what we outlined in this work.

In the numerical model, we approximated the fixed bed by the concept of a porous medium. The rigid solid forms the porous matrix and the reactive gas occupies the pore space. We presented the transport mechanisms for mass, momentum and heat, which occur in the fixed bed of the thermochemical heat storage reactor during reaction. The reaction itself is described by reaction kinetics. Our work focused on the specific reaction system of Calcium oxide (CaO) with water vapor (H_2O) to Calcium hydroxide ($Ca(OH)_2$) under the release of heat. Providing heat shifts the chemical equilibrium to the reverse side of the equation and reverts the reaction. The chemical equilibrium is characterized by the van't Hoff law according to pressure and temperature under the assumption of constant enthalpy and entropy of reaction. The reaction kinetics are usually determined experimentally. This work provided a literature review on existing formulations of the reaction kinetics and pointed out, that there is no common understanding on the reaction mechanism yet. For this reason, the theoretical formulation of [Schmidt, 2011] is used, that does not pretend a high accuracy. The reaction system $CaO/Ca(OH)_2$ undergoes a volume change of 50 % during the reaction. After several cycles of charging and discharging, agglomerates develop as a consequence of the repeated swelling and shrinking of the reactive porous medium. The properties of the initially homogeneous porous medium change.

We represented the reactive system by a set of balance equations. Mass and momentum of each reactive species and the energy of each phase are balanced. The balance equations include the physical formulations of the transport mechanisms and the reaction rate. The system of equations is complex and highly coupled via the reaction rate. Therefore, we approximated them numerically in the simulation toolbox $DuMu^x$, which provides the discretization and solving methods. Furthermore, $DuMu^x$ provides the environment to couple adjacent submodels by coupling fluxes.

In the first step, we presented simulation results for the directly operated reactor concept. The model is verified in a benchmark study together with models based on the software OpenGeoSys and ANSYS fluent. The benchmark setup however, contained several simplifying assumptions. We tested the impact of these simplifications with numerical experiments based on the simulation setup of the benchmark. We obtained the following findings:

- The assumption of thermal equilibrium reduces the set of primary variables, because one temperature variable is then sufficient to describe both solid and gas.

This saves simulation time. The assumption is sufficiently accurate for small particles in the range of 5e-5 m, where a possible temperature difference evens out rapidly.

- The representation of the solid volume change is important for describing the coupled processes in the reactive bed correctly. A change in porosity alters the amount of heat conduction and thus the reaction behavior, which is highly sensitive to the temperature. Moreover, an alternating permeability changes the pressure conditions in the reactor and consequently also influences the reaction rate in the homogeneously filled reactor.

- The presence of agglomerates at the place of the homogeneous bulk is equivalent to the presence of preferential flow paths. They retard the reaction at increasing conversion. We represented the preferential flow paths as discrete fractures in the numerical model, and thereby reproduced the effect of the agglomerates qualitatively.

In the second place, we presented the model concept for the indirectly operated reactor concept. It consists of two submodels: (1) the porous reactive bed and (2) the heat-transfer channel. Both submodels are coupled via a conductive heat flux. In order to validate the model with experimental data, we firstly identified seven important uncertain parameters specific to the experimental setup that needed calibration. They represent the heat transfer between bed and channel, heat losses over the reactor casing and the reaction rate. We determined the uncertain parameters with Bayesian inference. For speeding up the calibration, we substituted the numerical model by a surrogate model. The calibrated parameters reveal that 1.34e3 kJ of in total 2.24e3 kJ are lost over the reactor surface. Furthermore, it is deduced that the reaction rate is retarded at progressing conversion due to an agglomerated reactive bulk. We represent this retardation effect phenomenologically with an additional constant in the reaction kinetics. A subsequent comparison of the model with additional experimental data to the same reactor setup validated our model.

For both types of fixed-bed reactors, the volume change of the reactive solid particles impacts the overall reaction behavior. During the initial cycles of charging and discharging, porosity and permeability influence heat conduction and pressure conditions in the homogeneous bulk. Once agglomerates are formed after a few charging cycles, the reaction is retarded at progressed conversion. We presented two different

approaches to account for this effect: preferential flow paths in the reactive bed and a phenomenological representation via the reaction kinetics to retard the reaction at progressed conversion.

6.2 Outlook

Through numerical experiments and simulations in this work, we gained insight in the importance of several processes occurring in fixed-bed reactors for thermochemical heat storage with the reaction system $CaO/Ca(OH)_2$. However, several processes can't be answered by modeling, but need further experimental substantiation.

We used the reaction kinetics of [Schmidt, 2011], that is based on theoretical considerations. According to [Nagel et al., 2014], this formulation represents the reaction accurately, if the vapor pressure does not limit the reaction. To extend the model to different reaction conditions, a correct formulation of the reaction kinetics is crucial. The reaction mechanism that is independent of the reaction conditions of pressure and temperature, needs to be determined experimentally. This includes the quantification of the history effect due to the reaction temperatures presented by [Yan et al., 2019]. An appropriate reaction kinetics is necessary to simulate the charge reaction especially in the indirectly operated reactor concept. The charge reaction is preferably conducted at low pressures, where the equilibrium temperature is low [Schmidt and Linder, 2017]. Thereby low-level heat can be used. At such conditions, the reaction proceeds slowly and heat conduction does not limit the reaction, contrary to the experimental setups, we presented in this work. Currently, there is no reaction kinetics available, that represents the reaction at low pressures correctly [Risthaus et al., 2020].

The agglomerates fundamentally influence the chemical reaction in a fixed-bed reactor. Schmidt and Linder [2017] assume, that they get formed within the first cycles of charging and discharging. According to [Roßkopf et al., 2015], they are formed after 10 reaction cycles. Schmidt and Linder [2017] assume, that the properties of the bulk stay relatively constant, once the agglomerates are formed. Studying the process of agglomerate formation requires a detailed documentation of several cycles of charging and discharging in a row. [Schaube, 2013] run 25 cycles of charge and discharge in a directly operated reactor. However, they list only the duration until conversion and

no further parameters. We assume, that the formation of agglomerates does not occur homogeneously all over the reactive bed, as it depends on the mechanical stresses due to the load of the overlaying material. Agglomerates at the bottom of the reactor thus might have a higher density, that those located at the top. Thereby, it is important, to monitor the processes in the reactor in a spatially resolved manner. Schaube [2013], Schmidt and Linder [2017] furthermore discovered, that the total bulk volume is smaller after the formation of agglomerates. Modeling the formation of the agglomerates necessitates a mechanical model, that represents the stresses on the particles.

Modeling can assist the experimental work by providing methods for optimal design of experiments, see e.g. [Pukelsheim, 2006]. With the possibility of inverse modeling, it offers a method to deduce parameters that are difficult to obtain with measurements.

The numerical model presented in this work can be easily transferred to other reaction systems, by exchanging the material related properties. Promising material systems with a good experimental background are $SrBr_2/SrBr_2 \cdot 6H_2O$ [Michel et al., 2012, Stengler et al., 2017, Stengler and Linder, 2020] and $MgSO_4/MgSO_4 \cdot 7H_2O$ [Van Essen et al., 2009].

A Appendix

A.1 Knudsen Diffusion Flux

Different experimental setups for thermochemical heat storage will deal with Kn numbers up to 0.5. In order to cover all the different regimes, Yuan et al. [2016] present a correction factor for the permeability dependent on the Knudsen-number:

$$\mathbf{K}_{\mathrm{Kn}} = f(\mathrm{Kn})\mathbf{K} \tag{A.1}$$

with $\mathbf{K}_{\mathrm{Kn}}$ the apparent gas permeability, $f(\mathrm{Kn})$ the Knudsen correction factor, $\mathbf{K}$ the equivalent permeability. [Beskok and Karniadakis, 1999] and [Yuan et al., 2016] present the following correction factor

$$f(\mathrm{Kn}) = [1 + \alpha(\mathrm{Kn}) \cdot \mathrm{Kn}] \left[1 + \frac{4\mathrm{Kn}}{1 - b\mathrm{Kn}}\right] \tag{A.2}$$

with the rarefaction coefficient α

$$\alpha(\mathrm{Kn}) = \frac{128}{15\pi^2}\tan^{-1}(4.0\mathrm{Kn}^{0.4}) \tag{A.3}$$

and the slip coefficient $b = -1$.

A.2 Derivation of the Energy Balance Equations

The total energy of a system E takes (additionally to the internal energy U) the kinetic and the potential contribution into account.

$$E = U + m\frac{\mathbf{v^2}}{2} + m\Psi, \tag{A.4}$$

with Ψ, the potential. Our system of lab-scale thermochemmical heat-storage reactors, however, does not change its position in the gravitational field of the earth and thus, we neglect the potential term Ψ. Furthermore, the fluid velocity in the porous medium is very small and the solid doesn't move at all, so that we furthermore neglect the kinetic energy contribution $m\frac{\mathbf{v^2}}{2}$.

The change in internal energy U equals the sum of heat Q or Work W added to the system, see Equation 2.15.

We consider only normal stresses in the work performed by the fluid:

$$\frac{dW}{dt} = \int_V \nabla \cdot (\sigma \mathbf{v}) dV = -\int_V \nabla \cdot (p \cdot \underline{\mathrm{I}}\mathbf{v}) dV \tag{A.5}$$

The shear stresses are already described phenomenologically by the fluid viscosity (see Equation 2.7)

We consider heat conduction between the sytem and its environment as well as heat sources, q^e, resulting e.g. from a chemical reaction.

$$\frac{dQ}{dt} = \oint_A \lambda \cdot \nabla T dA + \int_V q^e dV = \int_V \nabla \cdot (\lambda \nabla T)\, dV + \int_V q^e dV \tag{A.6}$$

With λ the heat conduction. The Green-Gauss-theorem is applied to arrive at the second part of equation A.6.

The total derivative of the energy U is described by the Reynold's Transport Theorem (see e.g. [Helmig et al., 1997]) as follows:

$$\frac{dU}{dt} = \int_V \frac{\partial}{\partial t}(u\rho) dV + \oint_A u\rho(\mathbf{v} \cdot \mathbf{n}) dA = \int_V \frac{\partial}{\partial t}(u\rho) dV + \int_V \nabla \cdot (u\rho \mathbf{v}) dV \tag{A.7}$$

Again the Green-Gauss-Theorem was applied to transform the surface integral to a volume integral in the second part of the equation.

Inserting Equations A.5, A.6 and A.7 into Equation 2.15 yields

$$\int_V \frac{\partial}{\partial t}(u\rho)dV + \int_V \nabla\cdot(u\rho\mathbf{v})dV = -\int_V \nabla\cdot(p\mathbf{v})dV + \int_V \nabla\cdot(\lambda\nabla T)dV + \int_V q^e dV \quad \text{(A.8)}$$

Differentiating and rearranging the terms yields:

$$\frac{\partial}{\partial t}(u\rho) + \nabla\cdot(u\rho\mathbf{v} + p\mathbf{v} - \lambda\nabla T) = q^e \quad \text{(A.9)}$$

We take the definition of the enthalpy (see 2.17 and $h = u + p/\rho$ for the intensive quantity) into account. This yields the energy balance of one phase α:

$$\frac{\partial}{\partial t}u_\alpha\rho_\alpha + \nabla\cdot[\rho\mathbf{v}h_\alpha - \lambda_\alpha\nabla T] = q^e_\alpha \quad \text{(A.10)}$$

In the porous, reactive bed, there is at least one solid phase $\alpha = s$ and a fluid phase $\alpha = g$. The fluid phase occupies the volume fraction ϕ (i.e. the porosity) whereas the solid phase is present in the rest of the considered volume $(1-\phi)$. We account for heat transfer between the phases with $f(a_{ws}, T_s, T_f, Nu)$. The energy balance equations for the two phases result in:

$$\frac{\partial}{\partial t}\phi\rho_g u_g + \nabla\cdot\phi\left[\rho_g\mathbf{v}_g h_g - \lambda_g\nabla T_g\right] = \underbrace{f(a_{ws}, T_s, T_f, Nu)}_{\dot{e}_{gs}} + q^e_g, \quad \text{(A.11)}$$

$$\frac{\partial}{\partial t}(1-\phi)\rho_s u_s + \nabla\cdot(1-\phi)\left[\rho_s\mathbf{v}_s h_s - \lambda_s\nabla T_s\right] = \underbrace{f(a_{ws}, T_s, T_f, Nu)}_{\dot{e}_{sg}} + q^e_s. \quad \text{(A.12)}$$

We substitute the velocity of the gas phase by the Darcy velocity as follows: $\mathbf{v} = \phi\mathbf{v}_g$. The solid phase is considered immobile, thus $\mathbf{v}_s = 0$. Given ϕ and ρ_s are temperature independent, the partial derivative of the solid internal energy u_s with respect to the temperature is subsituted by the solid heat capacity.

$$\rho_s(1-\phi)\frac{\partial u_s}{\partial T}\frac{\partial T}{\partial t} = \rho_s(1-\phi)c_{ps}\frac{\partial T}{\partial t} \quad \text{(A.13)}$$

Thus, Equation A.14 results in:

$$\rho_s(1-\phi)c_{ps}\frac{\partial T}{\partial t} - \nabla\cdot(1-\phi)\,\lambda_s\nabla T_s = \underbrace{f(a_{ws}, T_s, T_f, Nu)}_{\dot{e}_{sg}} + q_s^e. \tag{A.14}$$

If the difference between the temperatures of solid and gas is small, we assume local thermal equilibrium, $T = T_g = T_s$ and the heat transfer amounts to zero.

With this assumption, the Equations A.11 and A.14 are added to the following overall energy balance equation at local thermal equilibrium:

$$\frac{\partial}{\partial t}(\phi\rho_g u_g) + \frac{\partial}{\partial t}((1-\phi)\rho_s u_s) + \nabla\cdot[\rho_g \mathbf{v} h_g] - \nabla\cdot(\phi\lambda_g\nabla T) - \nabla\cdot(1-\phi)(\lambda_s\nabla T) = q^e \tag{A.15}$$

The heat conductivities are summarzied to the effective conductivity, see Equation 2.44. Thus, Equation A.16 results in:

$$\frac{\partial}{\partial t}(\phi\rho_g u_g) + (1-\phi)\rho_s c_{ps}\frac{\partial T}{\partial t} + \nabla\cdot[\rho_g \mathbf{v} h_g] - \nabla\cdot(1-\phi)(\lambda_{eff}\nabla T) = q^e \tag{A.16}$$

A.3 Software

Table A.1: The simulation results are produced with the code available in the respective DuMu^x-pub-module. The DuMu^x-version is furthermore indicated in each module.

Section	pub-module	DuMu^x version
Section 4.1	https://git.iws.uni-stuttgart.de/dumux-pub/seitz2017a	3.0
Section 4.2	https://git.iws.uni-stuttgart.de/dumux-pub/seitz2020a	3.2
Section 4.3	https://git.iws.uni-stuttgart.de/dumux-pub/seitz2019a	3.0
Section 4.4	https://git.iws.uni-stuttgart.de/dumux-pub/seitz2020a	3.2
Chapter 5	https://git.iws.uni-stuttgart.de/dumux-pub/seitz2020b	3.2

A.4 Parameter Space for Inverse Modeling

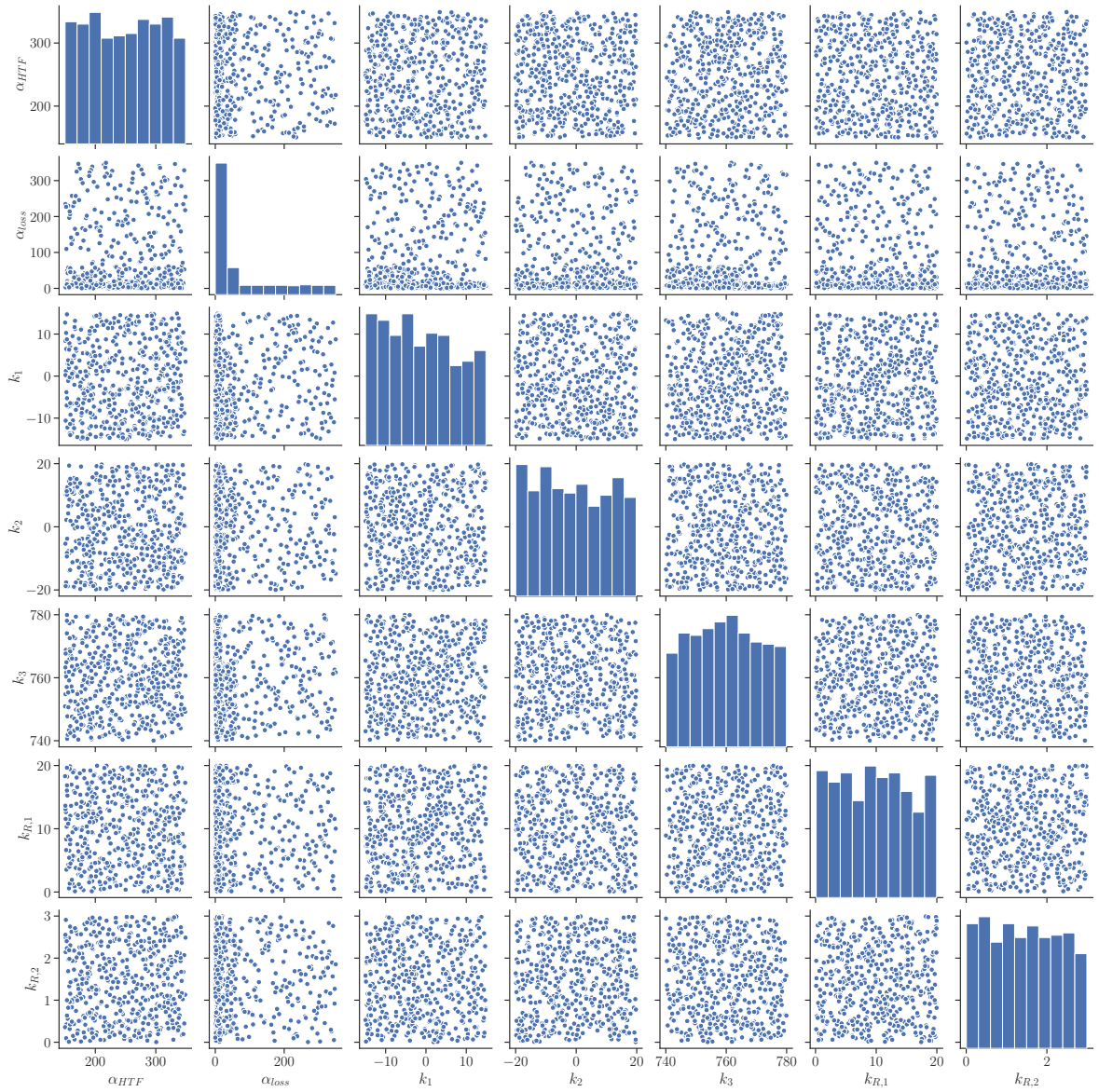

Figure A.1: Input parameter space for inverse modeling; For each point in the scatter plots, the DuMu^x -model was run in order to create a training set for the surrogate model. As the parameters are correlated, the parameters are not equally distributed in order to create a better output space.

Bibliography

I. Aavatsmark, G. Eigestad, B. Mallison, and J. Nordbotten. A compact multipoint flux approximation method with improved robustness. *Numerical Methods for Partial Differential Equations: An International Journal*, 24(5):1329–1360, 2008.

Y. Alvarez Criado, M. Alonso, and J. C. Abanades. Composite material for thermochemical energy storage using cao/ca (oh) 2. *Industrial & Engineering Chemistry Research*, 54(38):9314–9327, 2015.

M. Angerer, M. Becker, S. Härzschel, K. Kröper, S. Gleis, A. Vandersickel, and H. Spliethoff. Design of a MW-scale thermo-chemical energy storage reactor. *Energy Reports*, 4:507–519, 2018.

P. W. Atkins and J. De Paula, editors. *Atkins' physical chemistry*. Oxford Univ. Press, Oxford, 10. ed. edition, 2014. ISBN 978-0-19-969740-3.

D. Aydin, S. P. Casey, and S. Riffat. The latest advancements on thermochemical heat storage systems. *Renewable and Sustainable Energy Reviews*, 41:356 – 367, 2015. ISSN 1364-0321. doi: https://doi.org/10.1016/j.rser.2014.08.054.

I. Barin, editor. *Ag-Kr*, volume 1 of *Thermochemical data of pure substances 1*. VCH, Weinheim; Basel, 3. ed. edition, 1995.

P. Bastian, M. Blatt, A. Dedner, C. Engwer, R. Klöfkorn, R. Kornhuber, M. Ohlberger, and O. Sander. A generic grid interface for parallel and adaptive scientific computing. Part II: Implementation and tests in DUNE. *Computing*, 82:121–138, 01 2008a. doi: 10.1007/s00607-008-0004-9.

P. Bastian, M. Blatt, A. Dedner, C. Engwer, R. Klöfkorn, M. Ohlberger, and O. Sander. A generic grid interface for parallel and adaptive scientific com-

puting. Part I: Abstract framework. *Computing*, 82:103–119, 07 2008b. doi: 10.1007/s00607-008-0003-x.

T. Bauer, W.-D. Steinmann, D. Laing, and R. Tamme. Thermal energy storage materials and systems. *Annual Review of Heat Transfer*, 15, 2012.

J. Bear. *Modeling phenomena of flow and transport in porous media*, volume 31 of *Springer eBook Collection. Earth and Environmental Science*. Springer, 2018. ISBN 9783319728261.

Y. Bernabé, U. Mok, and B. Evans. Permeability-porosity relationships in rocks subjected to various evolution processes. *Pure and Applied Geophysics*, 160(5-6):937–960, 2003.

I. Berre, F. Doster, and E. Keilegavlen. Flow in fractured porous media: A review of conceptual models and discretization approaches. *Transport in Porous Media*, 130 (1):215–236, 2019.

J. Bertsch, C. Growitsch, S. Lorenczik, and S. Nagl. Flexibility in Europe's power sector — An additional requirement or an automatic complement? *Energy Economics*, 53: 118 – 131, 2016. doi: https://doi.org/10.1016/j.eneco.2014.10.022. Energy Markets.

A. Beskok and G. Karniadakis. A model for flows in channels, pipes, and ducts at micro and nano scales. *Microscale Thermophysical Engineering*, 3, 02 1999. doi: 10.1080/108939599199864.

M. Blatt, A. Burchardt, A. Dedner, C. Engwer, J. Fahlke, B. Flemisch, C. Gersbacher, C. Gräser, F. Gruber, C. Grüninger, D. Kempf, R. Klöfkorn, T. Malkmus, S. Müthing, M. Nolte, M. Piatkowski, and O. Sander. The distributed and unified numerics environment, version 2.4, Dec. 2016.

BMWi. Energieeffizienz in Zahlen - Entwicklungen und Trends in Deutschland 2019. Technical report, Bundesministerium für Wirtschaft und Energie, Berlin, 2019. https://www.bmwi.de/Redaktion/DE/Publikationen/Energie.

BP p.l.c. Statistical Review of World Energy 2020 - 69th edition, 2020. URL `https://www.bp.com/en/global/corporate/energy-economics/statistical-review-of-world-energy.html`.

P. Carman. Fluid flow through granular beds. *Chemical Engineering Research and Design*, 75:S32 – S48, 1997. doi: https://doi.org/10.1016/S0263-8762(97)80003-2.

J. Carrayrou, J. Hoffmann, P. Knabner, S. Kräutle, C. Dieuleveult, J. Erhel, J. Lee, V. Lagneau, K. Mayer, and K. Macquarrie. Comparison of numerical methods for simulating strongly nonlinear and heterogeneous reactive transport problems—the momas benchmark case. *Computational Geosciences*, 14, 06 2010. doi: 10.1007/s10596-010-9178-2.

A. J. Carrillo, J. Gonzalez-Aguilar, M. Romero, and J. M. Coronado. Solar energy on demand: A review on high temperature thermochemical heat storage systems and materials. *Chemical reviews*, 119(7):4777–4816, 2019.

E. Coltman, S. Ackermann, B. Becker, M. Blatt, S. Burbulla, H. Class, S. Emmert, B. Flemisch, D. Gläser, C. Grüninger, K. Heck, J. Hommel, T. Jupe, T. Koch, T. Kurz, M. Lipp, F. Mohammadi, M. Schneider, G. Seitz, L. Stadler, M. Utz, M. Veyskarami, F. Weinhardt, K. Weishaupt, and R. Winter. Dumux 3.2.0, May 2020.

J. R. Cooper and R. B. Dooley. Release of the IAPWS formulation 2008 for the viscosity of ordinary water substance, 2008.

J. Cot-Gores, A. Castell, and L. F. Cabeza. Thermochemical energy storage and conversion: A-state-of-the-art review of the experimental research under practical conditions. *Renewable and Sustainable Energy Reviews*, 16(7):5207 – 5224, 2012. doi: https://doi.org/10.1016/j.rser.2012.04.007.

Y. A. Criado, M. Alonso, and J. C. Abanades. Kinetics of the CaO/Ca(OH)2 hydration/dehydration reaction for thermochemical energy storage applications. *Industrial & Engineering Chemistry Research*, 53(32):12594–12601, 2014.

T. A. Davis. Umfpack user guide, 10 2019. URL `http://www.suitesparse.com`.

M. A. Delucchi and M. Z. Jacobson. Providing all global energy with wind, water, and solar power, Part II: Reliability, system and transmission costs, and policies. *Energy Policy*, 39(3):1170 – 1190, 2011. doi: https://doi.org/10.1016/j.enpol.2010.11.045.

I. Dincer and M. Ezan. *Heat Storage: A Unique Solution For Energy Systems*. Springer Berlin Heidelberg, 10 2018. ISBN 978-3-319-91893-8. doi: 10.1007/978-3-319-91893-8.

O. Edenhofer, R. Pichs-Madruga, Y. Sokona, E. Farahani, S. Kadner, K. Seyboth, A. Adler, I. Baum, S. Brunner, P. Eickemeier, B. Kriemann, J. Savolainen, S. Schlömer, C. von Stechow, T. Zwickel, and J. Minx, editors. *Summary for Policymakers*, pages 1–33. In Press, Genf, Switzerland, 2014. URL `https://www.ipcc.ch/site/assets/uploads/2018/02/ipcc_wg3_ar5_summary-for-policymakers.pdf`.

W. Ehlers. Foundations of multiphasic and porous materials. In *Porous media*, pages 3–86. Springer, 2002.

S. Ergun and A. A. Orning. Fluid flow through randomly packed columns and fluidized beds. *Industrial & Engineering Chemistry*, 41(6):1179–1184, 1949.

M. Felderhoff, R. Urbanczyk, and S. Peil. Thermochemical heat storage for high temperature applications–a review. *Green*, 3(2):113–123, 2013.

D. Foreman-Mackey, D. W. Hogg, D. Lang, and J. Goodman. emcee: The MCMC Hammer. *American Scientific Publishers*, 125(925):306, Mar. 2013. doi: 10.1086/670067.

D. Foreman-Mackey, W. M. Farr, M. Sinha, A. M. Archibald, D. W. Hogg, J. S. Sanders, J. Zuntz, P. K. Williams, A. R. Nelson, M. de Val-Borro, et al. emcee v3: A python ensemble sampling toolkit for affine-invariant mcmc. *arXiv preprint arXiv:1911.07688*, 2019.

S. Funayama, H. Takasu, M. Zamengo, J. Kariya, S. T. Kim, and Y. Kato. Performance of thermochemical energy storage of a packed bed of calcium hydroxide pellets. *Energy Storage*, 1(2):e40, 2019. doi: 10.1002/est2.40.

U. W. Gedde. Essential Classical Thermodynamics, 2020.

A. Gelman, G. Roberts, and W. Gilks. Bayesian statistics 5. *Oxford University Press*, 16:17, 1996.

C. Geuzaine and J.-F. Remacle. Gmsh: A 3-D finite element mesh generator with built-in pre- and post-processing facilities. *International Journal for Numerical Methods in Engineering*, 79(11):1309–1331, Sept. 2009. doi: 10.1002/nme.2579.

D. Gläser, B. Flemisch, H. Class, and R. Helmig. Frackit: a framework for stochastic fracture network generation and analysis. *Journal of Open Source Software*, 5(56): 2291, 2020a. doi: 10.21105/joss.02291.

D. Gläser, M. Schneider, B. Flemisch, and R. Helmig. Comparison of cell- and vertex-centered finite-volume schemes for flow in fractured porous media, 2020b.

V. Gnielinski. Heat transfer in concentric annular and parallel plate ducts. VDI Heat Atlas, chapter G1, pages 701 – 708. Springer Berlin Heidelberg, Berlin, Heidelberg, 2010. ISBN 978-3-540-77877-6.

M. Gollsch, B. Priggemeier, and M. Linder. Experimental investigation of gas transport in bulk materials for thermochemical storage. In *7th International Conference on Porous Media*, Mai 2015. URL `https://elib.dlr.de/96496/`.

M. Gollsch, S. Afflerbach, B. Angadi, and M. Linder. Investigation of calcium hydroxide powder for thermochemical storage modified with nanostructured flow agents. *Solar Energy*, 201:810–818, 05 2020. doi: 10.1016/j.solener.2020.03.033.

J. Goodman. Acor, statistical analysis of a time series, 2009.

J. Goodman and J. Weare. Ensemble samplers with affine invariance. *Communications in applied mathematics and computational science*, 5(1):65–80, 2010.

W. M. H. Haynes, editor. *2010 - 2011*, volume 91 (2010) of *CRC handbook of chemistry and physics : a ready-reference book of chemical and physical data*. CRC, Boca Raton, Fla., 91. ed. edition, 2010. ISBN 978-1-4398-2077-3. Previous ed.: 2009. - Includes bibliographical references and index.

R. Helmig et al. *Multiphase flow and transport processes in the subsurface: a contribution to the modeling of hydrosystems.* Springer-Verlag, 1997.

D. Higdon, J. Gattiker, B. Williams, and M. Rightley. Computer model calibration using high-dimensional output. *Journal of the American Statistical Association*, 103 (482):570–583, 2008.

J. Hommel, E. Coltman, and H. Class. Porosity–permeability relations for evolving pore space: A review with a focus on (bio-)geochemically altered porous media. *Transport in Porous Media*, 124(2):589–629, Sep 2018. doi: 10.1007/s11242-018-1086-2.

IAPWS. Revised Release on the IAPWS Industrial Formulation 1997 for the Thermodynamic Properties of Water and Steam, 1997. URL http://www.iapws.org/IF97-Rev.pdf.

IAPWS. Revised Release on the IAPS Formulation 1985 for the Viscosity of Ordinary Water Substance. http://www.iapws.org/, 2003.

IAPWS. Release on the IAPWS Formulation 2011 for the Thermal Conductivity of Ordinary Water Substance. Technical Report IAPWS R15-11, The International Association for the Properties of Water and Steam, Plzeň, Czech Republic, 2011.

IEA. Global CO2 emissions in 2019, 2 2020. URL https://www.iea.org/articles/global-co2-emissions-in-2019.

F. P. V. Incropera, editor. *Foundations of heat transfer*. Wiley, Hoboken, NJ, 6. ed., internat. student version edition, 2013. ISBN 978-0-470-64616-8.

IPCC, editor. *Summary for Policymakers*, page 32 pp. In Press, Genf, Switzerland, 2018. URL https://www.ipcc.ch/site/assets/uploads/sites/2/2019/05/SR15_SPM_version_report_HR.pdf.

A. Irabien, J. R. Viguri, and I. Ortiz. Thermal dehydration of Calcium hydroxide. 1. Kinetic model and parameters. *Industrial & Engineering Chemistry Research*, 29(8): 1599–1606, 1990. doi: 10.1021/ie00104a004.

H. Kerskes, F. Bertsch, B. Mette, A. Wörner, and F. Schaube. Thermochemische Energiespeicher. *Chemie Ingenieur Technik*, 83(11):2014–2026, 2011. doi: 10.1002/cite.201100091.

H. Kerskes, B. Mette, F. Bertsch, S. Asenbeck, and H. Drück. Chemical energy storage using reversible solid/gas-reactions (CWS) – results of the research project. *Energy Procedia*, 30:294 – 304, 2012. ISSN 1876-6102. doi: https://doi.org/10.1016/j.egypro.2012.11.035. 1st International Conference on Solar Heating and Coolingfor Buildings and Industry (SHC 2012).

M. Khachani, A. El Hamidi, M. Halim, and S. Arsalane. Non-isothermal kinetic and thermodynamic studies of the dehydroxylation process of synthetic calcium hydroxide ca(oh) 2. *Journal of Materials and Environmental Science*, 5:615–624, 01 2014.

S. Kjelstrup, D. Bedeaux, E. Johannessen, and J. Groß. *Non-equilibrium thermodynamics for engineers*. World Scientific, New Jersey [u.a.], 2010. ISBN 9789814322157.

H. Kobus, G. Schäfer, K. Spitz, and M. Herr. Dispersive transportprozesse und ihre modellierung. 1992.

T. Koch, D. Gläser, K. Weishaupt, S. Ackermann, M. Beck, B. Becker, S. Burbulla, H. Class, E. Coltman, S. Emmert, T. Fetzer, C. Grüninger, K. Heck, J. Hommel, T. Kurz, M. Lipp, F. Mohammadi, S. Scherrer, M. Schneider, G. Seitz, L. Stadler, M. Utz, F. Weinhardt, and B. Flemisch. Dumux 3 – an open-source simulator for solving flow and transport problems in porous media with a focus on model coupling. *Computers & Mathematics with Applications*, 2020. ISSN 0898-1221. doi: https://doi.org/10.1016/j.camwa.2020.02.012.

F. Kuznik, K. Johannes, C. Obrecht, and D. David. A review on recent developments in physisorption thermal energy storage for building applications. *Renewable and Sustainable Energy Reviews*, 94:576 – 586, 2018. ISSN 1364-0321. doi: https://doi.org/10.1016/j.rser.2018.06.038.

B. Köhler, J. Dengler, A. Dinkel, M. Azam, D. Kalz, P. Bonato, F. Tobias, J. Steinbach, M. Ragwitz, M. Arens, A. Aydemir, R. Elsland, C. Frassine, A. Herbst, S. Hirzel, M. Krail, M. Reuter, F. Toro, M. Rehfeldt, and M. Jakob. Mapping and analyses of the current and future (2020-2030) heating/cooling fuel deployment (fossil/renewables). Technical report, 09 2016.

Y. Le Gallo, O. Bildstein, and E. Brosse. Coupled reaction-flow modeling of diagenetic changes in reservoir permeability, porosity and mineral compositions. *Journal of Hydrology*, 209(1-4):366–388, 1998.

S. Lin, M. Harada, Y. Suzuki, and H. Hatano. CaO Hydration Rate at High Temperature (∼1023 K). *Energy & Fuels*, 20(3):903–908, 2006. doi: 10.1021/ef050257o.

M. Linder. Using thermochemical reactions in thermal energy storage systems. In *Advances in Thermal Energy Storage Systems*, pages 357–374. Elsevier, 2015.

M. Linder, C. Roßkopf, M. Schmidt, and A. Wörner. Thermochemical Energy Storage in kW-scale based on CaO/Ca(OH)2. volume 49, 01 2013. doi: 10.1016/j.egypro.2014.03.096.

P. Linstrom and W. Mallard. NIST Standard Reference Database Number 69.

H.-B. Lu, N. Mazet, and B. Spinner. Modelling of gas-solid reaction—coupling of heat and mass transfer with chemical reaction. *Chemical Engineering Science*, 51(15):3829 – 3845, 1996. ISSN 0009-2509. doi: https://doi.org/10.1016/0009-2509(96)00010-3.

A. Malley-Ernewein and S. Lorente. Constructal design of thermochemical energy storage. *International Journal of Heat and Mass Transfer*, 130:1299 – 1306, 2019. doi: https://doi.org/10.1016/j.ijheatmasstransfer.2018.10.097.

M. Manguoglu and V. Mehrmann. A robust iterative scheme for symmetric indefinite systems. *SIAM Journal on Scientific Computing*, 41(3):A1733–A1752, 2019.

B. Metz, O. Davidson, P. Bosch, R. Dave, and L. Meyer, editors. *Summary for Policymakers*, page 32 pp. Cambridge University Press, Cambridge, United Kingdom and New York, NY, USA., 2007. URL `https://www.ipcc.ch/site/assets/uploads/sites/2/2019/05/SR15_SPM_version_report_HR.pdf`.

D. Mewes and F. Mayinger, editors. *Introduction*, pages 1–19. Springer Berlin Heidelberg, Berlin, Heidelberg, 2005. ISBN 978-3-540-27230-4. doi: 10.1007/3-540-27230-5_1.

B. Michel, N. Mazet, S. Mauran, D. Stitou, and J. Xu. Thermochemical process for seasonal storage of solar energy: characterization and modeling of a high density reactive bed. *Energy*, 47(1):553–563, 2012.

B. Michel, P. Neveu, and N. Mazet. Comparison of closed and open thermochemical processes, for long-term thermal energy storage applications. *Energy*, 72:702 – 716, 2014. ISSN 0360-5442. doi: https://doi.org/10.1016/j.energy.2014.05.097.

R. J. Millington and J. P. Quirk. Permeability of porous solids. *Trans. Faraday Soc.*, 57:1200–1207, 1961. doi: 10.1039/TF9615701200.

E. M. Mokheimer. Performance of annular fins with different profiles subject to variable heat transfer coefficient. *International Journal of Heat and Mass Transfer*, 45(17):3631 – 3642, 2002. ISSN 0017-9310. doi: https://doi.org/10.1016/S0017-9310(02)00078-9.

T. Nagel, H. Shao, A. Singh, N. Watanabe, C. Roßkopf, M. Linder, A. Wörner, and O. Kolditz. Non-equilibrium thermochemical heat storage in porous media: Part 1–conceptual model. *Energy*, 60:254–270, 2013.

T. Nagel, H. Shao, C. Roßkopf, M. Linder, A. Wörner, and O. Kolditz. The influence of gas–solid reaction kinetics in models of thermochemical heat storage under monotonic and cyclic loading. *Applied Energy*, 136:289–302, 2014.

T. Nagel, S. Beckert, C. Lehmann, R. Gläser, and O. Kolditz. Multi-physical continuum models of thermochemical heat storage and transformation in porous media and powder beds—A review. *Applied Energy*, 178:323–345, 2016.

T. Nagel, P. Ostermeier, G. Seitz, H. Class, and R. Helmig. THC-Processes. In O. Kolditz, T. Nagel, H. Shao, W. Wang, and S. Bauer, editors, *Thermo-Hydro-Mechanical-Chemical Processes in Fractured Porous Media: Modelling and Benchmarking*. Springer, Cham, 2018. ISBN 978-3-319-68225-9. doi: https://doi.org/10.1007/978-3-319-68225-9.

D. A. Nield and A. Bejan. *Convection in Porous Media*. Springer New York, 2013. doi: 10.1007/978-1-4614-5541-7.

P. Nuske, V. Joekar-Niasar, and R. Helmig. Non-equilibrium in multiphase multicomponent flow in porous media: An evaporation example. *International Journal of Heat and Mass Transfer*, 74:128 – 142, 2014. ISSN 0017-9310. doi: https://doi.org/10.1016/j.ijheatmasstransfer.2014.03.011.

K. E. N'Tsoukpoe, T. Schmidt, H. U. Rammelberg, B. A. Watts, and W. K. Ruck. A systematic multi-step screening of numerous salt hydrates for low temperature thermochemical energy storage. *Applied Energy*, 124:1–16, 2014.

W. L. Oberkampf and C. J. Roy. *Verification and validation in scientific computing*. Cambridge University Press, 2010.

Z. Pan and C. Zhao. Gas–solid thermochemical heat storage reactors for high-temperature applications. *Energy*, 130:155–173, 2017.

P. Pardo, A. Deydier, Z. Anxionnaz-Minvielle, S. Rougé, M. Cabassud, and P. Cognet. A review on high temperature thermochemical heat energy storage. *Renewable and Sustainable Energy Reviews*, 32:591–610, 2014.

M. Pehnt, M. Arens, E. Jochem, and F. Idrissova. *Industrial waste heat – tapping into a neglected efficiency potential*, pages 691 – 700. ECEEE, 2011. ISBN 9789163344558.

M. Pijolat and M. Soustelle. Experimental tests to validate the rate-limiting step assumption used in the kinetic analysis of solid-state reactions. *Thermochimica Acta*, 478(1):34 – 40, 2008. doi: https://doi.org/10.1016/j.tca.2008.08.013.

B. E. Poling, J. M. Prausnitz, and J. P. O'Connell. *The properties of gases and liquids*, volume 5. McGraw-Hill New York, 2001.

F. Pukelsheim. *Optimal design of experiments*. SIAM, 2006.

Q. Ranjha and A. Oztekin. Numerical analyses of three-dimensional fixed reaction bed for thermochemical energy storage. *Renewable Energy*, 111:825 – 835, 2017. ISSN 0960-1481. doi: https://doi.org/10.1016/j.renene.2017.04.062.

C. Reddick, M. Sorin, J.-C. Bonhivers, and D. Laperle. Waste heat and renewable energy integration in buildings. *Energy and Buildings*, 211:109803, 2020. ISSN 0378-7788. doi: https://doi.org/10.1016/j.enbuild.2020.109803.

R. C. Reid, J. Prausnitz, and B. E. Poling. *The Properties of Gases and Liquids*. McGraw-Hill Inc., 1987.

M. Richter, E.-M. Habermann, E. Siebecke, and M. Linder. A systematic screening of salt hydrates as materials for a thermochemical heat transformer. *Thermochimica Acta*, 659:136–150, 2018.

K. Risthaus, I. Bürger, M. Linder, and M. Schmidt. Numerical analysis of the hydration of calcium oxide in a fixed bed reactor based on lab-scale experiments. *Applied Energy*, 261:114351, 2020. ISSN 0306-2619. doi: https://doi.org/10.1016/j.apenergy.2019.114351.

H. Ritchie. Statistical Review of World Energy2020 - 69th edition, 9 2020. URL `https://ourworldindata.org/ghg-emissions-by-sector`.

C. Roßkopf, M. Haas, A. Faik, M. Linder, and A. Wörner. Improving powder bed properties for thermochemical storage by adding nanoparticles. *Energy Conversion and Management*, 86:93 – 98, 2014. doi: https://doi.org/10.1016/j.enconman.2014.05.017.

C. Roßkopf, S. Afflerbach, M. Schmidt, B. Görtz, T. Kowald, M. Linder, and R. Trettin. Investigations of nano coated calcium hydroxide cycled in a thermochemical heat storage. *Energy Conversion and Management*, 97:94 – 102, 2015. doi: https://doi.org/10.1016/j.enconman.2015.03.034.

J. A. C. Samms and B. E. Evans. Thermal dissociation of Ca(OH)2 at elevated pressures. *Journal of Applied Chemistry*, 18(1):5–8, 1968. doi: 10.1002/jctb.5010180102.

F. Schaube. Untersuchungen zur Nutzung des CaO/Ca(OH)2 -Reaktionssystems für die thermochemische Wärmespeicherung. Hochschulschrift, Universität Stuttgart, München, 2013.

F. Schaube, A. Wörner, and R. Tamme. High temperature thermochemical heat storage for concentrated solar power using gas-solid reactions. *Journal of solar energy engineering*, 133(3):031006, 2011.

F. Schaube, L. Koch, A. Wörner, and H. Müller-Steinhagen. A thermodynamic and kinetic study of the de-and rehydration of Ca(OH)2 at high H2O partial pressures for thermo-chemical heat storage. *Thermochimica acta*, 538:9–20, 2012.

F. Schaube, A. Kohzer, J. Schütz, A. Wörner, and H. Müller-Steinhagen. De- and rehydration of Ca(OH)2 in a reactor with direct heat transfer for thermo-chemical heat storage. Part A: Experimental results . *Chemical Engineering Research and Design*, 91(5):856 – 864, 2013a. ISSN 0263-8762. doi: http://dx.doi.org/10.1016/j.cherd.2012.09.020.

F. Schaube, I. Utz, A. Wörner, and H. Müller-Steinhagen. De- and rehydration of Ca(OH)2 in a reactor with direct heat transfer for thermo-chemical heat storage. Part B: Validation of model . *Chemical Engineering Research and Design*, 91(5):865 – 873, 2013b. ISSN 0263-8762. doi: http://dx.doi.org/10.1016/j.cherd.2013.02.019.

M. Schmidt. Experimental investigation of $Ca(OH)_2$ as thermochemical energy storage at process relevant boundary conditions. Hochschulschrift, University of Stuttgart, Stuttgart, 2017.

M. Schmidt and M. Linder. Power generation based on the Ca(OH)2/ CaO thermochemical storage system – Experimental investigation of discharge operation modes in lab scale and corresponding conceptual process design. *Applied Energy*, 203:594 – 607, 2017. doi: https://doi.org/10.1016/j.apenergy.2017.06.063.

M. Schmidt, C. Szczukowski, C. Roßkopf, M. Linder, and A. Wörner. Experimental results of a 10 kW high temperature thermochemical storage reactor based on calcium hydroxide. *Applied Thermal Engineering*, 62(2):553 – 559, 2014. doi: https://doi.org/10.1016/j.applthermaleng.2013.09.020.

M. Schmidt, A. Gutierrez, and M. Linder. Thermochemical energy storage with CaO/Ca(OH)2 – Experimental investigation of the thermal capability at low vapor pressures in a lab scale reactor. *Applied Energy*, 188:672 – 681, 2017. doi: https://doi.org/10.1016/j.apenergy.2016.11.023.

P. Schmidt. On the design of a reactor for high temperature heat storage by means of reversible chemical reactions. Master's thesis, KTH school of Industrial Engineering an Management, 2011.

J. Schönherr. Untersuchung von Rissstrukturen bei der thermochemischen Wärmespeicherung mit $CaO/Ca(OH)_2$. Bachelor's thesis, Universität Stuttgart, Stuttgart, 2020.

G. Seitz, R. Helmig, and H. Class. A numerical modeling study on the influence of porosity changes during thermochemical heat storage. *Applied Energy*, 259:114152, 2020.

G. Seitz, F. Mohammadi, and H. Class. Thermochemical Heat Storage in a Lab-Scale Indirectly Operated CaO/Ca(OH)2 Reactor—Numerical Modeling and Model Validation through Inverse Parameter Estimation. *Applied Sciences*, 11(2), 2021. ISSN 2076-3417. doi: 10.3390/app11020682.

H. Shao, T. Nagel, C. Roßkopf, M. Linder, A. Wörner, and O. Kolditz. Non-equilibrium thermo-chemical heat storage in porous media: Part 2 – A 1D computational model for a calcium hydroxide reaction system. *Energy*, 60:271–282, 2013. ISSN 0360-5442. doi: 10.1016/j.energy.2013.07.063.

J. Shi and J. Wang. A numerical investigation of transpiration cooling with liquid coolant phase change. *Transport in porous media*, 87(3):703–716, 2011.

J. Stengler and M. Linder. Thermal energy storage combined with a temperature boost: An underestimated feature of thermochemical systems. *Applied Energy*, 262:114530, 2020. ISSN 0306-2619. doi: https://doi.org/10.1016/j.apenergy.2020.114530. URL `http://www.sciencedirect.com/science/article/pii/S0306261920300428`.

J. Stengler, T. Ascher, and M. Linder. High temperature thermochemical heat transformation based on SrBr2. 2017.

M. Sterner and I. Stadler. *Energiespeicher-Bedarf, Technologien, Integration*. Springer-Verlag, 2014.

M. Stoppok, A. Jess, R. Freitag, and E. Alber. Of culture, consumption and cost: a comparative analysis of household energy consumption in kenya, germany and spain. *Energy research & social science*, 40:127–139, 2018.

R. Taylor and R. Krishna, editors. *Multicomponent mass transfer*. Wiley series in chemical engineering. Wiley, New York [u.a.], 1993. ISBN 0471574171.

M. E. Tipping, A. C. Faul, et al. Fast marginal likelihood maximisation for sparse bayesian models. In *AISTATS*, 2003.

UNFCCC. UN Treaty No. XXVII-7-d, Dec. 2015. URL `https://treaties.un.org/pages/ViewDetails.aspx?src=TREATY&mtdsg_no=XXVII-7-d&chapter=27&clang=_en`. Accessed 10 October 2020.

D. Ürge-Vorsatz and B. Metz. Energy efficiency: how far does it get us in controlling climate change? *Energy Efficiency*, 2(2):87–94, 2009.

V. Van Essen, H. Zondag, J. C. Gores, L. Bleijendaal, M. Bakker, R. Schuitema, W. Van Helden, Z. He, and C. Rindt. Characterization of MgSO4 hydrate for thermochemical seasonal heat storage. *Journal of solar energy engineering*, 131(4):041014, 2009.

S. Vyazovkin, A. K. Burnham, J. M. Criado, L. A. Pérez-Maqueda, C. Popescu, and N. Sbirrazzuoli. ICTAC Kinetics Committee recommendations for performing kinetic computations on thermal analysis data. *Thermochimica acta*, 520(1-2):1–19, 2011.

P.-R. Wagner, J. Nagel, S. Marelli, and B. Sudret. UQLab user manual – Bayesian inversion for model calibration and validation. Technical report, Chair of Risk, Safety and Uncertainty Quantification, ETH Zurich, Switzerland, 2019. Report # UQLab-V1.3-113.

N. Wakao and S. Kagei. *Heat and mass transfer in packed beds*, volume 1. Taylor & Francis, 1982.

W. Wentworth and E. Chen. Simple thermal decomposition reactions for storage of solar thermal energy. *Solar Energy*, 18(3):205 – 214, 1976. ISSN 0038-092X. doi: https://doi.org/10.1016/0038-092X(76)90019-0.

F. M. White. *Fluid mechanics*. McGraw-Hill series in mechanical engineering. McGraw-Hill education, New York, NY, Eighth edition in SI units edition, 2016. ISBN 9789814720175.

W. Woodside and J. Messmer. Thermal conductivity of porous media in unconsolidated sands. *Journal of Applied Physics*, 32(9):1688–1699, 1961. doi: 10.1063/1.1728419.

J. Yan, C. Zhao, B. Xia, and T. Wang. The effect of dehydration temperatures on the performance of the CaO/Ca(OH)2 thermochemical heat storage system. *Energy*, 186:115837, 2019. doi: https://doi.org/10.1016/j.energy.2019.07.167.

Y. Yuan, N. Gholizadeh Doonechaly, and S. Rahman. An analytical model of apparent gas permeability for tight porous media. *Transport in Porous Media*, 111(1):193–214, Jan 2016. doi: 10.1007/s11242-015-0589-3.

A. S. Ziarani and R. Aguilera. Knudsen's permeability correction for tight porous media. *Transport in porous media*, 91(1):239–260, 2012.

H. Zsiborács, N. H. Baranyai, A. Vincze, L. Zentkó, Z. Birkner, K. Máté, and G. Pintér. Intermittent renewable energy sources: The role of energy storage in the european power system of 2040. *Electronics*, 8(7), 2019. doi: 10.3390/electronics8070729.

Institut für Wasser- und Umweltsystemmodellierung
Universität Stuttgart

Pfaffenwaldring 61
70569 Stuttgart (Vaihingen)
Telefon (0711) 685 - 60156
Telefax (0711) 685 - 51073
E-Mail: iws@iws.uni-stuttgart.de
http://www.iws.uni-stuttgart.de

Verzeichnis der Mitteilungshefte

5 Plate, Erich: *Beitrag zur Bestimmung der Windgeschwindigkeitsverteilung in der durch eine Wand gestörten bodennahen Luftschicht*, und
Röhnisch, Arthur; Marotz, Günter: *Neue Baustoffe und Bauausführungen für den Schutz der Böschungen und der Sohle von Kanälen, Flüssen und Häfen; Gestehungskosten und jeweilige Vorteile*, sowie
Unny, T.E.: *Schwingungsuntersuchungen am Kegelstrahlschieber*, 1967

6 Seiler, Erich: *Die Ermittlung des Anlagenwertes der bundeseigenen Binnenschiffahrtsstraßen und Talsperren und des Anteils der Binnenschiffahrt an diesem Wert*, 1967

7 *Sonderheft anläßlich des 65. Geburtstages von Prof. Arthur Röhnisch mit Beiträgen von* Benk, Dieter; Breitling, J.; Gurr, Siegfried; Haberhauer, Robert; Honekamp, Hermann; Kuz, Klaus Dieter; Marotz, Günter; Mayer-Vorfelder, Hans-Jörg; Miller, Rudolf; Plate, Erich J.; Radomski, Helge; Schwarz, Helmut; Vollmer, Ernst; Wildenhahn, Eberhard; 1967

8 Jumikis, Alfred: *Beitrag zur experimentellen Untersuchung des Wassernachschubs in einem gefrierenden Boden und die Beurteilung der Ergebnisse*, 1968

9 Marotz, Günter: *Technische Grundlagen einer Wasserspeicherung im natürlichen Untergrund*, 1968

10 Radomski, Helge: *Untersuchungen über den Einfluß der Querschnittsform wellenförmiger Spundwände auf die statischen und rammtechnischen Eigenschaften*, 1968

11 Schwarz, Helmut: *Die Grenztragfähigkeit des Baugrundes bei Einwirkung vertikal gezogener Ankerplatten als zweidimensionales Bruchproblem*, 1969

12 Erbel, Klaus: *Ein Beitrag zur Untersuchung der Metamorphose von Mittelgebirgsschneedecken unter besonderer Berücksichtigung eines Verfahrens zur Bestimmung der thermischen Schneequalität*, 1969

13 Westhaus, Karl-Heinz: *Der Strukturwandel in der Binnenschiffahrt und sein Einfluß auf den Ausbau der Binnenschiffskanäle*, 1969

14 Mayer-Vorfelder, Hans-Jörg: *Ein Beitrag zur Berechnung des Erdwiderstandes unter Ansatz der logarithmischen Spirale als Gleitflächenfunktion*, 1970

15 Schulz, Manfred: *Berechnung des räumlichen Erddruckes auf die Wandung kreiszylindrischer Körper*, 1970

16 Mobasseri, Manoutschehr: *Die Rippenstützmauer. Konstruktion und Grenzen ihrer Standsicherheit*, 1970

17 Benk, Dieter: *Ein Beitrag zum Betrieb und zur Bemessung von Hochwasserrückhaltebecken*, 1970

18 Gàl, Attila: *Bestimmung der mitschwingenden Wassermasse bei überströmten Fischbauchklappen mit kreiszylindrischem Staublech*, 1971, vergriffen

19 Kuz, Klaus Dieter: *Ein Beitrag zur Frage des Einsetzens von Kavitationserscheinungen in einer Düsenströmung bei Berücksichtigung der im Wasser gelösten Gase*, 1971, vergriffen

20 Schaak, Hartmut: *Verteilleitungen von Wasserkraftanlagen*, 1971

21 *Sonderheft zur Eröffnung der neuen Versuchsanstalt des Instituts für Wasserbau der Universität Stuttgart mit Beiträgen von* Brombach, Hansjörg; Dirksen, Wolfram; Gàl, Attila; Gerlach, Reinhard; Giesecke, Jürgen; Holthoff, Franz-Josef; Kuz, Klaus Dieter; Marotz, Günter; Minor, Hans-Erwin; Petrikat, Kurt; Röhnisch, Arthur; Rueff, Helge; Schwarz, Helmut; Vollmer, Ernst; Wildenhahn, Eberhard; 1972

22 Wang, Chung-su: *Ein Beitrag zur Berechnung der Schwingungen an Kegelstrahlschiebern*, 1972

23 Mayer-Vorfelder, Hans-Jörg: *Erdwiderstandsbeiwerte nach dem Ohde-Variationsverfahren*, 1972

24 Minor, Hans-Erwin: *Beitrag zur Bestimmung der Schwingungsanfachungsfunktionen überströmter Stauklappen*, 1972, vergriffen

25 Brombach, Hansjörg: *Untersuchung strömungsmechanischer Elemente (Fluidik) und die Möglichkeit der Anwendung von Wirbelkammerelementen im Wasserbau*, 1972, vergriffen

26 Wildenhahn, Eberhard: *Beitrag zur Berechnung von Horizontalfilterbrunnen*, 1972

27 Steinlein, Helmut: *Die Eliminierung der Schwebstoffe aus Flußwasser zum Zweck der unterirdischen Wasserspeicherung, gezeigt am Beispiel der Iller*, 1972

28 Holthoff, Franz Josef: *Die Überwindung großer Hubhöhen in der Binnenschiffahrt durch Schwimmerhebewerke*, 1973

29 Röder, Karl: *Einwirkungen aus Baugrundbewegungen auf trog- und kastenförmige Konstruktionen des Wasser- und Tunnelbaues*, 1973

30 Kretschmer, Heinz: *Die Bemessung von Bogenstaumauern in Abhängigkeit von der Talform*, 1973

31 Honekamp, Hermann: *Beitrag zur Berechnung der Montage von Unterwasserpipelines*, 1973

32 Giesecke, Jürgen: *Die Wirbelkammertriode als neuartiges Steuerorgan im Wasserbau*, und Brombach, Hansjörg: *Entwicklung, Bauformen, Wirkungsweise und Steuereigenschaften von Wirbelkammerverstärkern*, 1974

33 Rueff, Helge: *Untersuchung der schwingungserregenden Kräfte an zwei hintereinander angeordneten Tiefschützen unter besonderer Berücksichtigung von Kavitation*, 1974

34 Röhnisch, Arthur: *Einpreßversuche mit Zementmörtel für Spannbeton - Vergleich der Ergebnisse von Modellversuchen mit Ausführungen in Hüllwellrohren*, 1975

35 *Sonderheft anläßlich des 65. Geburtstages von Prof. Dr.-Ing. Kurt Petrikat mit Beiträgen von*: Brombach, Hansjörg; Erbel, Klaus; Flinspach, Dieter; Fischer jr., Richard; Gàl, Attila; Gerlach, Reinhard; Giesecke, Jürgen; Haberhauer, Robert; Hafner Edzard; Hausenblas, Bernhard; Horlacher, Hans-Burkhard; Hutarew, Andreas; Knoll, Manfred; Krummet, Ralph; Marotz, Günter; Merkle, Theodor; Miller, Christoph; Minor, Hans-Erwin; Neumayer, Hans; Rao, Syamala; Rath, Paul; Rueff, Helge; Ruppert, Jürgen; Schwarz, Wolfgang; Topal-Gökceli, Mehmet; Vollmer, Ernst; Wang, Chung-su; Weber, Hans-Georg; 1975

36 Berger, Jochum: *Beitrag zur Berechnung des Spannungszustandes in rotationssymmetrisch belasteten Kugelschalen veränderlicher Wandstärke unter Gas- und Flüssigkeitsdruck durch Integration schwach singulärer Differentialgleichungen*, 1975

37 Dirksen, Wolfram: *Berechnung instationärer Abflußvorgänge in gestauten Gerinnen mittels Differenzenverfahren und die Anwendung auf Hochwasserrückhaltebecken*, 1976

38 Horlacher, Hans-Burkhard: *Berechnung instationärer Temperatur- und Wärmespannungsfelder in langen mehrschichtigen Hohlzylindern*, 1976

39 Hafner, Edzard: *Untersuchung der hydrodynamischen Kräfte auf Baukörper im Tiefwasserbereich des Meeres*, 1977, ISBN 3-921694-39-6

40 Ruppert, Jürgen: *Über den Axialwirbelkammerverstärker für den Einsatz im Wasserbau*, 1977, ISBN 3-921694-40-X

41 Hutarew, Andreas: *Beitrag zur Beeinflußbarkeit des Sauerstoffgehalts in Fließgewässern an Abstürzen und Wehren*, 1977, ISBN 3-921694-41-8, *vergriffen*

42 Miller, Christoph: *Ein Beitrag zur Bestimmung der schwingungserregenden Kräfte an unterströmten Wehren*, 1977, ISBN 3-921694-42-6

43 Schwarz, Wolfgang: *Druckstoßberechnung unter Berücksichtigung der Radial- und Längsverschiebungen der Rohrwandung*, 1978, ISBN 3-921694-43-4

44 Kinzelbach, Wolfgang: *Numerische Untersuchungen über den optimalen Einsatz variabler Kühlsysteme einer Kraftwerkskette am Beispiel Oberrhein*, 1978, ISBN 3-921694-44-2

45 Barczewski, Baldur: *Neue Meßmethoden für Wasser-Luftgemische und deren Anwendung auf zweiphasige Auftriebsstrahlen*, 1979, ISBN 3-921694-45-0

46 Neumayer, Hans: *Untersuchung der Strömungsvorgänge in radialen Wirbelkammerverstärkern*, 1979, ISBN 3-921694-46-9

47 Elalfy, Youssef-Elhassan: *Untersuchung der Strömungsvorgänge in Wirbelkammerdioden und -drosseln*, 1979, ISBN 3-921694-47-7

48 Brombach, Hansjörg: *Automatisierung der Bewirtschaftung von Wasserspeichern*, 1981, ISBN 3-921694-48-5

49 Geldner, Peter: *Deterministische und stochastische Methoden zur Bestimmung der Selbstdichtung von Gewässern*, 1981, ISBN 3-921694-49-3, *vergriffen*

50 Mehlhorn, Hans: *Temperaturveränderungen im Grundwasser durch Brauchwassereinleitungen*, 1982, ISBN 3-921694-50-7, *vergriffen*

51 Hafner, Edzard: *Rohrleitungen und Behälter im Meer*, 1983, ISBN 3-921694-51-5

52 Rinnert, Bernd: *Hydrodynamische Dispersion in porösen Medien: Einfluß von Dichteunterschieden auf die Vertikalvermischung in horizontaler Strömung*, 1983, ISBN 3-921694-52-3, *vergriffen*

53 Lindner, Wulf: *Steuerung von Grundwasserentnahmen unter Einhaltung ökologischer Kriterien*, 1983, ISBN 3-921694-53-1, *vergriffen*

54 Herr, Michael; Herzer, Jörg; Kinzelbach, Wolfgang; Kobus, Helmut; Rinnert, Bernd: *Methoden zur rechnerischen Erfassung und hydraulischen Sanierung von Grundwasserkontaminationen*, 1983, ISBN 3-921694-54-X

55 Schmitt, Paul: *Wege zur Automatisierung der Niederschlagsermittlung*, 1984, ISBN 3-921694-55-8, *vergriffen*

56 Müller, Peter: *Transport und selektive Sedimentation von Schwebstoffen bei gestautem Abfluß*, 1985, ISBN 3-921694-56-6

57 El-Qawasmeh, Fuad: *Möglichkeiten und Grenzen der Tropfbewässerung unter besonderer Berücksichtigung der Verstopfungsanfälligkeit der Tropfelemente*, 1985, ISBN 3-921694-57-4, *vergriffen*

58 Kirchenbaur, Klaus: *Mikroprozessorgesteuerte Erfassung instationärer Druckfelder am Beispiel seegangsbelasteter Baukörper*, 1985, ISBN 3-921694-58-2

59 Kobus, Helmut (Hrsg.): *Modellierung des großräumigen Wärme- und Schadstofftransports im Grundwasser*, Tätigkeitsbericht 1984/85 (DFG-Forschergruppe an den Universitäten Hohenheim, Karlsruhe und Stuttgart), 1985, ISBN 3-921694-59-0, *vergriffen*

60 Spitz, Karlheinz: *Dispersion in porösen Medien: Einfluß von Inhomogenitäten und Dichteunterschieden*, 1985, ISBN 3-921694-60-4, *vergriffen*

61 Kobus, Helmut: *An Introduction to Air-Water Flows in Hydraulics*, 1985, ISBN 3-921694-61-2

62 Kaleris, Vassilios: *Erfassung des Austausches von Oberflächen- und Grundwasser in horizontalebenen Grundwassermodellen*, 1986, ISBN 3-921694-62-0

63 Herr, Michael: *Grundlagen der hydraulischen Sanierung verunreinigter Porengrundwasserleiter*, 1987, ISBN 3-921694-63-9

64 Marx, Walter: *Berechnung von Temperatur und Spannung in Massenbeton infolge Hydratation*, 1987, ISBN 3-921694-64-7

65 Koschitzky, Hans-Peter: *Dimensionierungskonzept für Sohlbelüfter in Schußrinnen zur Vermeidung von Kavitationsschäden*, 1987, ISBN 3-921694-65-5

66 Kobus, Helmut (Hrsg.): *Modellierung des großräumigen Wärme- und Schadstofftransports im Grundwasser*, Tätigkeitsbericht 1986/87 (DFG-Forschergruppe an den Universitäten Hohenheim, Karlsruhe und Stuttgart) 1987, ISBN 3-921694-66-3

67 Söll, Thomas: *Berechnungsverfahren zur Abschätzung anthropogener Temperaturanomalien im Grundwasser*, 1988, ISBN 3-921694-67-1

68 Dittrich, Andreas; Westrich, Bernd: *Bodenseeufererosion, Bestandsaufnahme und Bewertung*, 1988, ISBN 3-921694-68-X, *vergriffen*

69 Huwe, Bernd; van der Ploeg, Rienk R.: *Modelle zur Simulation des Stickstoffhaushaltes von Standorten mit unterschiedlicher landwirtschaftlicher Nutzung*, 1988, ISBN 3-921694-69-8, *vergriffen*

70 Stephan, Karl: *Integration elliptischer Funktionen*, 1988, ISBN 3-921694-70-1

71 Kobus, Helmut; Zilliox, Lothaire (Hrsg.): *Nitratbelastung des Grundwassers, Auswirkungen der Landwirtschaft auf die Grundwasser- und Rohwasserbeschaffenheit und Maßnahmen zum Schutz des Grundwassers*. Vorträge des deutsch-französischen Kolloquiums am 6. Oktober 1988, Universitäten Stuttgart und Louis Pasteur Strasbourg (Vorträge in deutsch oder französisch, Kurzfassungen zweisprachig), 1988, ISBN 3-921694-71-X

72 Soyeaux, Renald: *Unterströmung von Stauanlagen auf klüftigem Untergrund unter Berücksichtigung laminarer und turbulenter Fließzustände*,1991, ISBN 3-921694-72-8

73 Kohane, Roberto: *Berechnungsmethoden für Hochwasserabfluß in Fließgewässern mit überströmten Vorländern*, 1991, ISBN 3-921694-73-6

74 Hassinger, Reinhard: *Beitrag zur Hydraulik und Bemessung von Blocksteinrampen in flexibler Bauweise*, 1991, ISBN 3-921694-74-4, vergriffen

75 Schäfer, Gerhard: *Einfluß von Schichtenstrukturen und lokalen Einlagerungen auf die Längsdispersion in Porengrundwasserleitern*, 1991, ISBN 3-921694-75-2

76 Giesecke, Jürgen: *Vorträge, Wasserwirtschaft in stark besiedelten Regionen; Umweltforschung mit Schwerpunkt Wasserwirtschaft*, 1991, ISBN 3-921694-76-0

77 Huwe, Bernd: *Deterministische und stochastische Ansätze zur Modellierung des Stickstoffhaushalts landwirtschaftlich genutzter Flächen auf unterschiedlichem Skalenniveau*, 1992, ISBN 3-921694-77-9, vergriffen

78 Rommel, Michael: *Verwendung von Kluftdaten zur realitätsnahen Generierung von Kluftnetzen mit anschließender laminar-turbulenter Strömungsberechnung*, 1993, ISBN 3-92 1694-78-7

79 Marschall, Paul: *Die Ermittlung lokaler Stofffrachten im Grundwasser mit Hilfe von Einbohrloch-Meßverfahren*, 1993, ISBN 3-921694-79-5, vergriffen

80 Ptak, Thomas: *Stofftransport in heterogenen Porenaquiferen: Felduntersuchungen und stochastische Modellierung*, 1993, ISBN 3-921694-80-9, vergriffen

81 Haakh, Frieder: *Transientes Strömungsverhalten in Wirbelkammern,* 1993, ISBN 3-921694-81-7

82 Kobus, Helmut; Cirpka, Olaf; Barczewski, Baldur; Koschitzky, Hans-Peter: *Versuchseinrichtung zur Grundwasser- und Altlastensanierung VEGAS, Konzeption und Programmrahmen*, 1993, ISBN 3-921694-82-5

83 Zang, Weidong: *Optimaler Echtzeit-Betrieb eines Speichers mit aktueller Abflußregenerierung*, 1994, ISBN 3-921694-83-3, vergriffen

84 Franke, Hans-Jörg: *Stochastische Modellierung eines flächenhaften Stoffeintrages und Transports in Grundwasser am Beispiel der Pflanzenschutzmittelproblematik*, 1995, ISBN 3-921694-84-1

85 Lang, Ulrich: *Simulation regionaler Strömungs- und Transportvorgänge in Karstaquiferen mit Hilfe des Doppelkontinuum-Ansatzes: Methodenentwicklung und Parameteridentifikation*, 1995, ISBN 3-921694-85-X, vergriffen

86 Helmig, Rainer: *Einführung in die Numerischen Methoden der Hydromechanik*, 1996, ISBN 3-921694-86-8, vergriffen

87 Cirpka, Olaf: *CONTRACT: A Numerical Tool for Contaminant Transport and Chemical Transformations - Theory and Program Documentation -*, 1996, ISBN 3-921694-87-6

88 Haberlandt, Uwe: *Stochastische Synthese und Regionalisierung des Niederschlages für Schmutzfrachtberechnungen*, 1996, ISBN 3-921694-88-4

89 Croisé, Jean: *Extraktion von flüchtigen Chemikalien aus natürlichen Lockergesteinen mittels erzwungener Luftströmung*, 1996, ISBN 3-921694-89-2, vergriffen

90 Jorde, Klaus: *Ökologisch begründete, dynamische Mindestwasserregelungen bei Ausleitungskraftwerken*, 1997, ISBN 3-921694-90-6, vergriffen

91 Helmig, Rainer: *Gekoppelte Strömungs- und Transportprozesse im Untergrund - Ein Beitrag zur Hydrosystemmodellierung-*, 1998, ISBN 3-921694-91-4, vergriffen

92 Emmert, Martin: *Numerische Modellierung nichtisothermer Gas-Wasser Systeme in porösen Medien,* 1997, ISBN 3-921694-92-2

93 Kern, Ulrich: *Transport von Schweb- und Schadstoffen in staugeregelten Fließgewässern am Beispiel des Neckars*, 1997, ISBN 3-921694-93-0, vergriffen

94 Förster, Georg: *Druckstoßdämpfung durch große Luftblasen in Hochpunkten von Rohrleitungen 1997*, ISBN 3-921694-94-9

95 Cirpka, Olaf: *Numerische Methoden zur Simulation des reaktiven Mehrkomponententransports im Grundwasser*, 1997, ISBN 3-921694-95-7, *vergriffen*

96 Färber, Arne: *Wärmetransport in der ungesättigten Bodenzone: Entwicklung einer thermischen In-situ-Sanierungstechnologie*, 1997, ISBN 3-921694-96-5

97 Betz, Christoph: *Wasserdampfdestillation von Schadstoffen im porösen Medium: Entwicklung einer thermischen In-situ-Sanierungstechnologie*, 1998, SBN 3-921694-97-3

98 Xu, Yichun: *Numerical Modeling of Suspended Sediment Transport in Rivers*, 1998, ISBN 3-921694-98-1, *vergriffen*

99 Wüst, Wolfgang: *Geochemische Untersuchungen zur Sanierung CKW-kontaminierter Aquifere mit Fe(0)-Reaktionswänden,* 2000, ISBN 3-933761-02-2

100 Sheta, Hussam: *Simulation von Mehrphasenvorgängen in porösen Medien unter Einbeziehung von Hysterese-Effekten*, 2000, ISBN 3-933761-03-4

101 Ayros, Edwin: *Regionalisierung extremer Abflüsse auf der Grundlage statistischer Verfahren*, 2000, ISBN 3-933761-04-2, *vergriffen*

102 Huber, Ralf: *Compositional Multiphase Flow and Transport in Heterogeneous Porous Media*, 2000, ISBN 3-933761-05-0

103 Braun, Christopherus: *Ein Upscaling-Verfahren für Mehrphasenströmungen in porösen Medien*, 2000, ISBN 3-933761-06-9

104 Hofmann, Bernd: *Entwicklung eines rechnergestützten Managementsystems zur Beurteilung von Grundwasserschadensfällen*, 2000, ISBN 3-933761-07-7

105 Class, Holger: *Theorie und numerische Modellierung nichtisothermer Mehrphasenprozesse in NAPL-kontaminierten porösen Medien,* 2001, ISBN 3-933761-08-5

106 Schmidt, Reinhard: *Wasserdampf- und Heißluftinjektion zur thermischen Sanierung kontaminierter Standorte*, 2001, ISBN 3-933761-09-3

107 Josef, Reinhold: *Schadstoffextraktion mit hydraulischen Sanierungsverfahren unter Anwendung von grenzflächenaktiven Stoffen*, 2001, ISBN 3-933761-10-7

108 Schneider, Matthias: *Habitat- und Abflussmodellierung für Fließgewässer mit unscharfen Berechnungsansätzen*, 2001, ISBN 3-933761-11-5

109 Rathgeb, Andreas: *Hydrodynamische Bemessungsgrundlagen für Lockerdeckwerke an überströmbaren Erddämmen*, 2001, ISBN 3-933761-12-3

110 Lang, Stefan: *Parallele numerische Simulation instätionärer Probleme mit adaptiven Methoden auf unstrukturierten Gittern*, 2001, ISBN 3-933761-13-1

111 Appt, Jochen; Stumpp Simone: *Die Bodensee-Messkampagne 2001, IWS/CWR Lake Constance Measurement Program 2001*, 2002, ISBN 3-933761-14-X

112 Heimerl, Stephan: *Systematische Beurteilung von Wasserkraftprojekten,* 2002, ISBN 3-933761-15-8, *vergriffen*

113 Iqbal, Amin: *On the Management and Salinity Control of Drip Irrigation,* 2002, ISBN 3-933761-16-6

114 Silberhorn-Hemminger, Annette: *Modellierung von Kluftaquifersystemen: Geostatistische Analyse und deterministisch-stochastische Kluftgenerierung,* 2002, ISBN 3-933761-17-4

115 Winkler, Angela: *Prozesse des Wärme- und Stofftransports bei der In-situ-Sanierung mit festen Wärmequellen,* 2003, ISBN 3-933761-18-2

116 Marx, Walter: *Wasserkraft, Bewässerung, Umwelt - Planungs- und Bewertungsschwerpunkte der Wasserbewirtschaftung,* 2003, ISBN 3-933761-19-0

117 Hinkelmann, Reinhard: *Efficient Numerical Methods and Information-Processing Techniques in Environment Water,* 2003, ISBN 3-933761-20-4

118 Samaniego-Eguiguren, Luis Eduardo: *Hydrological Consequences of Land Use / Land Cover and Climatic Changes in Mesoscale Catchments*, 2003, ISBN 3-933761-21-2

119 Neunhäuserer, Lina: *Diskretisierungsansätze zur Modellierung von Strömungs- und Transportprozessen in geklüftet-porösen Medien*, 2003, ISBN 3-933761-22-0

120 Paul, Maren: *Simulation of Two-Phase Flow in Heterogeneous Poros Media with Adaptive Methods*, 2003, ISBN 3-933761-23-9

121 Ehret, Uwe: *Rainfall and Flood Nowcasting in Small Catchments using Weather Radar*, 2003, ISBN 3-933761-24-7

122 Haag, Ingo: *Der Sauerstoffhaushalt staugeregelter Flüsse am Beispiel des Neckars - Analysen, Experimente, Simulationen -,* 2003, ISBN 3-933761-25-5

123 Appt, Jochen: *Analysis of Basin-Scale Internal Waves in Upper Lake Constance,* 2003, ISBN 3-933761-26-3

124 Hrsg.: Schrenk, Volker; Batereau, Katrin; Barczewski, Baldur; Weber, Karolin und Koschitzky, Hans-Peter: *Symposium Ressource Fläche und VEGAS - Statuskolloquium 2003, 30. September und 1. Oktober 2003,* 2003, ISBN 3-933761-27-1

125 Omar Khalil Ouda: *Optimisation of Agricultural Water Use: A Decision Support System for the Gaza Strip,* 2003, ISBN 3-933761-28-0

126 Batereau, Katrin: *Sensorbasierte Bodenluftmessung zur Vor-Ort-Erkundung von Schadensherden im Untergrund*, 2004, ISBN 3-933761-29-8

127 Witt, Oliver: *Erosionsstabilität von Gewässersedimenten mit Auswirkung auf den Stofftransport bei Hochwasser am Beispiel ausgewählter Stauhaltungen des Oberrheins*, 2004, ISBN 3-933761-30-1

128 Jakobs, Hartmut: *Simulation nicht-isothermer Gas-Wasser-Prozesse in komplexen Kluft-Matrix-Systemen*, 2004, ISBN 3-933761-31-X

129 Li, Chen-Chien: *Deterministisch-stochastisches Berechnungskonzept zur Beurteilung der Auswirkungen erosiver Hochwasserereignisse in Flussstauhaltungen,* 2004, ISBN 3-933761-32-8

130 Reichenberger, Volker; Helmig, Rainer; Jakobs, Hartmut; Bastian, Peter; Niessner, Jennifer: *Complex Gas-Water Processes in Discrete Fracture-Matrix Systems: Up-scaling, Mass-Conservative Discretization and Efficient Multilevel Solution,* 2004, ISBN 3-933761-33-6

131 Hrsg.: Barczewski, Baldur; Koschitzky, Hans-Peter; Weber, Karolin; Wege, Ralf: *VEGAS - Statuskolloquium 2004,* Tagungsband zur Veranstaltung am 05. Oktober 2004 an der Universität Stuttgart, Campus Stuttgart-Vaihingen, 2004, ISBN 3-933761-34-4

132 Asie, Kemal Jabir: *Finite Volume Models for Multiphase Multicomponent Flow through Porous Media*. 2005, ISBN 3-933761-35-2

133 Jacoub, George: *Development of a 2-D Numerical Module for Particulate Contaminant Transport in Flood Retention Reservoirs and Impounded Rivers,* 2004, ISBN 3-933761-36-0

134 Nowak, Wolfgang: *Geostatistical Methods for the Identification of Flow and Transport Parameters in the Subsurface,* 2005, ISBN 3-933761-37-9

135 Süß, Mia: *Analysis of the influence of structures and boundaries on flow and transport processes in fractured porous media*, 2005, ISBN 3-933761-38-7

136 Jose, Surabhin Chackiath: *Experimental Investigations on Longitudinal Dispersive Mixing in Heterogeneous Aquifers,* 2005, ISBN: 3-933761-39-5

137 Filiz, Fulya: *Linking Large-Scale Meteorological Conditions to Floods in Mesoscale Catchments,* 2005, ISBN 3-933761-40-9

138 Qin, Minghao: *Wirklichkeitsnahe und recheneffiziente Ermittlung von Temperatur und Spannungen bei großen RCC-Staumauern*, 2005, ISBN 3-933761-41-7

139 Kobayashi, Kenichiro: *Optimization Methods for Multiphase Systems in the Subsurface - Application to Methane Migration in Coal Mining Areas*, 2005, ISBN 3-933761-42-5

140 Rahman, Md. Arifur: *Experimental Investigations on Transverse Dispersive Mixing in Heterogeneous Porous Media,* 2005, ISBN 3-933761-43-3

141 Schrenk, Volker: *Ökobilanzen zur Bewertung von Altlastensanierungsmaßnahmen,* 2005, ISBN 3-933761-44-1

142 Hundecha, Hirpa Yeshewatesfa: *Regionalization of Parameters of a Conceptual Rainfall-Runoff Model*, 2005, ISBN: 3-933761-45-X

143 Wege, Ralf: *Untersuchungs- und Überwachungsmethoden für die Beurteilung natürlicher Selbstreinigungsprozesse im Grundwasser,* 2005, ISBN 3-933761-46-8

144 Breiting, Thomas: *Techniken und Methoden der Hydroinformatik - Modellierung von komplexen Hydrosystemen im Untergrund*, 2006, ISBN 3-933761-47-6

145 Hrsg.: Braun, Jürgen; Koschitzky, Hans-Peter; Müller, Martin: *Ressource Untergrund: 10 Jahre VEGAS: Forschung und Technologieentwicklung zum Schutz von Grundwasser und Boden,* Tagungsband zur Veranstaltung am 28. und 29. September 2005 an der Universität Stuttgart, Campus Stuttgart-Vaihingen, 2005, ISBN 3-933761-48-4

146 Rojanschi, Vlad: *Abflusskonzentration in mesoskaligen Einzugsgebieten unter Berücksichtigung des Sickerraumes,* 2006, ISBN 3-933761-49-2

147 Winkler, Nina Simone: *Optimierung der Steuerung von Hochwasserrückhaltebeckensystemen,* 2006, ISBN 3-933761-50-6

148 Wolf, Jens: *Räumlich differenzierte Modellierung der Grundwasserströmung alluvialer Aquifere für mesoskalige Einzugsgebiete*, 2006, ISBN: 3-933761-51-4

149 Kohler, Beate: *Externe Effekte der Laufwasserkraftnutzung*, 2006, ISBN 3-933761-52-2

150 Hrsg.: Braun, Jürgen; Koschitzky, Hans-Peter; Stuhrmann, Matthias: *VEGAS-Statuskolloquium 2006,* Tagungsband zur Veranstaltung am 28. September 2006 an der Universität Stuttgart, Campus Stuttgart-Vaihingen, 2006, ISBN 3-933761-53-0

151 Niessner, Jennifer: *Multi-Scale Modeling of Multi-Phase - Multi-Component Processes in Heterogeneous Porous Media*, 2006, ISBN 3-933761-54-9

152 Fischer, Markus: *Beanspruchung eingeerdeter Rohrleitungen infolge Austrocknung bindiger Böden,* 2006, ISBN 3-933761-55-7

153 Schneck, Alexander: *Optimierung der Grundwasserbewirtschaftung unter Berücksichtigung der Belange der Wasserversorgung, der Landwirtschaft und des Naturschutzes*, 2006, ISBN 3-933761-56-5

154 Das, Tapash: *The Impact of Spatial Variability of Precipitation on the Predictive Uncertainty of Hydrological Models,* 2006, ISBN 3-33761-57-3

155 Bielinski, Andreas: *Numerical Simulation of CO_2 sequestration in geological formations*, 2007, ISBN 3-933761-58-1

156 Mödinger, Jens: *Entwicklung eines Bewertungs- und Entscheidungsunterstützungssystems für eine nachhaltige regionale Grundwasserbewirtschaftung*, 2006, ISBN 3-933761-60-3

157 Manthey, Sabine: *Two-phase flow processes with dynamic effects in porous media - parameter estimation and simulation,* 2007, ISBN 3-933761-61-1

158 Pozos Estrada, Oscar: *Investigation on the Effects of Entrained Air in Pipelines,* 2007, ISBN 3-933761-62-X

159 Ochs, Steffen Oliver: *Steam injection into saturated porous media – process analysis including experimental and numerical investigations*, 2007, ISBN 3-933761-63-8

160 Marx, Andreas: *Einsatz gekoppelter Modelle und Wetterradar zur Abschätzung von Niederschlagsintensitäten und zur Abflussvorhersage, 2007,* ISBN 3-933761-64-6

161 Hartmann, Gabriele Maria: *Investigation of Evapotranspiration Concepts in Hydrological Modelling for Climate Change Impact Assessment*, 2007, ISBN 3-933761-65-4

162 Kebede Gurmessa, Tesfaye: *Numerical Investigation on Flow and Transport Characteristics to Improve Long-Term Simulation of Reservoir Sedimentation*, 2007, ISBN 3-933761-66-2

163 Trifković, Aleksandar: *Multi-objective and Risk-based Modelling Methodology for Planning, Design and Operation of Water Supply Systems*, 2007, ISBN 3-933761-67-0

164 Götzinger, Jens: *Distributed Conceptual Hydrological Modelling - Simulation of Climate, Land Use Change Impact and Uncertainty Analysis*, 2007, ISBN 3-933761-68-9

165 Hrsg.: Braun, Jürgen; Koschitzky, Hans-Peter; Stuhrmann, Matthias: *VEGAS – Kolloquium 2007,* Tagungsband zur Veranstaltung am 26. September 2007 an der Universität Stuttgart, Campus Stuttgart-Vaihingen, 2007, ISBN 3-933761-69-7

166 Freeman, Beau: *Modernization Criteria Assessment for Water Resources Planning; Klamath Irrigation Project, U.S.*, 2008, ISBN 3-933761-70-0

167 Dreher, Thomas: *Selektive Sedimentation von Feinstschwebstoffen in Wechselwirkung mit wandnahen turbulenten Strömungsbedingungen*, 2008, ISBN 3-933761-71-9

168 Yang, Wei: *Discrete-Continuous Downscaling Model for Generating Daily Precipitation Time Series*, 2008, ISBN 3-933761-72-7

169 Kopecki, Ianina: *Calculational Approach to FST-Hemispheres for Multiparametrical Benthos Habitat Modelling,* 2008*,* ISBN 3-933761-73-5

170 Brommundt, Jürgen: *Stochastische Generierung räumlich zusammenhängender Niederschlagszeitreihen*, 2008, ISBN 3-933761-74-3

171 Papafotiou, *Alexandros: Numerical Investigations of the Role of Hysteresis in Heterogeneous Two-Phase Flow Systems*, 2008, ISBN 3-933761-75-1

172 He, Yi: *Application of a Non-Parametric Classification Scheme to Catchment Hydrology*, 2008, ISBN 978-3-933761-76-7

173 Wagner, Sven: *Water Balance in a Poorly Gauged Basin in West Africa Using Atmospheric Modelling and Remote Sensing Information*, 2008, ISBN 978-3-933761-77-4

174 Hrsg.: Braun, Jürgen; Koschitzky, Hans-Peter; Stuhrmann, Matthias; Schrenk, Volker: *VEGAS-Kolloquium 2008 Ressource Fläche III*, Tagungsband zur Veranstaltung am 01. Oktober 2008 an der Universität Stuttgart, Campus Stuttgart-Vaihingen, 2008, ISBN 978-3-933761-78-1

175 Patil, Sachin: *Regionalization of an Event Based Nash Cascade Model for Flood Predictions in Ungauged Basins*, 2008, ISBN 978-3-933761-79-8

176 Assteerawatt, Anongnart: *Flow and Transport Modelling of Fractured Aquifers based on a Geostatistical Approach,* 2008, ISBN 978-3-933761-80-4

177 Karnahl, Joachim Alexander: *2D numerische Modellierung von multifraktionalem Schwebstoff- und Schadstofftransport in Flüssen*, 2008, ISBN 978-3-933761-81-1

178 Hiester, Uwe: *Technologieentwicklung zur In-situ-Sanierung der ungesättigten Bodenzone mit festen Wärmequellen,* 2009, ISBN 978-3-933761-82-8

179 Laux, Patrick: *Statistical Modeling of Precipitation for Agricultural Planning in the Volta Basin of West Africa,* 2009, ISBN 978-3-933761-83-5

180 Ehsan, Saqib: *Evaluation of Life Safety Risks Related to Severe Flooding,* 2009, ISBN 978-3-933761-84-2

181 Prohaska, Sandra: *Development and Application of a 1D Multi-Strip Fine Sediment Transport Model for Regulated Rivers,* 2009, ISBN 978-3-933761-85-9

182 Kopp, Andreas: *Evaluation of CO_2 Injection Processes in Geological Formations for Site Screening,* 2009, ISBN 978-3-933761-86-6

183 Ebigbo, Anozie: *Modelling of biofilm growth and its influence on CO_2 and water (two-phase) flow in porous media,* 2009, ISBN 978-3-933761-87-3

184 Freiboth, Sandra: *A phenomenological model for the numerical simulation of multiphase multicomponent processes considering structural alterations of porous media*, 2009, ISBN 978-3-933761-88-0

185 Zöllner, Frank: *Implementierung und Anwendung netzfreier Methoden im Konstruktiven Wasserbau und in der Hydromechanik*, 2009, ISBN 978-3-933761-89-7

186 Vasin, Milos: *Influence of the soil structure and property contrast on flow and transport in the unsaturated zone*, 2010, ISBN 978-3-933761-90-3

187 Li, Jing: *Application of Copulas as a New Geostatistical Tool*, 2010, ISBN 978-3-933761-91-0

188 AghaKouchak, Amir: *Simulation of Remotely Sensed Rainfall Fields Using Copulas*, 2010, ISBN 978-3-933761-92-7

189 Thapa, Pawan Kumar: *Physically-based spatially distributed rainfall runoff modelling for soil erosion estimation*, 2010, ISBN 978-3-933761-93-4

190 Wurms, Sven: *Numerische Modellierung der Sedimentationsprozesse in Retentionsanlagen zur Steuerung von Stoffströmen bei extremen Hochwasserabflussereignissen*, 2011, ISBN 978-3-933761-94-1

191 Merkel, Uwe: *Unsicherheitsanalyse hydraulischer Einwirkungen auf Hochwasserschutzdeiche und Steigerung der Leistungsfähigkeit durch adaptive Strömungsmodellierung*, 2011, ISBN 978-3-933761-95-8

192 Fritz, Jochen: *A Decoupled Model for Compositional Non-Isothermal Multiphase Flow in Porous Media and Multiphysics Approaches for Two-Phase Flow*, 2010, ISBN 978-3-933761-96-5

193 Weber, Karolin (Hrsg.): *12. Treffen junger WissenschaftlerInnen an Wasserbauinstituten*, 2010, ISBN 978-3-933761-97-2

194 Bliefernicht, Jan-Geert: *Probability Forecasts of Daily Areal Precipitation for Small River Basins,* 2011, ISBN 978-3-933761-98-9

195 Hrsg.: Koschitzky, Hans-Peter; Braun, Jürgen: *VEGAS-Kolloquium 2010 In-situ-Sanierung - Stand und Entwicklung Nano und ISCO -,* Tagungsband zur Veranstaltung am 07. Oktober 2010 an der Universität Stuttgart, Campus Stuttgart-Vaihingen*,* 2010*,* ISBN 978-3-933761-99-6

196 Gafurov, Abror: *Water Balance Modeling Using Remote Sensing Information - Focus on Central Asia,* 2010, ISBN 978-3-942036-00-9

197 Mackenberg, Sylvia: *Die Quellstärke in der Sickerwasserprognose: Möglichkeiten und Grenzen von Labor- und Freilanduntersuchungen,* 2010, ISBN 978-3-942036-01-6

198 Singh, Shailesh Kumar: *Robust Parameter Estimation in Gauged and Ungauged Basins,* 2010, ISBN 978-3-942036-02-3

199 Doğan, Mehmet Onur: *Coupling of porous media flow with pipe flow,* 2011, ISBN 978-3-942036-03-0

200 Liu, Min: *Study of Topographic Effects on Hydrological Patterns and the Implication on Hydrological Modeling and Data Interpolation,* 2011, ISBN 978-3-942036-04-7

201 Geleta, Habtamu Itefa: *Watershed Sediment Yield Modeling for Data Scarce Areas,* 2011, ISBN 978-3-942036-05-4

202 Franke, Jörg: *Einfluss der Überwachung auf die Versagenswahrscheinlichkeit von Staustufen,* 2011, ISBN 978-3-942036-06-1

203 Bakimchandra, Oinam: *Integrated Fuzzy-GIS approach for assessing regional soil erosion risks,* 2011, ISBN 978-3-942036-07-8

204 Alam, Muhammad Mahboob: *Statistical Downscaling of Extremes of Precipitation in Mesoscale Catchments from Different RCMs and Their Effects on Local Hydrology,* 2011, ISBN 978-3-942036-08-5

205 Hrsg.: Koschitzky, Hans-Peter; Braun, Jürgen: *VEGAS-Kolloquium 2011 Flache Geothermie - Perspektiven und Risiken,* Tagungsband zur Veranstaltung am 06. Oktober 2011 an der Universität Stuttgart, Campus Stuttgart-Vaihingen*,* 2011*,* ISBN 978-3-933761-09-2

206 Haslauer, Claus: *Analysis of Real-World Spatial Dependence of Subsurface Hydraulic Properties Using Copulas with a Focus on Solute Transport Behaviour,* 2011, ISBN 978-3-942036-10-8

207 Dung, Nguyen Viet: *Multi-objective automatic calibration of hydrodynamic models – development of the concept and an application in the Mekong Delta,* 2011, ISBN 978-3-942036-11-5

208 Hung, Nguyen Nghia: *Sediment dynamics in the floodplain of the Mekong Delta, Vietnam,* 2011, ISBN 978-3-942036-12-2

209 Kuhlmann, Anna: *Influence of soil structure and root water uptake on flow in the unsaturated zone,* 2012, ISBN 978-3-942036-13-9

210 Tuhtan, Jeffrey Andrew: *Including the Second Law Inequality in Aquatic Ecodynamics: A Modeling Approach for Alpine Rivers Impacted by Hydropeaking,* 2012, ISBN 978-3-942036-14-6

211 Tolossa, Habtamu: *Sediment Transport Computation Using a Data-Driven Adaptive Neuro-Fuzzy Modelling Approach,* 2012, ISBN 978-3-942036-15-3

212 Tatomir, Alexandru-Bodgan: *From Discrete to Continuum Concepts of Flow in Fractured Porous Media,* 2012, ISBN 978-3-942036-16-0

213 Erbertseder, Karin: *A Multi-Scale Model for Describing Cancer-Therapeutic Transport in the Human Lung,* 2012, ISBN 978-3-942036-17-7

214 Noack, Markus: *Modelling Approach for Interstitial Sediment Dynamics and Reproduction of Gravel Spawning Fish,* 2012, ISBN 978-3-942036-18-4

215 De Boer, Cjestmir Volkert: *Transport of Nano Sized Zero Valent Iron Colloids during Injection into the Subsurface*, 2012, ISBN 978-3-942036-19-1

216 Pfaff, Thomas: *Processing and Analysis of Weather Radar Data for Use in Hydrology*, 2013, ISBN 978-3-942036-20-7

217 Lebrenz, Hans-Henning: *Addressing the Input Uncertainty for Hydrological Modeling by a New Geostatistical Method*, 2013, ISBN 978-3-942036-21-4

218 Darcis, Melanie Yvonne: *Coupling Models of Different Complexity for the Simulation of CO_2 Storage in Deep Saline Aquifers*, 2013, ISBN 978-3-942036-22-1

219 Beck, Ferdinand: *Generation of Spatially Correlated Synthetic Rainfall Time Series in High Temporal Resolution - A Data Driven Approach*, 2013, ISBN 978-3-942036-23-8

220 Guthke, Philipp: *Non-multi-Gaussian spatial structures: Process-driven natural genesis, manifestation, modeling approaches, and influences on dependent processes*, 2013, ISBN 978-3-942036-24-5

221 Walter, Lena: *Uncertainty studies and risk assessment for CO_2 storage in geological formations*, 2013, ISBN 978-3-942036-25-2

222 Wolff, Markus: *Multi-scale modeling of two-phase flow in porous media including capillary pressure effects,* 2013, ISBN 978-3-942036-26-9

223 Mosthaf, Klaus Roland: *Modeling and analysis of coupled porous-medium and free flow with application to evaporation processes,* 2014, ISBN 978-3-942036-27-6

224 Leube, Philipp Christoph: *Methods for Physically-Based Model Reduction in Time: Analysis, Comparison of Methods and Application*, 2013, ISBN 978-3-942036-28-3

225 Rodríguez Fernández, Jhan Ignacio: *High Order Interactions among environmental variables: Diagnostics and initial steps towards modeling*, 2013, ISBN 978-3-942036-29-0

226 Eder, Maria Magdalena: *Climate Sensitivity of a Large Lake*, 2013, ISBN 978-3-942036-30-6

227 Greiner, Philipp: *Alkoholinjektion zur In-situ-Sanierung von CKW Schadensherden in Grundwasserleitern: Charakterisierung der relevanten Prozesse auf unterschiedlichen Skalen*, 2014, ISBN 978-3-942036-31-3

228 Lauser, Andreas: *Theory and Numerical Applications of Compositional Multi-Phase Flow in Porous Media*, 2014, ISBN 978-3-942036-32-0

229 Enzenhöfer, Rainer: *Risk Quantification and Management in Water Production and Supply Systems*, 2014, ISBN 978-3-942036-33-7

230 Faigle, Benjamin: *Adaptive modelling of compositional multi-phase flow with capillary pressure*, 2014, ISBN 978-3-942036-34-4

231 Oladyshkin, Sergey: *Efficient modeling of environmental systems in the face of complexity and uncertainty*, 2014, ISBN 978-3-942036-35-1

232 Sugimoto, Takayuki: *Copula based Stochastic Analysis of Discharge Time Series*, 2014, ISBN 978-3-942036-36-8

233 Koch, Jonas: *Simulation, Identification and Characterization of Contaminant Source Architectures in the Subsurface*, 2014, ISBN 978-3-942036-37-5

234 Zhang, Jin: *Investigations on Urban River Regulation and Ecological Rehabilitation Measures, Case of Shenzhen in China*, 2014, ISBN 978-3-942036-38-2

235 Siebel, Rüdiger: *Experimentelle Untersuchungen zur hydrodynamischen Belastung und Standsicherheit von Deckwerken an überströmbaren Erddämmen,* 2014, ISBN 978-3-942036-39-9

236 Baber, Katherina: *Coupling free flow and flow in porous media in biological and technical applications: From a simple to a complex interface description,* 2014, ISBN 978-3-942036-40-5

237 Nuske, Klaus Philipp: *Beyond Local Equilibrium — Relaxing local equilibrium assumptions in multiphase flow in porous media,* 2014, ISBN 978-3-942036-41-2

238 Geiges, Andreas: *Efficient concepts for optimal experimental design in nonlinear environmental systems*, 2014, ISBN 978-3-942036-42-9

239 Schwenck, Nicolas: *An XFEM-Based Model for Fluid Flow in Fractured Porous Media*, 2014, ISBN 978-3-942036-43-6

240 Chamorro Chávez, Alejandro: *Stochastic and hydrological modelling for climate change prediction in the Lima region, Peru*, 2015, ISBN 978-3-942036-44-3

241 Yulizar: *Investigation of Changes in Hydro-Meteorological Time Series Using a Depth-Based Approach*, 2015, ISBN 978-3-942036-45-0

242 Kretschmer, Nicole: *Impacts of the existing water allocation scheme on the Limarí watershed – Chile, an integrative approach*, 2015, ISBN 978-3-942036-46-7

243 Kramer, Matthias: *Luftbedarf von Freistrahlturbinen im Gegendruckbetrieb*, 2015, ISBN 978-3-942036-47-4

244 Hommel, Johannes: *Modeling biogeochemical and mass transport processes in the subsurface: Investigation of microbially induced calcite precipitation*, 2016, ISBN 978-3-942036-48-1

245 Germer, Kai: *Wasserinfiltration in die ungesättigte Zone eines makroporösen Hanges und deren Einfluss auf die Hangstabilität*, 2016, ISBN 978-3-942036-49-8

246 Hörning, Sebastian: *Process-oriented modeling of spatial random fields using copulas*, 2016, ISBN 978-3-942036-50-4

247 Jambhekar, Vishal: *Numerical modeling and analysis of evaporative salinization in a coupled free-flow porous-media system,* 2016, ISBN 978-3-942036-51-1

248 Huang, Yingchun: *Study on the spatial and temporal transferability of conceptual hydrological models*, 2016, ISBN 978-3-942036-52-8

249 Kleinknecht, Simon Matthias: *Migration and retention of a heavy NAPL vapor and remediation of the unsaturated zone*, 2016, ISBN 978-3-942036-53-5

250 Kwakye, Stephen Oppong: *Study on the effects of climate change on the hydrology of the West African sub-region*, 2016, ISBN 978-3-942036-54-2

251 Kissinger, Alexander: *Basin-Scale Site Screening and Investigation of Possible Impacts of CO_2 Storage on Subsurface Hydrosystems*, 2016, ISBN 978-3-942036-55-9

252 Müller, Thomas: *Generation of a Realistic Temporal Structure of Synthetic Precipitation Time Series for Sewer Applications*, 2017, ISBN 978-3-942036-56-6

253 Grüninger, Christoph: *Numerical Coupling of Navier-Stokes and Darcy Flow for Soil-Water Evaporation*, 2017, ISBN 978-3-942036-57-3

254 Suroso: *Asymmetric Dependence Based Spatial Copula Models: Empirical Investigations and Consequences on Precipitation Fields*, 2017, ISBN 978-3-942036-58-0

255 Müller, Thomas; Mosthaf, Tobias; Gunzenhauser, Sarah; Seidel, Jochen; Bárdossy, András: *Grundlagenbericht Niederschlags-Simulator (NiedSim3)*, 2017, ISBN 978-3-942036-59-7

256 Mosthaf, Tobias: *New Concepts for Regionalizing Temporal Distributions of Precipitation and for its Application in Spatial Rainfall Simulation,* 2017, ISBN 978-3-942036-60-3

257 Fenrich, Eva Katrin: *Entwicklung eines ökologisch-ökonomischen Vernetzungsmodells für Wasserkraftanlagen und Mehrzweckspeicher,* 2018, ISBN 978-3-942036-61-0

258 Schmidt, Holger: *Microbial stabilization of lotic fine sediments*, 2018, ISBN 978-3-942036-62-7

259 Fetzer, Thomas: *Coupled Free and Porous-Medium Flow Processes Affected by Turbulence and Roughness – Models, Concepts and Analysis*, 2018, ISBN 978-3-942036-63-4

260 Schröder, Hans Christoph: *Large-scale High Head Pico Hydropower Potential Assessment*, 2018, ISBN 978-3-942036-64-1

261 Bode, Felix: *Early-Warning Monitoring Systems for Improved Drinking Water Resource Protection*, 2018, ISBN 978-3-942036-65-8

262 Gebler, Tobias: *Statistische Auswertung von simulierten Talsperrenüberwachungsdaten zur Identifikation von Schadensprozessen an Gewichtsstaumauern*, 2018, ISBN 978-3-942036-66-5

263 Harten, Matthias von: *Analyse des Zuppinger-Wasserrades – Hydraulische Optimierungen unter Berücksichtigung ökologischer Aspekte*, 2018, ISBN 978-3-942036-67-2

264 Yan, Jieru: *Nonlinear estimation of short time precipitation using weather radar and surface observations*, 2018, ISBN 978-3-942036-68-9

265 Beck, Martin: *Conceptual approaches for the analysis of coupled hydraulic and geomechanical processes*, 2019, ISBN 978-3-942036-69-6

266 Haas, Jannik: *Optimal planning of hydropower and energy storage technologies for fully renewable power systems*, 2019, ISBN 978-3-942036-70-2

267 Schneider, Martin: *Nonlinear Finite Volume Schemes for Complex Flow Processes and Challenging Grids*, 2019, ISBN 978-3-942036-71-9

268 Most, Sebastian Christopher: *Analysis and Simulation of Anomalous Transport in Porous Media*, 2019, ISBN 978-3-942036-72-6

269 Buchta, Rocco: *Entwicklung eines Ziel- und Bewertungssystems zur Schaffung nachhaltiger naturnaher Strukturen in großen sandgeprägten Flüssen des norddeutschen Tieflandes*, 2019, ISBN 978-3-942036-73-3

270 Thom, Moritz: *Towards a Better Understanding of the Biostabilization Mechanisms of Sediment Beds*, 2019, ISBN 978-3-942036-74-0

271 Stolz, Daniel: *Die Nullspannungstemperatur in Gewichtsstaumauern unter Berücksichtigung der Festigkeitsentwicklung des Betons*, 2019, ISBN 978-3-942036-75-7

272 Rodriguez Pretelin, Abelardo: *Integrating transient flow conditions into groundwater well protection*, 2020, ISBN: 978-3-942036-76-4

273 Weishaupt, Kilian: *Model Concepts for Coupling Free Flow with Porous Medium Flow at the Pore-Network Scale: From Single-Phase Flow to Compositional Non-Isothermal Two-Phase Flow*, 2020, ISBN: 978-3-942036-77-1

274 Koch, Timo: *Mixed-dimension models for flow and transport processes in porous media with embedded tubular network systems*, 2020, ISBN: 978-3-942036-78-8

275 Gläser, Dennis: *Discrete fracture modeling of multi-phase flow and deformation in fractured poroelastic media*, 2020, ISBN: 978-3-942036-79-5

276 Seitz, Lydia: *Development of new methods to apply a multi-parameter approach – A first step towards the determination of colmation*, 2020, ISBN: 978-3-942036-80-1

277 Ebrahim Bakhshipour, Amin: *Optimizing hybrid decentralized systems for sustainable urban drainage infrastructures planning*, 2021, ISBN: 978-3-942036-81-8

278 Seitz, Gabriele: *Modeling Fixed-Bed Reactors for Thermochemical Heat Storage with the Reaction System CaO/Ca(OH)$_2$*, 2021, ISBN: 978-3-942036-82-5

Die Mitteilungshefte ab der Nr. 134 (Jg. 2005) stehen als pdf-Datei über die Homepage des Instituts: www.iws.uni-stuttgart.de zur Verfügung.